Using Multibeam Echosounders for Multiscale and Interdisciplinary Habitat Mapping on the Dutch Continental Shelf

Koop, L.

DOI
10.4233/uuid:1af34dce-0e3b-45d0-8851-b62546121185e

Publication date
2022

Document Version
Final published version

Citation (APA)
Koop, L. (2022). *Using Multibeam Echosounders for Multiscale and Interdisciplinary Habitat Mapping on the Dutch Continental Shelf*. [Dissertation (TU Delft), Delft University of Technology]. https://doi.org/10.4233/uuid:1af34dce-0e3b-45d0-8851-b62546121185e

Using Multibeam Echosounders for Multiscale and Interdisciplinary Habitat Mapping on the Dutch Continental Shelf

Using Multibeam Echosounders for Multiscale and Interdisciplinary Habitat Mapping on the Dutch Continental Shelf

Dissertation

for the purpose of obtaining the degree of doctor
at Delft University of Technology,
by the authority of the Rector Magnificus Prof. dr. ir. T.H.J.J. van der Hagen,
chair of the Board for Doctorates,
to be defended publicly on
Monday 7 February 2022 at 12:30 o'clock

by

Leo KOOP

Master of Science in Applied Mathematics,
Delft University of Technology, the Netherlands;
Master of Science in Scientific Computing,
Berlin Institute of Technology, Germany
born in Spanish Lookout, Belize.

The dissertation has been approved by the promoters.

Composition of the doctoral committee:

Rector Magnificus,	chairman
Prof.dr. D. G. Simons,	Delft University of Technology, promotor
Prof.dr.ir. M. Snellen,	Delft University of Technology, promotor

Independent members:

Prof.dr.ir. C. P. A. Wapenaar	Delft University of Technology
Prof.dr.ir. E. C. Slob	Delft University of Technology
Prof.dr. J. Greinert	Christian-Albrecht University, Kiel, Germany
Dr.ir. F. C. Vossepoel	Delft University of Technology
Prof.dr. V. Grewe	Delft University of Technology, reserve member

Other member:

Prof.dr. P. M. J. Herman	Delft University of Technology

TUDelft Delft University of Technology

GIESKES·STRIJBIS
FONDS

Keywords: Multibeam Echosounder, Sediment Classification, Dutch North Sea, Object-based image analysis, Backscatter, Bathymetry, Bathymetric derivatives, Grab samples, Bayesian classification, Seafloor mapping, Benthic habitats, Marine geology, Sandbanks, Tidal ridges, Sand waves, Mega ripples, Sand ripples

Printed by: IPSKAMP printing

Front & Back: An illustration of the multidisciplinary habitat mapping approach taken in the DISCLOSE project. Illustration by Tamara van Dijk.

ISBN 978-94-6384-297-6

An electronic version of this dissertation is available at
`http://repository.tudelft.nl/`.

To my parents, who always encouraged me to learn.

Contents

Summary

Because the seafloor is a complex ecosystem, a multidisciplinary approach must be adopted in order to produce comprehensive habitat maps. Such multidisciplinary projects have been lacking for the Dutch area of the North Sea. To address this lack, the ***Di**stribution, **s**tru**c**ture and functioning of **lo**w resilience seafloor communities and habitats of the Dutch North **Se**a* (DISCLOSE) project, funded by the Gieskes-Strijbis Fonds, was initiated. The consortium for the project included three research institutes, as well as the North Sea Foundation. The first of the research institutes was the Delft University of Technology, tasked with the large-scale mapping of the seafloor, using acoustic systems such as the multibeam echosounder (MBES). The second research institute, the University of Groningen (UG), focused on the use of photography and videography to study the seafloor and the epifauna at a smaller, yet more detailed, spatial scale. Finally, the Royal Netherlands Institute for Sea Research (NIOZ), studied the seafloor from both the perspective of particle size and macrofauna using grab-sample data. All of these measurement methods were utilized for the same research areas, in order to maximize the possibility to established links between the sampling methods, and thereby create detailed habitat maps. The work in this thesis focuses specifically on the acoustic results generated within the DISCLOSE project.

In recent years the MBES has become the standard tool for the large-scale mapping of the ocean floor. With the MBES, large swaths of the seafloor can be covered in short periods of time. The use of the two-way travel time to measure the bathymetry of the ocean has become very standardized. In addition to measuring the bathymetry, the MBES can also deliver the collocated backscatter product. The appropriate use of backscatter for the classification of seafloor properties and habitats is much less well understood than bathymetry. As such, this is an active field of research. Within Dutch waters, most research has taken place using datasets from the area of the Cleaverbank. Other areas have not been well studied, for example, the southern sandy area. Utilizing MBES backscatter-based seafloor classification in sandy areas is a major focus in this thesis.

A dataset from the Brown Bank area of the North Sea was used in order to study seafloor classification over mega ripple structures. A big part of the Southern North Sea is covered in nested sand waves of different sizes. The largest of these is the tidal ridge, with some ten kilometers from crest to crest. The second largest is the sand wave, and the smallest is the mega ripple. Obviously, the main sediment type in this area is sand. Previous research suggests that a difference in grain size is to be expected between the crest of the tidal ridge to the trough. It was not known if a difference in grain size from the crest to the trough of the sand wave or the mega ripple is present, or detectable using MBES backscatter. As such, for this research a few things were very important. Firstly, it was necessary to accurately correct the backscatter for the seafloor slopes in the research area. Next, it was important to

have a high spatial resolution for the final classification results. Additionally, a high geo-acoustic resolution was also needed. This final resolution is needed because it is expected that the difference in sediment properties from the trough to crest of a mega-ripple may be just slightly coarser or finer sand. From our research, it was found that it is possible to use MBES backscatter in order to classify the sediment types at the scale of mega ripples. It was found that the coarsest sediments were in the troughs, finer sediments on the stoss side slopes, and a mixture of sediments on the lee side slopes of the mega ripples.

A different data set from the Brown Bank area was used to further study the effects of small sand ripples on MBES backscatter data. It is important to note that these sand ripples were smaller than the above mentioned mega ripples. They were so small that they were not resolved in the bathymetry data. For this research, data from two MBESs and four different frequencies were available. These frequencies ranged from 30 kHz to 450 kHz. It was found that these small sand ripples had a, survey-azimuth dependent, effect which was discernible in the angular response curves (ARCs) which were created from the MBES backscatter. ARCs consider the backscatter intensity as a function of the angle between the seafloor and direction of the incoming acoustic waves. Similar patterns have previously been found in other research. However, it was not previously shown that the orientation and shape of the sand ripples could be determined based on the affected ARCs. By sailing specific patterns over the seafloor, the orientation of the sand ripples was determined successfully. The angles of the stoss and lee sides of the sand ripples were also estimated. It was further found that the sand ripples changed orientation when the tide direction shifted.

Thus far, most of the acoustic research within the DISCLOSE project focused on backscatter-based classification in sandy environments of the southern North Sea. But with only these results, and because of the fact that backscatter data is not available for the entirety of the North Sea, only small areas of the seafloor could be classified using these methods. Therefore, it was necessary to develop a different algorithm that could classify the seafloor based on the much more widely available bathymetry. In order to develop such a method, data from an area from Norwegian waters was used, where both backscatter and bathymetry data, as well as a number of ground truth data points were available from an heterogeneous area of seafloor. Two methods were developed, using an object-based image analysis (OBIA) approach. The best performing algorithm was transferred to a data set from the Dutch North Sea and further tested. It was found that that OBIA method transferred well from one area to another. Furthermore the OBIA based classification results were acceptable, with a 10% decrease in accuracy when these results and backscatter-based classification results were compared to grab-sample ground-reference data. Additionally, the computation requirements for this method were small compared to many other image-classification methods. This makes the developed method applicable to large areas of the North Sea, and could in the future be adapted to global bathymetric maps.

As indicated, DISCLOSE was a multidisciplinary project. As such, the focus was not just on acoustics. In order to get the most out of this project it was necessary to create links between the different sampling methods. Video and grab-sample data was already previously used to ground truth the acoustic results. But a further link between the different methods was needed. Therefore, in the final chapter an additional classification method was developed in which a number of new sediment parameters were estimated from the acoustic data. These were then related to biological data, to identify the most informative acoustic parameters with respect to macrobenthos. It was found that the volume scattering parameter was a valuable parameter to predict the presence of, for example, Sabellaria Spinulosa reefs. It was further found that there was a variation in macrobenthic densities from the crest to the trough of sand waves. In this manner, the value of the DISCLOSE method was confirmed.

Samenvatting

Omdat de zeebodem een complex ecosysteem is, moet een multidisciplinaire benadering worden gevolgd om uitgebreide habitatkaarten te produceren. Voor het Nederlandse deel van de Noordzee ontbraken dergelijke multidisciplinaire projecten. Om hierop in te spelen is het ***Di**stribution, **s**tru**c**ture and functioning of **lo**w resilience seafloor communities and habitats of the Dutch North **Se**a* (DISCLOSE) project, gefinancierd door het Gieskes-Strijbis Fonds, gestart. Het consortium voor het project omvatte drie onderzoeksinstituten, evenals de Stichting De Noordzee. De eerste van de onderzoeksinstituten was de Technische Universiteit Delft, belast met het op grote schaal in kaart brengen van de zeebodem met behulp van akoestische systemen zoals de multibeam echolood (MBES). Het tweede onderzoeksinstituut, de Rijksuniversiteit Groningen (RUG), richtte zich op het gebruik van fotografie en videografie om de zeebodem en de epifauna op kleinere, maar meer gedetailleerde, ruimtelijke schaal te bestuderen. Ten slotte heeft het Koninklijk Nederlands Instituut voor Onderzoek der Zee (NIOZ) de zeebodem zowel vanuit het perspectief van de deeltjesgrootte als de macrofauna bestudeerd met behulp van steekmonstergegevens. Al deze meetmethoden werden in dezelfde onderzoeksgebieden gebruikt zodat de mogelijkheid om bemonsteringsmethoden te koppelen, en zo gedetailleerde habitatkaarten te maken, werd vergroot. Het werk in dit proefschrift richt zich specifiek op de akoestische resultaten die zijn gegenereerd binnen het DISCLOSE-project.

De MBES is de afgelopen jaren het standaardinstrument geworden voor het op grote schaal in kaart brengen van de oceaanbodem. Met de MBES kunnen grote delen van de zeebodem in korte tijd in kaart worden gebracht. Het gebruik van de exacte tijdsduur tussen het uitzenden van het geluid en het opvangen van de echo is een gestandaardizeerde methode om de diepte van de oceanen te bepalen. Een MBES kan, naast de exacte tijdsduur, ook andere kenmerken van de opgevangen echo registreren, zoals de intensiteit (backscatter). Deze backscatter data kan gebruikt worden om zeebodemeigenschappen en habitats te classificeren, al is er nog geen eenduidige methode ontwikkeld om dit te doen. Als zodanig is dit een actief onderzoeksgebied. Binnen de Nederlandse wateren is het meeste onderzoek gedaan met datasets uit het gebied van de Klaverbank. Andere gebieden zijn niet goed onderzocht, bijvoorbeeld het zuidelijke zandgebied. Het gebruik van MBES op backscatter gebaseerde zeebodemclassificatie in zandige gebieden is een belangrijk aandachtspunt in dit proefschrift.

Een dataset uit het Bruine Bank-gebied van de Noordzee werd gebruikt om de classificatie van de zeebodem over mega-ribbelstructuren te bestuderen. Een groot deel van de zuidelijke Noordzee is bedekt met genestelde zandgolven van verschillende groottes. De grootste hiervan zijn de zandbanken, met zo’n tien kilometer van top tot top. De op één na grootste zijn de zandgolven, en de kleinste zijn de megaribbels. Het belangrijkste sedimenttype in dit gebied is uiteraard zand. Op basis van eerder onderzoek werd er een verschil in korrelgrootte verwacht tussen de top en het dal van de zandbank. Het was niet bekend of er een verschil in korrelgrootte van de top tot het dal van de zandgolven of de megaribbel aanwezig is, of detecteerbaar is met MBES-backscatter. Voor dit onderzoek waren daarom een aantal zaken erg belangrijk. Ten eerste was het nodig om de backscatter nauwkeurig te corrigeren voor hellingen van de zeebodem in het onderzoeksgebied. Vervolgens was het belangrijk om een hoge ruimtelijke resolutie te hebben voor de uiteindelijke classificatieresultaten. Daarnaast was ook een hoge geo-akoestische resolutie nodig. Deze resolutie is nodig omdat verwacht wordt dat het verschil in sedimenteigenschappen van de dal tot de top van een megaribbel net iets grover of fijner zand kan zijn. Uit ons onderzoek is gebleken dat het mogelijk is om MBES-backscatter te gebruiken om de sedimenttypen op de schaal van megaribbels te classificeren. Het bleek dat de grofste sedimenten zich in de dalen bevonden, fijnere sedimenten op de loef-zijde en een mengsel van sedimenten op de lijzijde van de megaribbels.

Een andere dataset uit het Brown Bank-gebied werd gebruikt om de effecten van kleine zandribbels op MBES-backscatter verder te bestuderen. Het is belangrijk op te merken dat deze zandribbels kleiner waren dan de bovengenoemde megaribbels. Ze waren zo klein dat ze niet zichtbaar waren in de bathymetrische gegevens. Voor dit onderzoek waren gegevens van twee MBES'en en vier verschillende frequenties beschikbaar. Deze frequenties varieerden van 30 kHz tot 450 kHz. Er werd gevonden dat deze kleine zandribbels een (vaarrichting-afhankelijk) effect hadden dat waarneembaar was in de Angular Response Curves die werden gecreëerd op basis van de backscatter. ARC's beschouwen de backscatter als een functie van de hoek tussen de zeebodem en de richting van de binnenkomende akoestische golven. Soortgelijke patronen zijn eerder gevonden in ander onderzoek. Het was echter niet eerder aangetoond dat de oriëntatie en vorm van de zandribbels konden worden bepaald op basis van de getroffen ARC's. Door in specifieke patronen over de zeebodem te varen, werd de oriëntatie van de zandribbels met succes bepaald. De hoeken van de loef- en lij-zijden van de zandribbels werden ook geschat. Verder werd gevonden dat de zandribbels van richting veranderden wanneer het tij van richting veranderde.

Tot dusver was het meeste akoestische onderzoek binnen het DISCLOSE-project gericht op op backscatter gebaseerde classificatie in zandige omgevingen van de zuidelijke Noordzee. Maar met alleen deze resultaten, en omdat backscattergegevens niet voor de gehele Noordzee beschikbaar zijn, konden alleen kleine delen van de zeebodem met deze methoden worden geclassificeerd. Daarom was het nodig om een ander algoritme te ontwikkelen dat de zeebodem kon classificeren op basis van de veel breder beschikbare bathymetrie. Om een dergelijke methode te ontwikkelen, werden gegevens uit een gebied uit de Noorse wateren gebruikt, waar zowel backscatter- als bathymetriegegevens, evenals een aantal bodemmonsters beschikbaar waren van een heterogeen gebied van de zeebodem. Er werden twee methoden ontwikkeld, waarbij gebruik werd gemaakt van een objectgebaseerde beeldanalyse (OBIA)-benadering. Het best presterende algoritme is verder getest op een dataset uit de Nederlandse Noordzee. Het bleek dat die OBIA-methode goed toepasbaar was op beide gebieden. Verder waren de op OBIA gebaseerde classificatieresultaten acceptabel, met een afname van 10% in nauwkeurigheid wanneer deze resultaten en op backscatter gebaseerde classificatieresultaten werden vergeleken met de gemeten waarden van de steekproeven. Bovendien waren de berekeningsvereisten voor deze methode klein in vergelijking met veel andere beeldclassificatiemethoden. Dit maakt de ontwikkelde methode toepasbaar op grote delen van de Noordzee en kan deze in de toekomst worden toegepast op mondiale bathymetrische kaarten.

Zoals aangegeven was DISCLOSE een multidisciplinair project. De focus lag dus niet alleen op akoestiek. Om het maximale uit dit project te halen was het noodzakelijk om koppelingen te maken tussen de verschillende steekproefmethoden. Video- en bodemmonsters werden al eerder gebruikt om de akoestische resultaten te valideren. Maar er was behoefte aan een verdere koppeling tussen de verschillende methoden. Daarom is in het laatste hoofdstuk een aanvullende classificatiemethode ontwikkeld waarin een aantal nieuwe sedimentparameters zijn geschat op basis van de akoestische gegevens. Deze zijn vervolgens gerelateerd aan biologische gegevens om de parameters te identificeren die het meest informatief zijn over het macrobenthische leven. Het bleek dat de volumeverstrooiingsparameter een waardevolle parameter was om de aanwezigheid van bijvoorbeeld Sabellaria Spinulosa-riffen te voorspellen. Verder werd gevonden dat er een variatie was in macrobenthische dichtheden van de top tot het dal van zandgolven. Op deze manier werd de waarde van de DISCLOSE-methode bevestigd.

Nomenclature

Latin symbols

a_x, a_y	Seafloor slope in amount of rise over a meter in the x and y directions
A	Ensonified area
A'_f	Estimated ensonified area assuming a flat seafloor
A_f	Estimated ensonified area accounting for seafloor slopes
A_k	Acceptance region
B	Bulk modulus of a medium
b_i	$i \in (1, 2, m)$ Bounding box of image object 1, 2, or m
BP, BP_T, BP_R	Beam pattern in dB, during transmission, during reception
BPI_{r_p}, BPI_{r_d}	Bathymetric position index with out radius in pixels, or meters
BS	Backscattering strength in dB per m^2 at 1m
c	Speed of sound
cm	Centimeter
com	Compactness of an image object
d	Depth, Grain size in mm
D	Coefficient matrix
d_{m_ℓ}	The distance between the wavefront and the hydrophone m_ℓ
E	Easting geographic coordinate
f	Frequency of the acoustic wave
h	Heterogeneity in an image object (OBIA)
h_c H	Hypothesis in Bayesian decision rule (Chapter 3), Height of a sand wave (Chapter 3)
H_{avg}, H_{max}	Average and maximum height of sand ripples based on their length
I_G	Gini impurity index
k	Wave number, Grain size kurtosis (Chapter 3)
L	Sand wave length (Chapter 4), Pixel size (Chapter 5)
L_x	Distance between sound sources
L_y	Total length of hydrophone array
m	Meter
mm	Millimeter
$\overrightarrow{\mathbf{m}}$	Unit vector from a point on the seafloor towards the MBES
m	Number of Gaussian distributions fitted to backscatter data
m_ℓ	The ℓ^{th} hydrophone in the microphone array
M	Number of hydrophones in an acoustic array (Chapter 2); Number of bins in BS histogram (Chapter 3)
N_s	Number of scatter pixels per beam
N	Northing coordinate
n_j	Number of BS measurements per bin j of BS histogram

n_i	$i \in (1, 2, m)$ the number of pixels in image object 1, 2 or m.
$\vec{\mathbf{n}}$	Normal vector to seafloor
M_z	Mean grain size
o_1	A seed image object
p	Acoustic pressure
p_0	Acoustic pressure amplitude 1 m away from the source
PG	Processing gain in dB
p_i	$i \in (1, 2, m)$ perimeter of image object 1, 2, or m
r	Distance to source
r_d	Radius in meters
r_p	Radius in pixels
s	Axis of acoustic wave travel, or seconds, grain size skewness (Chapter 3), Slope (Chapter 5)
S	Salinity
S_A, S_B	Signal measured at sub-array A and B
SH	Transducer sensitivity in dB
SL	Source level
sm	Smoothness of an image object
S_p	Scale parameter
t	Time generally; or the 2 way travel time
t_ℓ	Phase delay at the ℓ^{th} element of an acoustic array
T	Temperature (Chapter 2), Pulse length (Chapter 3)
TL	Transmission loss
TS	Target strength
$w_c, w_s, w_{com}, w_{sm}$	Weights for color, shape, compactness, and smoothness contribution
w_ℓ	Weight given to image layer
x	Spatial coordinate
x_s	Pixel size in the x direction
$\mathbf{x}$	Vector of Gaussian unknowns
y	Spatial coordinate BS value of bin in the BS histogram (Bayesian)
$\bar{y}_k, \sigma_{y_k}, c_k$	Mean, standard deviation, and contribution of Gaussians fitted to BS histogram
y_j	BS value at bin j of a BS histogram
y_s	Pixel size in the y direction
z	Spatial coordinate

Greek symbols

α	Attenuation coefficient given in dB
α_x, α_y	Across and along track slopes of the seafloor in degrees
γ	Spectral exponent (APL)
$\gamma_0, \gamma_1, \gamma_2$	Angles where there are peaks in ARCs
δy	The distance between elements in a hydrophone array
Δ	Bin size of BS histogram
Δh	Heterogeneity change in image object
Δh_c	Heterogeneity change with respect to color
Δh_s	Heterogeneity change with respect to shape
η	Spectral strength (APL)
θ	Incident angle, between incident wave and surface normal; Beam angle
θ_t	Incident angle adjusted for seafloor slopes
λ	Acoustic wave length
ν	Degrees of freedom
ρ	Density
σ	Grain size sorting
$\sigma_{\ell,i}$	$i \in (1, 2, m)$ the standard deviation within image object 1, 2, or m
$\hat{\sigma}_v$	Volume scattering parameter (APL)
ϕ	Steering angle,
	Grain size
ϕ_{50}	Median grain size
ϕ_i	The i^{th} grain size percentile of a grab sample
φ	Grazing angle
$\widehat{\Delta\varphi}$	Estimated phase difference
χ^2	Goodness of fit test
χ^2_ν	Reduced chi-squared statistic
ω	Radial frequency of an acoustic wave
Ω	Beam width
Ω_y	Across-track beam opening angle
µm	Micrometer
µs	Microsecond

Mathematical symbols

$\frac{\partial p}{\partial s}$	Partial derivative of the function p with respect to the variable s
$\frac{\partial^2 p}{\partial s^2}$	Second order partial derivative of the function p with respect to the variable s
∇^2	Laplace operator
$\frac{dz}{dx}, \frac{dz}{dy}$	Derivative of a function with respect to x and y

Acronyms

General acronyms

AC	Acoustic class
ARC	Angular-response curve
BC	Bin center
BPI	Bathymetric Position Index
BS	Backscatter
CTD	Conductivity temperature, and pressure
dB	Decibel
DCS	Dutch continental shelf
DISCLOSE	**DI**stribution, **S**tru**C**ture and functioning of **LO**wresilience benthic communities and habitats of the Dutch North **SE**a
DTM	Digital terrain model
EMODNet	European Marine Observation and Data Network
ETRS	European Terrestrial Reference System
GPS	Global positioning system
gsf	Generic sensor format
LMM	Linear mixed model
MBES	Multibeam echosounder
MBES	Multibeam echosounder
MRU	Motion reference unit
MSFD	Marine Strategy Framework Directive
NIOZ	Royal Netherlands Institute for Sea Research
OBIA	Object-based image analysis
PC	Principal component
PCA	Principal component analysis
PDFs	Probability density functions
PSA	Particle size analysis
QPS	Quality Positioning Systems
ROV	Remotely operated vehicle
RVO	Rijksdienst voor Ondernemend Nederland (Netherlands Enterprise Agency)
SBES	Singlebeam echosounder
SIS	Seafloor information system
SPI	Sediment profile imaging
SSS	Side scan sonar
UTM	Universal Transverse Mercator
WGS	World Geodetic System

Sediment acronyms

M	Mud
sM	Sandy mud
mS	Muddy sand
S	Sand
(g)S	Slightly gravely sand
gS	Gravely sand
sG	Sandy gravel
G	Gravel
R	Rock

1

Introduction

In questions of science, the authority of a thousand
is not worth the humble reasoning of a single individual.

Galileo Galilei

He who controls the sea controls everything.

Themistocles

1.1. Motivation

To the countries around its borders, the North Sea has played an integral part of their modern history. From 835 to 1050 AD the Vikings ruled much of the area around the North Sea [1]. Throughout the middle ages, before the development of good roads, the North Sea facilitated much of Europe's trading ability [2]. For no other European country has the North Sea played as significant of a role as for the Netherlands. It was the trade on the North Sea that helped to usher in the so called, Dutch Golden years from 1500 to 1815. Various Dutch Ports have been the largest in the world at various times. In the 13th century the Port of Amsterdam rose to importance. Later, in the 17th century it became the main port of the Dutch East India Trading company. More recently, the Port of Rotterdam outgrew the Port of Amsterdam. Until recently (2004) it was the world's busiest port [3]. The ports of Dordrecht and Delft have also played their part in Dutch history. Of course, Dutch ports are only a fraction of the ports that interact with the North Sea. All of this shipping activity is one of the reasons why the North Sea is also one of the busiest seas of the world [4, 5].

In addition to the shipping activity on the North Sea, it is also one of the most bottom trawled continental shelves in the world [6]. It has further been shown that this fishing activity is focused on specific habitats [7]. Oil and gas extraction and exploration is another major activity on the North Sea [8]. All of these activities have a significant effect on the benthic habitats of the North Sea.

Current regulations require the effects of all these economic activities on marine life to be assessed [9]. But for all the advances in science and our increasing capability to study habitats on larger scales, less than 18% of the world's oceans are mapped [10]. Furthermore, it is one thing to map the bathymetry of the ocean, but a much more complicated matter is to map sediment distributions or habitats in the oceans.

The study of habitats is very multifaceted, and as such, any effort to create comprehensive habitat maps must utilize a multi-disciplinary approach. There are multiple methods that are commonly employed for the study of benthic habitats including acoustic methods [11, and references therein], video and photographic methods [12], and grab sampling [13–15] among others. With this as the background, the DISCLOSE project (**DI**stribution, **S**tru**C**ture and functioning of **LO**w-resilience benthic communities and habitats of the Dutch North **SE**a) was initiated, to address the knowledge gap in benthic habitat mapping in the Dutch North Sea. In the DISCLOSE project, three main methodologies are employed. Firstly, at the largest scale, acoustic mapping systems are used to create detailed maps of the seabed bathymetry, topography, and sediment composition. Next, the distribution and functioning of benthic marine habitats are studied at a more detailed scale using video and still cameras. Finally, the structure and functioning of benthic habitats at the organism scale are studied using core samples of the seafloor. By linking the information from these three levels of scale, producing high resolution and broad scale habitat maps is achieved.

DISCLOSE is not the first project that aims to combine acoustic, photographic, videographic, and grab-sample information to create habitat maps. In [16] a similar approach of using acoustic data in conjunction with video data and grab-samples was used to explore and map cold water reefs in the United Kingdom's economic zone of the North Sea. Jordan *et al.* [17] created detailed bathymetry and sediment maps of the New South Wales coast in Australia, using extensive video footage from a towed video system as well as single beam echo sounder and grab-sample data to create habitat maps. Between 2004 and 2008 there was a European project for mapping seabed habitats called MESH [18]. With regards to habitat mapping, the MESH project produced Bathymetric Position Index maps with a resolution of 200 × 200 m and combined these with the known sediment distribution, based on grab-sample data. Currently the European Marine Observation and Data Network (EMODnet) [19] is continuing the work started by MESH. They currently have habitat maps up to the European Nature Information System (EUNIS) Level 3[1] in the Dutch area of the North Sea.

In order to improve upon the work that has thus far taken place, a few key questions need to be answered. The first relates to the use of backscatter. The main acoustic system used for this research, the multibeam echosounder (MBES) (further introduced in Section 1.2), is capable of delivering both bathymetry, a measure of water depth, as well as backscatter, a measure of the intensity of the sound reflected back to the sonar from the seafloor. Bathymetry was used in some of the mentioned projects, but there is a need to go beyond bathymetry and also use backscatter-based classification to create links to habitats. Next, especially for

---

[1] A full description of the different levels is found in [20]. Level 3 includes the ”Main habitats” and is further described as ”These serve to provide very broad divisions of national and international application which reflect major differences in biological character. They are equivalent to the intertidal Sites of Special Scientific Interest (SSSI) selection units (for designation of shores in the UK) (Joint Nature Conservation Committee 1996) and can be used as national mapping units.”

the southern North Sea, which is a sandy environment with sand waves of multiple superimposed scales, spatial and geo-acoustic[2] resolutions need to be investigated. Finally, since full-coverage backscatter maps will not become available in the short term, methods to maximize the use of bathymetry data for classification purposes need to be explored. These are some of the areas where the DISCLOSE project contributes to the state of the art of modern benthic habitat mapping research.

1.2. Multi-disciplinary habitat mapping methods

From the perspective of acoustics, marine habitat mapping is a topic of intense research. This is in part due to the high performance of modern acoustic systems. Of these systems, an important one is the MBES. The MBES is a swath sonar that uses focused sound beams to acoustically ensonify a large number of very specific locations of the seafloor on a wide swath. When combined with a global positioning system (GPS) and a motion reference unit (MRU), the location being ensonified is not just known in relation to the vessel, but also geographically. In addition to delivering bathymetry, a measure of the water depth, MBES systems also deliver the collocated backscatter product. Both of these products are used in this thesis. MBES systems are also capable of delivering water column data. Brown *et al.* [11] lists 148 studies covering acoustic habitat mapping methodologies that were published in the decade prior to 2011. This indicates the level of research effort being expended on this topic. The results from the acoustic methods developed in this thesis are further linked to video and grab-sample data to create habitat maps.

Of the three different methods used in DISCLOSE, acoustic methods allow large areas of the seafloor to be sensed. Acoustic based mapping plays a similar role in the underwater world as satellite and airborne optical methods do terrestrially. The main reason for this, is that electromagnetic waves attenuate rapidly underwater, whereas, acoustic waves carry much further in water than they do in air. It could be said that the foundation for underwater acoustics was laid in 1826, when the speed of sound in water was accurately determined by Jean-Daniel Colladon and Charles Francios Sturm [22]. In 1916 Alexander Behm carried out the first tests to measure the depth of the seafloor using echo sounding [23]. Behm used small explosions as a sound source for his initial echo sounding. Around 1923 the Submarine Signal Company built a for-purpose fathometer to acoustically measure the water depth [24]. In 1964 the first Sonar Array Sounding System (SASS) was introduced [25]. This system made use of beam forming to create directivity in the sound signal. Beam forming is only possible when using multiple receive transducers. This allows the sensitivity of the system to be steered in desired directions. For many years the more simple single beam echo sounder (SBES) was widely used because they were more affordable, easier to operate, and the data they yielded was easier to store and process. A disadvantage of the single beam echosounder is that only a narrow swath of the seafloor is mapped at a time. In 1958 the first publication came forth that used the Side Scan Sonar (SSS) as a survey tool for seafloor mapping [26, 27]. The

---

[2] Geo-acoustic resolution: the scale at which different types of sediments can be resolved using a certain acoustic classification/characterization technique [21]

side scan sonar is a wide swath system, contrary to the SBES, and as such it covers a large area of the seafloor. However, due to the method of deployment (towed behind a ship close to the seafloor) and its construction (lack of a beam forming during signal reception) it is not suitable to use it as a bathymetry measuring tool. Starting in the 1960s, multi beam echosounders were developed for the US military [25]. The civilian versions lacked some of the capabilities of the military version at that time. However, in recent years MBESs have really come into their own for bathymetric measurements. In addition to bathymetry, the most recent systems also allow for the acquiring of collocated backscatter data. Especially in the last 20 years they became an integral and indispensable tool for habitat mapping [11]. For anything except the shallowest of water, they provide the means for a rapid and large-scale overview of the seafloor.

Acoustic methods are not the only area that has seen a recent surge in research effort. Mallet and Pelletier [12] compared 60 years of video techniques for shallow (< 100 m depth) salt water environments. In their literature review they found 182 peer reviewed papers on this topic, 67% of which were published in the decade prior to 2014. They too cite the improvement in technology, improvements in sensor technology, improvements in battery life, and information storage capacity as reasons why video techniques are now more readily employed.

The method of benthic study that has been used the longest is that of grab sampling. The Dutch government has gathered this kind of data in the MWTL *(Monitoring waterstaatkundige toestand des lands)* program since 1995 [13–15]. In the North Sea, grab samples have been used for much longer for the study and mapping of habitats, some as early as 1773 [28].

1.3. Research objectives

The main focus of this thesis is to investigate the role of acoustic measurement techniques for habitat mapping. The study area is limited to the Dutch sector of the North Sea. Here, much of the previous research in acoustic mapping has focused on the area of the Cleaver bank. One objective of this thesis is to expand the areas for which the relationship between backscatter and the seafloor type is well understood. A big portion of the southern North Sea is covered with sandy sediment. Furthermore, the typical topography of this area is that of sand waves of various sizes superimposed on top of each other. The applicability of backscatter-based classification in these kinds of environments is thus investigated.

In a sand-wave environment, the question of resolution is important. This is because a detailed geographic resolution is needed in order to distinguish differences at the scales of small sand waves, called megaripples. These megaripples in the southern North Sea have a wavelength of a few tens of meters. Therefore, to find sediment or habitat patterns on these megaripples a spatial classification resolution well below 10 m is needed. However, this is not the only resolution criterion that is of importance. Geo-acoustic resolution is also important. This is because the main sediment for the seafloor is expected to be sand, and a high geo-acoustic resolution would allow small changes in sediment type to be distinguished for different parts of the megaripple. In this thesis it is investigated if sufficient spatial and geo-acoustic resolutions can be achieved to detect patterns of sediment distributions on different parts of megaripples.

It is also investigated how much of an effect and what kind of effect very small-scale sand ripples have on backscatter. These small sand ripples are often visible in video data but are not captured in MBES bathymetry data. To carry out backscatter-based classifications in sand-wave areas, these affects need to be understood. It is further investigated if backscatter can be used to determine the shapes and orientations of sand ripples that do not show up in the bathymetry.

One of the most common data types that is used for seafloor classification in acoustics is backscatter. However, currently large gaps in backscatter coverage exist in the North Sea. It is not known when full-coverage backscatter of the North Sea in the Dutch sector will become available. However, the Hydrographic Service of the Royal Netherlands Navy collects bathymetric data for the entirety of the Dutch sector of the North Sea on regular intervals. Therefore, it is investigated if a classification method can be developed that is applicable for those areas of the North Sea where backscatter is not available but bathymetric data is available.

Finally, it is investigated how to best link acoustic seafloor data to habitat data such as video and grab-sample data. The end goal of the acoustic mapping is to create maps not just of the bathymetry or sediment type, but to map the habitats of the seafloor in full coverage and in high detail. It is important for future projects that DISCLOSE creates links between these methods.

1.4. Thesis outline

This thesis is structured in the following way. In Chapter 2 the basics of acoustic methods and the theory needed for a good understanding of the rest of the thesis is discussed.

In Chapter 3 a dataset from the Brown Bank area of the North Sea is used for seafloor classification in a sand-wave environment. This area of the seafloor has sand waves of multiple scales. The first of these is the tidal ridge. These structures have a wavelength of 10 or more kilometers. Superimposed on the tidal ridges are sand waves. Sand waves have a wavelength from a hundred to a few hundred meters. Additionally, there is a still smaller seafloor structure, the megaripple, which has a wavelength of a few tens of meters. In previous research it has been shown that the sediment changes from the crest of a tidal ridge to the trough of a tidal ridge [29]. In this research it is investigated if the sediment changes at the scales of sand waves and megaripples. It is also in this chapter where the question of resolutions is addressed. Based on the results within this chapter, guidelines for future monitoring programs are indicated. If there is a significant change in sediments at the scale of the megaripple, then video- and grab-sampling geo-referencing need to be at a resolution better than the wavelength of a megaripple in order to create accurate habitat maps.

In Chapter 4 another dataset, again from the Brown Bank area of the North Sea, is used. This dataset contains acoustic data with multiple and different frequencies. For the analysis, the angular response curves (ARCs) of the MBES backscatter data were used. These curves consider the backscatter intensity as a function of the angle between the seafloor and direction of the incoming acoustic waves. The ARCs contain unexpected peaks that do not coincide with nadir, which is directly below the survey vessel. These peaks in the ARCs are caused by very small sand ripples on the seafloor. The size of these sand ripples is so small that they cannot be detected in the bathymetric data. It is found that not only can the sand ripples be detected in the backscatter data, but that the orientation of the sand ripples can also be detected. For the first time, acoustic evidence confirms that these small-scale sand ripples change direction with the changing of the tide, i.e., on a six hour cycle. The acoustic results are validated with video ground truth data. The results from this chapter indicate a large-scale change of the top few centimeters of the seafloor four times per day, and that these changes can be mapped by use of MBESs, not through bathymetry, but through backscatter.

In Chapter 5 full coverage habitat mapping, despite gaps in backscatter data coverage, is addressed. Datasets from Norwegian waters as well as from Dutch waters are used in order to develop a method to classify the seafloor using bathymetry and bathymetric derivative image layers. The developed methods do not rely on the use of backscatter in order to classify the seafloor. These results are important, because this method could be extended to cover the entire Dutch Continental Shelf (DCS). Older legacy data, and high-quality bathymetry data from the Hydrographic Service could then be utilized even further than they are now.

In Chapter 6 all of the acoustic methods described in the previous chapters are used and linked to data from video camera and grab samples. As such, links are established between acoustic mapping and the biology of the seafloor to produce habitat maps.

Finally in Chapter 7 the conclusions for the thesis are presented. It is also discussed how these findings relate to and are practically applicable in the real world. Their value to society as a whole and more particularly to the Netherlands, in the mapping of our resources, especially that of our benthic habitats, is discussed.

References

[1] T. D. Kendrick, *A History of the Vikings* (Courier Corporation, 2004).

[2] D. Melleno, *North Sea networks: Trade and communication from the seventh to the tenth century,* Comitatus: A Journal of Medieval and Renaissance Studies **45**, 65 (2014).

[3] H. Sornn-Friese, *Transactions and interactions-the flow of goods, services, and information,* (2008).

[4] G. Glegg, R. Jefferson, and S. Fletcher, *Marine governance in the English Channel (La Manche): Linking science and management,* Marine Pollution Bulletin **95**, 707 (2015).

[5] B. S. Halpern, S. Walbridge, K. A. Selkoe, C. V. Kappel, F. Micheli, C. D'Agrosa, J. F. Bruno, K. S. Casey, C. Ebert, H. E. Fox, R. Fujita, D. Heinemann, H. S. Lenihan, E. M. P. Madin, M. T. Perry, E. R. Selig, M. Spalding, R. Steneck, and

R. Watson, *A global map of human impact on marine ecosystems,* Science **319**, 948 (2008), https://www.science.org/doi/pdf/10.1126/science.1149345 .

[6] R. O. Amoroso, C. R. Pitcher, A. D. Rijnsdorp, R. A. McConnaughey, A. M. Parma, P. Suuronen, O. R. Eigaard, F. Bastardie, N. T. Hintzen, F. Althaus, S. J. Baird, J. Black, L. Buhl-Mortensen, A. B. Campbell, R. Catarino, J. Collie, J. H. Cowan, D. Durholtz, N. Engstrom, T. P. Fairweather, H. O. Fock, R. Ford, P. A. Gálvez, H. Gerritsen, M. E. Góngora, J. A. González, J. G. Hiddink, K. M. Hughes, S. S. Intelmann, C. Jenkins, P. Jonsson, P. Kainge, M. Kangas, J. N. Kathena, S. Kavadas, R. W. Leslie, S. G. Lewis, M. Lundy, D. Makin, J. Martin, T. Mazor, G. Gonzalez-Mirelis, S. J. Newman, N. Papadopoulou, P. E. Posen, W. Rochester, T. Russo, A. Sala, J. M. Semmens, C. Silva, A. Tsolos, B. Vanelslander, C. B. Wakefield, B. A. Wood, R. Hilborn, M. J. Kaiser, and S. Jennings, *Bottom trawl fishing footprints on the world's continental shelves,* Proceedings of the National Academy of Sciences **115**, E10275 (2018), https://www.pnas.org/content/115/43/E10275.full.pdf .

[7] K. J. Van der Reijden, N. T. Hintzen, L. L. Govers, A. D. Rijnsdorp, and H. Olff, *North Sea demersal fisheries prefer specific benthic habitats,* PloS one **13**, e0208338 (2018).

[8] K. W. Glennie, *Petroleum Geology of the North Sea: Basic concepts and recent advances* (John Wiley & Sons, 2009).

[9] J. Rice, C. Arvanitidis, A. Borja, C. Frid, J. G. Hiddink, J. Krause, P. Lorance, S. Áki Ragnarsson, M. Sköld, B. Trabucco, L. Enserink, and A. Norkko, *Indicators for sea-floor integrity under the European marine strategy framework directive,* Ecological Indicators **12**, 174 (2012), marine Benthic Indicators.

[10] L. Mayer, M. Jakobsson, G. Allen, B. Dorschel, R. Falconer, V. Ferrini, G. Lamarche, H. Snaith, and P. Weatherall, *The nippon foundation—GEBCO seabed 2030 project: The quest to see the world's oceans completely mapped by 2030,* Geosciences **8**, 63 (2018).

[11] C. J. Brown, S. J. Smith, P. Lawton, and J. T. Anderson, *Benthic habitat mapping: A review of progress towards improved understanding of the spatial ecology of the seafloor using acoustic techniques,* Estuarine, Coastal and Shelf Science **92**, 502 (2011).

[12] D. Mallet and D. Pelletier, *Underwater video techniques for observing coastal marine biodiversity: a review of sixty years of publications (1952–2012),* Fisheries Research **154**, 44 (2014).

[13] M. Bogaart-Scholte, M. van der Weijden, A. Naber, and M. Roos, *MWTL Meetplan 2014–Monitoring waterstaatkundige toestand des lands milieumeetnet rijkswateren chemie en biologie,* Rijkswaterstaat Waterdienst, Lelystad (2014).

[14] P. D. Van Denderen, N. T. Hintzen, A. D. Rijnsdorp, P. Ruardij, and T. van Kooten, *Habitat-specific effects of fishing disturbance on benthic species richness in marine soft sediments,* Ecosystems **17**, 1216 (2014).

[15] K. J. van der Reijden, L. L. Govers, L. Koop, J. H. Damveld, P. M. J. Herman, S. Mestdagh, G. Piet, A. D. Rijnsdorp, G. E. Dinesen, M. Snellen, and H. Olff, *Connecting the dots: a multi-scale, multi-resolution approach to marine habitat mapping,* .

[16] J. M. Roberts, C. Brown, D. Long, and C. R. Bates, *Acoustic mapping using a multibeam echosounder reveals cold-water coral reefs and surrounding habitats,* Coral Reefs **24**, 654 (2005).

[17] A. Jordan, P. Davies, T. Ingleton, E. Mesley, J. Neilson, and T. Pritchard, *Seabed habitat mapping of continental shelf waters of nsw,* NSW Department of Environment Climate Change and Water Occasional Paper Series **209** (2010).

[18] EMODnet, *Mesh archive on EMODnet,* Online (2021), accessd on 24-06-2021.

[19] EMODnet, *What is EMODnet? Your gateway to marine data in Europe,* Online (2021), accessed on 24-06-2021.

[20] D. Connor, J. Allen, N. Golding, K. Howell, L. Lieberknecht, K. Northen, and J. Reker, *The marine habitat classification for Britain and Ireland version 04.05,* (2005).

[21] E. Alevizos, M. Snellen, D. G. Simons, K. Siemes, and J. Greinert, *Acoustic discrimination of relatively homogeneous fine sediments using Bayesian classification on mbes data,* Marine Geology **370**, 31 (2015).

[22] R. B. Lindsay, *The story of acoustics,* The Journal of the Acoustical Society of America **39**, 629 (1966).

[23] P. Wille, *Sound images of the ocean: in research and monitoring* (Springer Science & Business Media, 2005).

[24] M. Lasky, *Review of undersea acoustics to 1950,* The Journal of the Acoustical Society of America **61**, 283 (1977).

[25] M. F. Glenn, *Introducing an operational multi-beam array sonar,* The International Hydrographic Review (1970).

[26] W. Chesterman, P. Clynick, and A. Stride, *An acoustic aid to sea bed survey,* Acta Acustica united with Acustica **8**, 285 (1958).

[27] M. Somers and A. Stubbs, *Sidescan sonar,* in *IEE Proceedings F-Communications, Radar and Signal Processing*, Vol. 131 (IET, 1984) pp. 243–256.

[28] C. J. Frid, K. Harwood, S. Hall, and J. Hall, *Long-term changes in the benthic communities on North Sea fishing grounds,* ICES Journal of Marine Science **57**, 1303 (2000).

[29] T. A. van Dijk, J. A. van Dalfsen, V. Van Lancker, R. A. van Overmeeren, S. van Heteren, and P. J. Doornenbal, *Benthic habitat variations over tidal ridges, North Sea, the Netherlands,* in *Seafloor Geomorphology as Benthic Habitat* (Elsevier, 2012) pp. 241–249.

2
Background and theory

Only a few know, how much one must know,
to know how little one knows.

Werner Heisenberg

What we know is a drop,
what we don't know is an ocean.

Isaac Newton

2.1. Introduction

The work presented in this thesis fits into a rich history of research in a very active field of study. Therefore, in this chapter, the theory that is relevant to the work in the remaining chapters is presented. A major part of this chapter will focus on the necessary theory related to the functioning of multibeam echosounders (MBESs).

Due to the rapid attenuation of electromagnetic waves underwater, the most common method used to map large areas of the seafloor is that of acoustic methods. Sonars have come along way since their first introduction in the 1920s [1]. Today's multibeam echosounders are precision instruments often operating at multiple frequencies gathering detailed information from a wide swath of seafloor. They will deliver products such as bathymetry, backscatter, and water column information. To determine how to interpret the MBES measurements regarding seafloor properties, the physics of sound traveling through water, how the water column affects the sound, how it interacts with the seafloor, and other factors all need to be taken in account. These are some of the items that are considered this chapter.

2.2. Multibeam Echosounders

The idea of the MBES first came from developmental land mapping radars of the US military. These radars used a Mills Cross technique, named after the Australian radio astronomer Bernard Mills, to beam form (more on beam forming later in the chapter) radar signals. Although the plan for the radars did not pan out, the Mills

Cross technique was adopted by *General Instrument* engineers who developed a Bottom Mapping Sonar (BOMAS) in collaboration with the US Navy [2]. Later this BOMAS system came to be known as the Sonar Array Sounding System (SASS). From the first SASS test system in 1964 [3, 4] until 1974 these systems and the data they generated remained largely classified. In 1977 the first operational non-military MBES, the Sea Beam ”Classic”, entered service on the French vessel *Jean Charcot* [2]. These early systems were largely deep water systems, instead of shallow water systems, with frequencies ranging from 12 to 30 kHz. In the years following, shallow water MBES systems were developed. By 1984 shallow water MBES systems were used for mapping and inspection for the offshore oil and gas industry [5].

Initial interest in MBES systems and the data they produce was based on military needs for submarine and missile navigation [2, 4]. Ocean engineering applications soon also made use of the technology, initially for the laying of deep sea cables. The driving force for systems for shallower waters with higher frequencies came from oil and gas exploration needs [4]. More recently, interest in habitat mapping has increased [6], as well as the use of backscatter for seafloor classification [7].

Today’s multibeam echosounders and the way they are employed are a far cry from the original *SeaBeam Classic* with its 16 beams and 45° swath coverage angle. This is due to both the decades of design and production improvements and also to the massively more powerful computers available today. It is common for modern MBESs to have over a thousand beams, swath opening angles up to 160°, as well as dual swath modes. In addition to delivering data from the seafloor, modern MBES systems can also deliver water column data. Water column data is not yet in wide spread use due to file size and compute power constraints. In terms of backscatter, the recent capability to acquire backscatter data at multiple frequencies in a single pass is particularly welcomed by the habitat mapping community [8–11].

There are three main types of MBES data, as follows:

- Bathymetry
- Backscatter
- Water column.

Bathymetry is the measure of the water depth. Bathymetry is generated by measuring the travel time of acoustic pings that are beamformed during both the transmit and receive operations. Backscatter refers to the intensity of the return signal. Both of these will be thoroughly covered in the following sections. The third of the above data types, water column data, is a record of the backscatter intensity not just around the time that the ping, for a given beam, reaches the seafloor, but for the entire time the ping travels through the water column. This datatype is not considered in this thesis.

2.2.1. General functioning

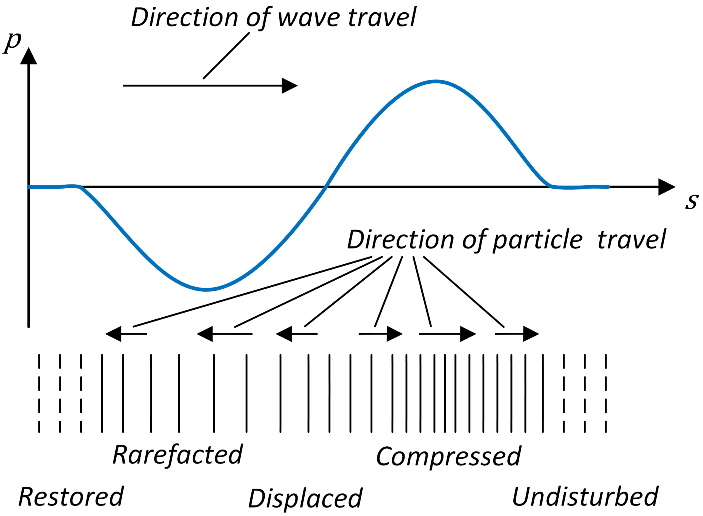

Figure 2.1: Fluid particle positions with the passage of a sine wave. s is the axis along which the wave travels. p indicates the amplitude of the compression wave (also known as acoustic pressure). Small arrows indicate the direction of particle movement. The spacing in the vertical lines indicates the state of particle density as the wave passes. Figure after [12]

Sound propagation

In order to understand the operation of MBES systems, the principles of sound and sound propagation need to first be addressed. Sound, is of course, what we perceive with our ears, but is broader than just what we can hear. It also applies to pressure waves with frequencies lower than what we can hear (*infrasound*) or higher than what we can hear (*ultrasound*). Sound in a medium is a matter of a traveling pressure wave (Figure 2.1).

Sound, or acoustic disturbances, are perturbations to an ambient state in a fluid that can be characterized by the values p_0 and ρ_0. Where p is the pressure and ρ is the density. By using the principle of the conservation of mass and Newtons second law, neglecting higher order terms, and equating p and ρ, the linear Wave equation [12]

$$\nabla^2 p = \frac{\partial^2 p}{\partial x^2} + \frac{\partial^2 p}{\partial y^2} + \frac{\partial^2 p}{\partial z^2} = \frac{1}{c^2}\frac{\partial^2 p}{\partial t^2} \tag{2.1}$$

is derived. Where ∇^2 it the Laplacian, the sum of the second derivatives related to the (x, y, z) directions of a three dimensional Cartesian coordinate system, p is the pressure of the propagating wave.

For many applications related to the modeling of underwater acoustics sound can be considered as a plane wave. As such, Equation 2.1 is considered only along a single direction s. The assumption is that all acoustic field quantities are such that they depend only on time t and s. With that, Equation 2.1 reduces to

$$\frac{\partial^2 p}{\partial s^2} = \frac{1}{c^2}\frac{\partial^2 p}{\partial t^2}. \tag{2.2}$$

Equation 2.2 can be factored to the following

$$\left(\frac{\partial}{\partial s} - \frac{1}{c}\frac{\partial}{\partial t}\right)\left(\frac{\partial}{\partial s} + \frac{1}{c}\frac{\partial}{\partial t}\right)p = 0 \tag{2.3}$$

because differential operators are commutable and therefore can be manipulated in algebraic fashion. Let p be a function of $\xi = t - s/c$ and $\eta = t + s/c$. Then $\partial/\partial t = \partial/\partial\xi + \partial/\partial\eta$ and $\partial/\partial s = -(1/c)(\partial/\partial\xi - \partial/\partial\eta)$, and with that the wave equation becomes

$$-\frac{4}{c^2}\frac{\partial}{\partial\xi}\frac{\partial}{\partial\eta}p = 0. \tag{2.4}$$

The general solution of Equation 2.4 is a sum of a function of $\xi = t - s/c$ and $\eta = t + s/c$ as follows

$$p(s,t) = f(t - s/c) + g(t + s/c) \tag{2.5}$$

where both f and g are arbitrary functions [12].

In the case where the acoustic wave is a plane harmonic wave then

$$p(s,t) = p_0 e^{i(ks - \omega t)} \tag{2.6}$$

is a solution, where p_0 is the amplitude, ω is the radial frequency, and k is the wave number. Taking the real part of this equation yields the solution of the harmonic 1D wave equation as

$$p(s,t) = p_0 \cos(ks - \omega t). \tag{2.7}$$

Considering a spherical wave and using a polar coordinate system, Equation 2.1 becomes

$$\frac{\partial^2 (rp)}{\partial r^2} = \frac{1}{c^2}\frac{\partial^2 (rp)}{\partial t^2}. \tag{2.8}$$

where r is the radial distance from the source. The general solution is similar to Equation 2.5 as follows

$$rp(s,t) = f(t - s/c) + g(t + s/c). \tag{2.9}$$

Here g is the case where the wave moves towards the source, which is not possible. Considering again a harmonic wave, then the solution simplifies to

$$p(r,t) = \frac{A}{r}e^{i(kr - \omega t)} \tag{2.10}$$

For most cases of sound modeling related to MBES systems either the radial coordinate systems or the plane wave system is used. Sound from sources in the water will propagate spherically. At a certain point the curvature of the sphere is small enough relative to the wave length to where the sound front can be considered to be a plane wave.

The above explains some of the basic physics related to sound propagation underwater as is needed for an understanding of the functioning of MBES systems. The interested reader is directed to [12] and [13] and the references therein for a more detailed discussion.

Speed of sound in water

The speed of sound in the water (a fluid) is given by

$$c = \sqrt{\frac{B}{\rho}} \tag{2.11}$$

where B is the bulk modulus and ρ is the density [13].

The speed of sound in ocean water is dependent on the water temperature T, the depth z, and the salinity of the water S. Some of the earliest measures of the speed of sound in water were performed by François Sulpice Beudant (1816) and Jean-Daniel Colladon together with Charles Francios Sturm (1826) [13, 14]. Beudant performed the test close to Marseilles with an underwater bell and a swimmer who waved a flag when he heard the sound arrive. According to his measurement, the speed of sound was $1,500 m/s$ Colladon and Sturm used an underwater bell in lake Geneva and a boat in the water to listen for the arrival of the sound. A gunpowder flash coinciding with the striking of the bell was used to start the clock. According to their measurement the sound speed was $1,435 m/s$ (consistent with modern expectations, given the water temperature that they measured to be 8 °C). Interestingly, the purpose of their measurement was to confirm calculations of water compressibility [14]. Starting in the 1920s accurate tables of the sound speed became available [13] giving these parameters [15], and were improved upon by Kuwahara [16] in 1939. Medwin [17] proposed an empirical formula for the speed of sound in the water based on these tables. The formula is given by

$$c = 1449.2 + 4.6T - 0.055T^2 + 0.00029T^3 + (1.34 - 0.01T)(S - 35) + 0.016z \tag{2.12}$$

where

- T is the water temperature in °C.
- z is the depth in m.
- S is the salinity of the water in parts per thousand (ppt).

For accurate bathymetry measurements with MBESs, the sound speed is needed for the entire water column [18]. To measure the sound speed profile of the water column there are two kinds of systems. The first of these, called a CTD probe, measures the conductivity, temperature, and pressure. From these the salinity, temperature and depth are determined which in turn are used to determine the sound speed profile. The second device uses a small transducer sending a pulse of sound that is reflected back to the transducer. By knowing the exact distance of the reflector plate the speed of sound is directly measured.

Either of these devices is lowered to the seafloor during which time it continuously carries out measurements to create a sound speed profile of the entire water column. In deeper water, the sound speed sensor may be lowered through the thermocline(s) until the remainder of the sound profile can be accurately estimated because the main changing parameter is the depth and thus the pressure.

Beamforming

All modern MBES systems use the principle of acoustic beamforming in order to both focus the emission of the sound as well as when receiving the sound that returns from the seafloor. This beamforming is how the depth and backscatter measurements are known to come from a specific location of the seafloor. Because of the important role of beamforming in modern sonars, the theory will be treated here.

Beamforming is an interference phenomenon. Consider the case where there are two sound sources located on the x-axis of a 3-D Cartesian space separated by some distance L_x. Let's further assume that these sources emit the same signal at the same time. On the axis perpendicular to L_x and located in the middle between the two sources, the two signals are in phase, thus resulting in a doubling of the pressure. At other angles, a variety of situations can occur ranging from full constructive to full destructive interference. This is the basic principle of beamforming during the active part of the sonar operation.

During the receive phase of the ping cycle, beamforming is also carried out. Assume now that the receive array of the MBES is an array of hydrophones on the y-axis of the above mentioned Cartesian space. Figure 2.2 shows an example with M hydrophones m_ℓ $(\ell = 0, 1, 2, ..., M-1)$ each offset with a distance δy from the previous hydrophone. Let the total length of the array being L_y. Let us further assume that the wavefront can be considered to be a plane wave. Then the summed output of these hydrophones would be maximized if the plane wave arrives from a direction perpendicular to the hydrophone array. Assume the wave arrives not from the perpendicular direction but rather with an offset angle θ from the perpendicular. Let us further consider the hydrophone m_0 to be the reference hydrophone. Let the distance between the wave front and some hydrophone m_ℓ be d_{m_ℓ} (Figure 2.2). For simplicity, let us consider only the point in time when the wave front arrives at m_0 i.e. $d_{m_0} = 0$. Then the relationship

$$\sin(\theta) = \frac{d_{m_\ell}}{\ell \delta y} \quad for\ \ell = 0, \dots, M-1 \tag{2.13}$$

holds true. The time delay of the arrival of the wavefront at the other hydrophones is expressed as

$$t_\ell = \frac{d_{m_\ell}}{c} \quad \ell = 0, \dots, M-1. \tag{2.14}$$

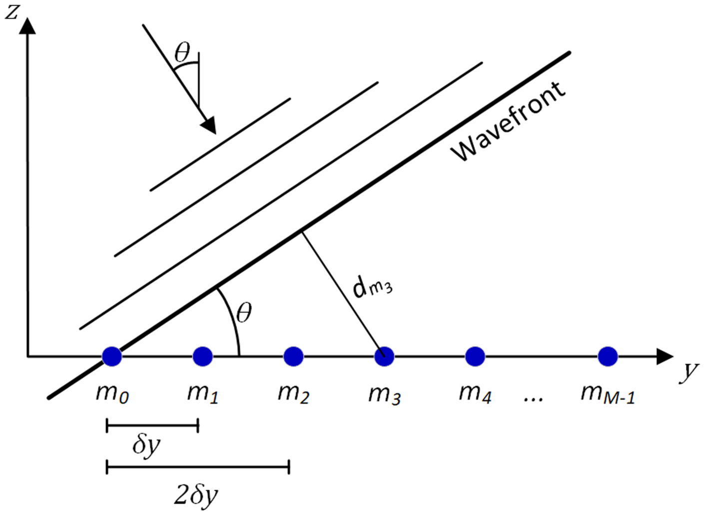

Figure 2.2: Schematic of a plane wave impinging on a line array of M equally spaced hydrophones with an angle θ.

With that, the phase delay at the array elements is as follows

$$\Delta\varphi_\ell = \omega t_\ell = \frac{2\pi}{\lambda} d_{m_\ell} = \frac{2\pi\ell\sin(\theta)\delta y}{\lambda} \tag{2.15}$$

where ω is the angular frequency such that the following holds $\omega = 2\pi f$, f is the frequency of the acoustic wave, and λ is the acoustic wavelength. Equation 2.15 can be rewritten in complex notation such that the phase delay is

$$\Delta\varphi_\ell = e^{i2\pi\frac{\sin(\theta)}{\lambda}\ell dy}. \tag{2.16}$$

With that, the acoustic array response to the incoming wave arriving from angle θ is given by the sum

$$G(\theta) = \sum_{\ell=0}^{N-1} e^{i2\pi\frac{\sin(\theta)}{\lambda}\ell dy}. \tag{2.17}$$

Equation 2.17 indicates the sensitivity of an array to sound coming from a given direction θ which is not directly in front of the array. In order to know the sensitivity of an array to an incoming wave from direction θ while steered towards ϕ the term $\sin(\phi)$ needs to be added to Equation 2.17 as follows

$$G(\theta,\phi) = \sum_{\ell=0}^{N-1} e^{i\frac{2\pi}{\lambda}(\sin(\theta)-\sin(\phi))\ell dy}. \tag{2.18}$$

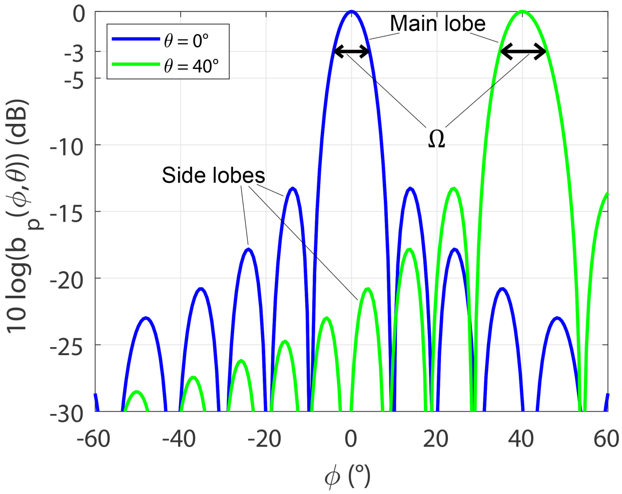

Figure 2.3: Illustration of beam patterns for a simulated array of length L_y = 0.1 m, with 512 equally spaced hydrophones. Indicated are the beam patterns for both an unsteered array (shown in blue), and an array steered towards 40° (shown in green). Both main lobes and side lobes are visible. The beam opening angle is shown for both cases by Ω, as typically measured at -3 decibels.

From this, the beam pattern [13] $b_p(\theta, \phi)$ is easily calculated as the squared magnitude of the normalized array response by

$$b_p(\theta, \phi) = \left| \frac{\sum_{\ell=0}^{N-1} e^{i\frac{2\pi}{\lambda}(\sin(\theta)-\sin(\phi))\ell dy}}{M} \right|^2 . \tag{2.19}$$

An example beam pattern is presented in Figure 2.3 (in decibel units) for a simulated array of length $L_y = 0.1$ m with 512 equally spaced hydrophones. The beam pattern is shown for both an unsteered array ($\phi = 0$) (in blue) as well as a steered array towards $\phi = 40°$ (in green) for a simulated frequency of 90 kHz. The beam width Ω is defined by the width of the beam at the -3 dB sensitivity level. As is visible in Figure 2.3 the beam width of the steered beam is wider than the unsteered beam. This is due to the effective array length being shorter when the array is steered. The amount of the beam width increase is $1/cos(\phi)$. In addition to the main lobe there are side lobes as well. These are directions to which the array is also sensitive. For the simulated array shown in Figure 2.3 none of the side lobe levels have a sensitivity of 0 dB. A side lobe level of 0 dB sensitivity is also referred to as a grating lobe. The locations and sensitivities of the side lobes depend on the array geometry. Because side lobes are not desired, they are often reduced by weighting the contribution of array elements. The disadvantage to such weighting is the widening of the main lobe.

In a manner similar to the steering of the receive array the send array can also be steered by introducing a delay for some of the transducer elements. This is done in order to have a more even spacing of soundings in the along track direction. In practice, there are various ways implemented by the different sonar manufacturers for such beam steering during the pinging cycle. Because of the breadth of this topic, the interested reader is referred to [19] for a deeper look at the various aspects of transmit beam steering and their impacts on sonar operations.

Auxiliary Sensors

Thus far, the operation of the MBES has been discussed. But there are a few additional sensors that are needed in order to get a good bathymetric measurement. The first of these is a global positioning system (GPS). A GPS is a satellite based radio navigation system. The precise position of the satellites as they relate to the earth is known by the use of ground base stations. Using the travel time of radio signals from multiple satellites, a GPS receiver calculates its precise global position. To get the best measurements for surveying, two GPS receivers are typically mounted high on a ship’s mast, so they will have a direct line of sight to the satellites above. The location of the GPS receivers, relative to the sonar must be known, and the offsets accounted for.

To account for those offsets, a motion reference unit (MRU) is used to constantly and precisely measure the roll, yaw, pitch, and heave of the vessel. The MRU is typically installed close to the ship’s center of gravity. In addition to the offsets between the GPS receivers and the MBES, the offsets between these two systems and the MRU are also very precisely measured.

With these two systems, it is possible to very accurately determine the exact horizontal position of the MBES at all times. It is a little more complicated to get precise vertical position, since typical GPS accuracy in the vertical direction is in the range of 0.5 m. If the survey takes place closer to shore then an additional RTK system is used to improve the vertical measurement accuracy. Another method is to measure the draft of the vessel (more specifically the MBES), and correct for the influence of the tide to get an accurate and unchanging bathymetric measurement.

2.2.2. Bathymetry

Given the theory of underwater sound propagation and the methods of beamforming and global positioning that have thus far been established, the core products delivered by multibeam echosounders (MBESs) can now be discussed. One of the main products of MBES systems is the water depth, or bathymetry, which is surveyed in swaths. By sailing ”lawn mower patterns” (optimizing sailing patters for (autonomous) surveying is a topic of research [20]) full coverage of the seafloor is achieved. In this way the point cloud, from which the digital terrain model of the seafloor is generated, is established.

With the accurate position and orientation of the MBES known, the beam angle θ is also known. Furthermore the speed of sound c in the water column is known. From the MBES the two-way travel time t is then measured. From this, the across track distance y is known as well as the water depth d (Figure 2.4). These can be expressed as

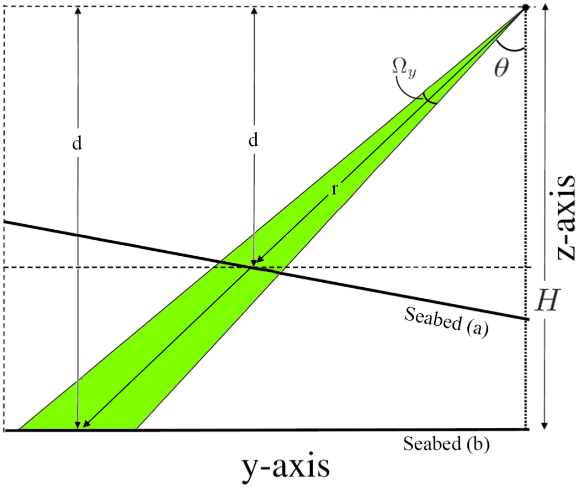

Figure 2.4: Across-track cross section of an oblique beam of a multibeam echosounder for a sloping seafloor (a) and a flat seafloor (b). The range r from the sonar to the seafloor, and the depth d are also shown (figure after [21] and [22]).

$$d = r\cos(\theta) \tag{2.20a}$$

$$y = r\sin(\theta) \tag{2.20b}$$

where r is calculated using the two-way travel time and the speed of sound as

$$r = \frac{ct}{2}. \tag{2.21}$$

The above holds true assuming that the sound speed is constant. However, as seen from Equation 2.12 the sound speed depends on the temperature, depth, and salinity. There are two affects that need to be considered. Firstly, the range r can be affected by a changing sound speed. For this problem a reasonable accuracy can be achieved by using the average sound speed in the water column. But the additional problem is that the sound ray is refracted, and as such, changes direction. This is especially true for the beams pointing away from nadir. To account for this, ray tracing needs to be implemented in order to assign the correct location of the beam footprint on the seafloor. The fundamental theory employed in ray tracing is Snell's law [23, 24]

$$\frac{\sin(\theta_1)}{c_1} = \frac{\sin(\theta_2)}{c_2} = k_0 \tag{2.22}$$

where θ_1 is the ray angle in one medium with a sound speed of c_1, θ_2 is the ray angle in the second medium with a sound speed of c_2, and k_0 is a constant. Snell's law holds for the water to seabed interface, but it also holds in the case where the sound speed in water changes with changing depth. For ray tracing, Snell's law is applied some discrete number of times at different water depths, given a sound speed profile of the water column (The interested reader is directed to [18, 23, 24] for more information on this topic).

There are two general methods by which the (two-way) travel time, or the time with the sound arrives at the seafloor is detected [25]. The first of these is an amplitude detection and is used for beam angles close to nadir. The second method is a phase detection, and is used for oblique beam angles.

The amplitude detection method computes the center of gravity from the signal envelope as follows

$$t_D = \frac{\sum t_i a(t_i)}{\sum a(t_i)} \tag{2.23}$$

where a is the digitized sound signal and t_i the time sample. This signal is that of one beam of the MBES system. With the phase detection method, use is made of interferometry between two subsets of the receiving array [25]. For both of the sub-arrays, the signal is beam-formed for the desired beam angle. Because of the difference in distance from the return point on the seafloor to the centers of both sub-arrays there will be a phase difference between the signals that each of these sub-arrays receives. When the return signal comes from the expected angle, for which the sub-arrays are beam formed, then the phase difference between the two signals is zero. Thus, the zero-phase crossing is the correct arrival time. The phase difference $\widehat{\Delta\varphi}$ is calculated with

$$\widehat{\Delta\varphi} = arg\left\{S_A S_B^*\right\} \tag{2.24}$$

where S_A is the signal envelope of the first sub-array, and S_B^* is the complex conjugate signal of the second sub-array [26]. Because the return signal is often noisy, and therefore the phase difference ramp(s) are noisy, a low order polynomial is fitted to the phase difference measurement to improve the bottom detection. Because there may be many phase ramps limited between $-\pi$ and π, the correct phase ramp is chosen using the center of gravity of the signal envelope, as used for the amplitude detect method. The interested reader is refereed to [25] and [26] for a more detailed discussion of bottom detection methods.

2.2.3. Backscatter

Until this point only the depth measurement delivered by MBES systems has been discussed. The bathymetric measurement depends on the range detection based on the two-way travel time. This measurement is performed on the portion of the sound signal that, after interacting with the seafloor and scattering, scatters back in the direction from which it came, toward the sonar (Figure 2.5). Another term for this portion of the sound signal is the backscatter. In addition to just measuring the travel time, the intensity of this signal can also be measured to yield an additional information source on the seafloor. However, unlike the case where the only interest is the two-way travel time, which is nowadays relatively standard, as long as the

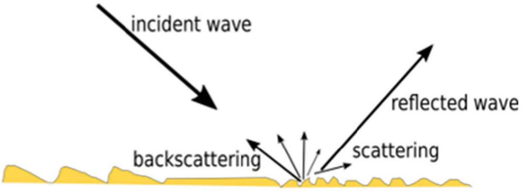

Figure 2.5: Reflection and scattering of an incident acoustic wave due to seafloor roughness.

signal to noise ratio is sufficient, an accurate measure and derivation of backscatter strength is more complicated.

In the context of seafloor mapping, it would be desirable that the resulting variation in backscatter is representative of only changes caused by differences in seafloor characteristics. For this to be the case, the absorption, refraction, and scattering of sound in the water column need to be accounted for. Another class of effects that needs to be controlled for is the internal sensitivity and processing of the signal in the MBES. For example, the source level SL of the active ping should be accurately known. The receiver sensitivities should also be calibrated. The analog to digital converters should operate without signal loss or distortion. The full sonar equation with the different contributors is given by [27]

$$BL_0 = SL + BP_T(\theta) - 2TL + BS_f(\beta) + 10\log_{10}(A) + SH + BP_R(\theta) + PG \tag{2.25}$$

where SL is the source level, BP_T is the beam sensitivity pattern during transmit, TL is the transmission loss. The following two terms relate to the target strength. The first, $BS_f(\beta)$ being the desired seafloor contribution of the backscatter which depends on the frequency and the grazing angle β. The second controls for the instantaneously ensonified area A. The next term, SH is the sensitivity of the receive array. A beam pattern correction per angle θ is included with the term $BP_R(\theta)$. Finally, PG is the gain introduced between the signal reception to what is recorded in the data files.

The above indicates the ideal situation where all imperfections can be corrected and the absolute backscatter strength is derivable. In practice it is often not possible to perform all of these corrections. Especially the corrections for sonar sensitivities are often hard to do, due to manufacturer confidentiality restrictions related to sonar construction specifics [28]. Sonar sensitivity is also known to change through the lifetime of a sonar [29]. As such, when absolute calibration of the sonar is not possible then relative values are often used to determine acoustic class relationships to the seafloor [28]. In such cases, the backscatter-based classification map is matched to ground truth data to determine the class relationships to seafloor characteristics.

2.2.4. Sound interaction with the seafloor

To consider how sound interacts with the seafloor, and thereby examine what the backscatter measurements indicate about the seafloor, let us first consider a simple case. The case of a plane wave arriving from some angle θ_1 interacting with the boundary between two mediums 1 and 2. Each medium will have respective parameters for density and sound speed ρ, c. Depending on the exact parameters, it is expected that there will be a reflection of the incoming wave away from the interface as well as an transmission of the wave from medium 1 to medium 2. The reflection for a wave arriving from angle θ_1 (with respect to normal) is expected to be in the direction of $-\theta_1$ (about normal to the plane). Given the continuity conditions, the part of the incident wave that is transmitted into medium 2 will obey Snell's law (Equation 2.22). With regards to the relationship between the incident, reflected and transmitted pressures, the coefficients for the reflection and transmission are expressed as

$$R(\theta_1) = \frac{\rho_2 c_2 \cos(\theta_1) - \rho_1 c_1 \cos(\theta_2)}{\rho_2 c_2 \cos(\theta_1) + \rho_1 c_1 \cos(\theta_2)} \tag{2.26a}$$

$$T(\theta_1) = \frac{2\rho_2 c_2 \cos(\theta_1)}{\rho_2 c_2 \cos(\theta_1) + \rho_1 c_1 \cos(\theta_2)} = 1 + R(\theta_1). \tag{2.26b}$$

Thus, there is a part of the incoming wave that is reflected, a part that is transmitted, but in the case of typical seafloors there is also a part that is absorbed by the second medium. This is accounted for by making the sound speed c complex by a complex wave number k. The complex sound speed then becomes

$$\tilde{c} = c - \frac{i\alpha_c |c|^2}{\omega} \tag{2.27}$$

where α_c is the absorption coefficient in nepers/m, and ω is the circular frequency. With this modification there will not be perfect reflection even for incident angles near normal.

The case that has been discussed thus far is an idealized case. If this was the case for the seafloor then the MBES would not function due to there being no backscatter. Thus, the phenomena of scattering needs to be considered.

How different surfaces affect the scattering of acoustic (or electromagnetic) waves has been covered extensively in numerous books such as [30–34]. A short introduction is provided below. Acoustic waves are scattered by irregularities in the seafloor [35]. These include the following.

- The roughness of the water sediment interface.
- Spatial variations in sediment physical properties.
- Discrete inclusions such as shell pieces, pebbles, or bubbles.

The main measure of backscattering that is of interest for classifying the seafloor is termed the backscatter strength $BS(\varphi_i)$. The backscatter strength is the dB form of the scattering cross section. The scattering cross section is, in turn, defined as the ratio of the intensity of the scattered sound I_s and the intensity of the incoming acoustic plane wave I_i in decibel units. The ratio is given by

$$S(\varphi_i) = \frac{I_s(\varphi_i)}{I_i(\varphi_i)}. \tag{2.28}$$

Here I_s is given relative to a unit area of 1 m^2 and at a distance of 1 m from this unit area. The angle between the seafloor and the direction from which the plane wave arrives at the area of the seafloor is φ_i (Grazing angle). The case given here is where I_s is measured for the direction of φ_i i.e. the backscatter direction. With that the backscatter strength $BS(\varphi_i)$ is defined as follows

$$BS(\varphi_i) = 10\log_{10}\left(\frac{I_s(\varphi_i)}{I_i(\varphi_i)}\right). \tag{2.29}$$

The backscatter strength BS is important as it relates to the characterization of the seafloor. However, in practice something is needed that is independent of the area that is instantaneously ensonified. This is called the Target Strength TS, and the relationship between the TS and the BS is as follows

$$TS(\varphi_i) = BS(\varphi_i) + 10\log_{10}\left(\frac{A}{A_0}\right) \tag{2.30}$$

where A is the instantaneously ensonified area and $A_0 = 1$ m ^{2} is the reference area.

In acoustics (although it was first used in optics [36]) Lambert's cosine law is often used as a simple model for the angle dependence of the backscatter strength [37]. Lambert's rule holds for rough seafloor surfaces. Consider a sound with intensity I_i arriving at the area A of seafloor in question from the angle φ_i. The power of this wave with respect to the seafloor is then $P_i = I_i A\sin(\varphi_i)$. According to Lambert's law the intensity I_s radiated in the direction of φ_s measured at a distance of 1 m is given by

$$I_s = \mu I_i A\cos(\varphi_i)\cos(\varphi_s) \tag{2.31}$$

where μ is a proportionality constant. When $\varphi_i = \varphi_s$, i.e. the backscatter direction, then Lambert's law written in dB values is

$$\begin{aligned} 10\log_{10}\left(\frac{I_s}{I_i}\right) &= 10\log_{10}(\mu) + 10\log_{10}(\cos(\varphi_i)\cos(\varphi_i)) \\ &= 10\log_{10}(\mu) + 20\log_{10}(\cos(\varphi_i)) = BS(\varphi_i). \end{aligned} \tag{2.32}$$

The term μ can be adjusted to account for both the frequency dependency as well as sediment geoacoustic properties. Experiments indicate that typical values for $10\log_{10}(\mu)$ range from -40 dB to -10 dB. A good first estimate value for $10\log_{10}(\mu)$ is -29 dB when using Lambert's rule for any given seafloor [38]. Lambert's law

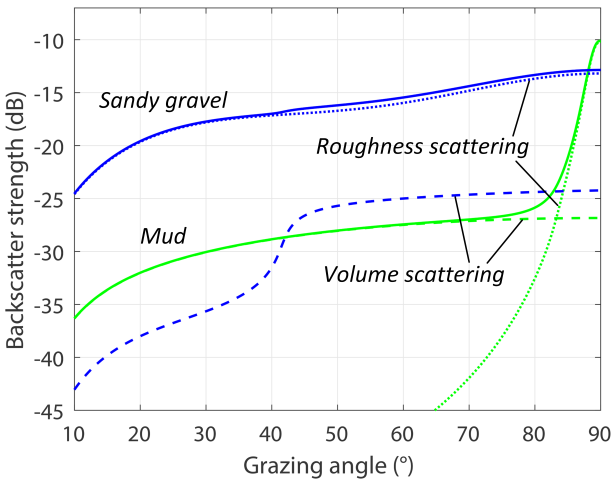

Figure 2.6: Backscatter strength according to the APL-model as a function of grazing angle for two seafloor types, Mud in the green, and Sandy gravel in blue. The contribution of volume scattering is shown in dashed lines and the contribution of roughness scattering is shown in dotted lines.

provides a good first approximation of backscatter intensity. For some seafloors, such as rock, Lambert's rule has been shown to provide a good estimate for the entire range of swath angles. For other seafloors, especially seafloors composed of fine sediments, it is only valuable for oblique grazing angles [38].

One of the more sophisticated models that is used for backscatter modeling was developed by Jackson [39], the so-called Applied Physics Laboratory of the Unversity of Washington (APL-UW) model. This model is valid for frequencies between 10 kHz and 100 kHz, although it is also referenced for higher frequencies [40]. This model has eight inputs, as follows

1. θ - The angle of incidence of the acoustic wave front, given in degrees.
2. f - The frequency of the ping, given in Hz.
3. ρ_r - Ratio of sediment mass density to water mass density, given in kg/m^3.
4. c_r - Ratio of sediment sound speed to water sound speed, given in m/s.
5. α - the sediment attenuation coefficient, given in dB/m.
6. γ - the spectral exponent of the sediment roughness.
7. η - the spectral strength of the sediment roughness.
8. $\hat{\sigma}_v$ - Volume scattering parameter.

The APL model further uses three sub-models, namely, the Kirchhoff Approximation, the Composite Roughness Approximation, and the Large-Roughness Scattering

Cross Section. The Kirchhoff approximation is used for angles within 50 degrees of normal and is valid for smooth to relatively smooth seafloors. The composite roughness approximation is valid for smooth to relatively smooth seafloors for angles away from normal. The Large-roughness scattering cross section is used for rougher seafloors such as gravel and rock, and is used for the entire range of angles. Interpolation is performed such that there are no jumps in the final result. Together, these models account for seafloor interface roughness and volume scattering from within the sediment (Figure 2.6).

2.2.5. Typical backscatter data processing steps

There are a number of backscatter processing steps that were performed prior to classification, in the following chapters. The exact processing steps depended on the sonar from which the data came. In the following chapters data is used that was collected by either Kongsberg or R2Sonic MBES systems. These two manufacturers log the backscatter data in different manners.

Both Kongsberg and R2Sonic apply a time varying gain (TVG) to counteract the decrease in signal intensity due to spherical spreading. This real time TVG application is needed in order to keep the signal in the sensitivity range of the digitizers. For both the Kongsberg and R2Sonic data, this TVG was removed and reapplied with absorption coefficients calculated by use of ocean conditions that were also measured during the respective cruises. At this point, the data processing differs between the data from the two systems.

R2Sonic stores the intensity data as digitized pressure units. These are converted to decibels. Next, because the transducer has different sensitivity for the different frequencies, these are corrected for. Then the data were corrected for user defined receiver gains.

Kongsberg implements a TVG, but does so assuming a flat seafloor. This TVG is removed from the data and a new TVG applied using the actual distance of travel information for each beam, and thus removing the assumption of the seafloor being flat.

Then for both systems a slope correction is performed as is discussed in more detail in Section 3.2.2. This slope correction is performed using the bathymetry data from the MBES. Having the corrected slopes allows corrected grazing angles to be known, which in turn ensures higher accuracy when applying angle specific classification such as the Bayesian classification method [21, 22] (Section 3.2.2). Having the correct seafloor slope also allows the BS to be adjusted for the correct ensonified area A, as done in Section 3.2.2. There are some instances, for example, for small seafloor features, where the slope correction fails. Chapter 4 illustrates a case in which slope correction does not work.

References

[1] M. Lasky, *Review of undersea acoustics to 1950,* The Journal of the Acoustical Society of America **61**, 283 (1977).

[2] A. E. Theberge Jr and N. Z. Cherkis, *A note on fifty years of multi-beam,* Hydro International **22** (2013).

[3] M. F. Glenn, *Introducing an operational multi-beam array sonar,* The International Hydrographic Review (1970).

[4] J. E. H. Clarke, *Multibeam echosounders,* in *Submarine geomorphology* (Springer, 2018) pp. 25–41.

[5] E. Hammerstad, A. Lovik, S. Minde, L. Krane, and M. Steinset, *Field performance of the Benigraph high-resolution multibeam seafloor mapping system,* in *OCEANS'85-Ocean Engineering and the Environment* (IEEE, 1985) pp. 682–685.

[6] C. J. Brown, S. J. Smith, P. Lawton, and J. T. Anderson, *Benthic habitat mapping: A review of progress towards improved understanding of the spatial ecology of the seafloor using acoustic techniques,* Estuarine, Coastal and Shelf Science **92**, 502 (2011).

[7] G. Lamarche and X. Lurton, *Recommendations for improved and coherent acquisition and processing of backscatter data from seafloor-mapping sonars,* Marine Geophysical Research **39**, 5 (2018).

[8] E. Vas, *Multispectral mode™ survey capability.* Online (2016).

[9] J. E. H. Clarke, *Multispectral acoustic backscatter from multibeam, improved classification potential,* in *Proceedings of the United States Hydrographic Conference, San Diego, CA, USA* (2015) pp. 15–19.

[10] T. Gaida, T. Tengku Ali, M. Snellen, A. Amiri-Simkooei, T. van Dijk, and D. Simons, *A multispectral Bayesian classification method for increased acoustic discrimination of seabed sediments using multi-frequency multibeam backscatter data,* Geosciences **8**, 455 (2018).

[11] C. J. Brown, J. Beaudoin, M. Brissette, and V. Gazzola, *Multispectral multibeam echo sounder backscatter as a tool for improved seafloor characterization,* Geosciences **9**, 126 (2019).

[12] A. D. Pierce, *Acoustics: an introduction to its physical principles and applications* (Springer, 2019).

[13] M. A. Ainslie, *Principles of sonar performance modelling*, Vol. 707 (Springer, 2010).

[14] R. B. Lindsay, *The story of acoustics,* The Journal of the Acoustical Society of America **39**, 629 (1966).

[15] D. J. Matthews, *Tables of the velocity of sound in pure water and sea water for use in echo-sounding and sound-ranging*, 2nd ed., Vol. 4 (Hydrographic Department, Admiralty, 1939).

[16] S. Kuwahara, *Velocity of sound in sea-water and calculation of the velocity for use in sonic sounding,* The International Hydrographic Review (1939).

[17] H. Medwin, *Speed of sound in water: A simple equation for realistic parameters,* The Journal of the Acoustical Society of America **58**, 1318 (1975).

[18] T. H. Mohammadloo, M. Snellen, W. Renoud, J. Beaudoin, and D. Simons, *Correcting multibeam echosounder bathymetric measurements for errors induced by inaccurate water column sound speeds,* IEEE Access **7**, 122052 (2019).

[19] X. Lurton, *Modelling of the sound field radiated by multibeam echosounders for acoustical impact assessment,* Applied Acoustics **101**, 201 (2016).

[20] J. Folkesson, I. Torroba, and N. Bore, *A comparison of submap registration methods for multibeam bathymetric mapping,* (2018).

[21] A. Amiri-Simkooei, M. Snellen, and D. G. Simons, *Riverbed sediment classification using multi-beam echo-sounder backscatter data,* The Journal of the Acoustical Society of America **126**, 1724 (2009).

[22] L. Koop, A. Amiri-Simkooei, K. J van der Reijden, S. O'Flynn, M. Snellen, and D. G Simons, *Seafloor classification in a sand wave environment on the Dutch continental shelf using multibeam echosounder backscatter data,* Geosciences **9**, 142 (2019).

[23] D. F. Dinn, B. D. Loncarevic, and G. Costello, *The effect of sound velocity errors on multi-beam sonar depth accuracy,* in *'Challenges of Our Changing Global Environment'. Conference Proceedings. OCEANS '95 MTS/IEEE*, Vol. 2 (1995) pp. 1001–1010 vol.2.

[24] J. Plaa, M. Snellen, and D. Simons, *Correcting bathymetry measurements for water sound speed effects using inversion theory,* The Journal of the Acoustical Society of America **123**, 3352 (2008).

[25] Y. Ladroit, X. Lurton, C. Sintès, J. Augustin, and R. Garello, *Definition and application of a quality estimator for multibeam echosounders,* in *2012 Oceans - Yeosu* (2012) pp. 1–7.

[26] C. Sintes, G. Llort-Pujol, and D. Guériot, *Coherent probabilistic error model for interferometric sidescan sonars,* IEEE Journal of Oceanic Engineering **35**, 412 (2010).

[27] A. C. Schimel, J. Beaudoin, I. M. Parnum, T. Le Bas, V. Schmidt, G. Keith, and D. Ierodiaconou, *Multibeam sonar backscatter data processing,* Marine Geophysical Research **39**, 121 (2018).

[28] T. C. Weber, G. Rice, and M. Smith, *Toward a standard line for use in multibeam echo sounder calibration,* Marine Geophysical Research **39**, 75 (2018).

[29] M. Roche, K. Degrendele, C. Vrignaud, S. Loyer, T. Le Bas, J.-M. Augustin, and X. Lurton, *Control of the repeatability of high frequency multibeam echosounder backscatter by using natural reference areas,* Marine Geophysical Research **39**, 89 (2018).

[30] F. G. Bass and I. M. Fuks, *Wave Scattering from Statistically Rough Surfaces: International Series in Natural Philosophy*, Vol. 93 (Elsevier, 2013).

[31] P. Beckmann and A. Spizzichino, *The scattering of electromagnetic waves from rough surfaces,* ah (1987).

[32] J. A. Ogilvy and H. M. Merklinger, *Theory of wave scattering from random rough surfaces,* (1991).

[33] A. G. Voronovich, *Wave scattering from rough surfaces,* (1994).

[34] A. Ishimaru, *Wave propagation and scattering in random media, 574 pages,* (1997).

[35] D. Jackson and M. Richardson, *High-frequency seafloor acoustics* (Springer Science & Business Media, 2007).

[36] J. H. Lambert, *Lamberts Photometrie: Photometria, sive De mensura et gradibus luminus, colorum et umbrae (1760)*, Vol. 6 (W. Engelmann, 1892).

[37] R. J. Urick, *Principles of underwater sound.* (1983).

[38] X. Lurton, *An introduction to underwater acoustics: principles and applications* (Springer Science & Business Media, 2002).

[39] D. Jackson, *Apl-uw high-frequency ocean environmental acoustic models handbook,* Applied Physics Laboratory, University of Washington, Technical Report **9407** (1994).

[40] M. Snellen, T. C. Gaida, L. Koop, E. Alevizos, and D. G. Simons, *Performance of multibeam echosounder backscatter-based classification for monitoring sediment distributions using multitemporal large-scale ocean data sets,* IEEE Journal of Oceanic Engineering **44**, 142 (2019).

3

Seafloor classification in a sand-wave environment on the Dutch Continental Shelf using multibeam echosounder backscatter data

But striking a sandbar with the sea on both sides,
they ran the vessel aground; and the bow stuck fast
and remained immovable,

Acts 27:41

No great discovery was ever made without a bold guess.

Isaac Newton

High resolution maps of sandy seafloors are valuable to understand seafloor dynamics, plan engineering projects, and create detailed benthic habitat maps. This chapter presents multibeam echosounder backscatter classification results of the Brown Bank area of the North Sea. We apply the Bayesian classification method in a megaripple and sand-wave area with significant slopes. Prior to the classification, corrections are implemented to account for the slopes. This includes corrections on the backscatter value and its corresponding incident angle. A trade-off in classification resolutions is found. A higher geo-acoustic resolution is obtained at the price of losing spatial resolution, however, the Bayesian classification method remains robust with respect to these trade-off decisions. The classification results are compared to grab-sample particle-size analysis and classified video footage. In non-distinctive sedimentary environments, the acoustic classes are not attributed to only the mean grain size of the grab samples but to the full spectrum of the grain sizes. Finally, we show the Bayesian classification results can be used

---

Parts of this chapter have been published in Geosciences **9** (3), 142 (2019) [1]

to characterize the sedimentary composition of megaripples. Coarser sediments were found in the troughs and on the crests, finer sediments on the stoss slopes and a mixture of sediments on the lee slopes.

3.1. Introduction

In recent years, increasing use has been made of multibeam echosounder (MBES) systems to characterize the seafloor by acoustic remote sensing. Use has been made of the bathymetric data derived from MBES systems (or single beam echo sounders (SBES)), correlated with grab samples to determine the variations in sediment over sand waves in the North Sea [2–5]. In addition to bathymetry data, MBES systems also provide backscatter (BS) data which can be utilized more directly to characterize seafloor sediments [6]. There are a variety of approaches in use for the classification of the seafloor using MBES backscatter data. These range from image-based segmentation approaches [7, 8], classification based on backscatter angular response curves [9, 10], as well as, principal component analysis of both bathymetry and backscatter data [11–13], among others.

We employ the Bayesian classification method, which was first developed in [14]. One of the key components of the method is that it considers the BS data per beam angle. This method can discriminate between relatively homogeneous sediments [15], can be used as a reliable tool for long-term environmental monitoring [13], and was previously applied to river beds where significant slopes needed to be accounted for [16].

The Brown Bank area of the North Sea (Figure 3.1a; data source: [17]) exhibits sand waves of various sizes, namely, sand banks (Figure 3.1b), sand waves (Figure 3.1c), and megaripples (Figure 3.1d) (see Section 3.2.1 for definitions). Although the main sediment is sand, there is a variation of muddy sediments mixed with gravel and shell fragments in the deep troughs and well sorted medium sand on the crest [18]. Also, infauna species diversity and abundance is much higher in the troughs than on the crest [18]. A high resolution classification map of seafloor sediments in a sand-wave area provides valuable information for both marine biologists, who study the spatial variability of seabed habitats and benthic communities, and modelers of seafloor dynamics.

The goal of this chapter is four-fold. We first apply the Bayesian classification method to a sand-wave area where there exist significant and rapidly changing slopes in small areas. The second goal is to investigate to what extent different acoustic classes can be distinguished. A comparison with grabs is carried out to investigate what sediment properties drive the acoustic discrimination in an area with relatively homogenous sediments. The third goal is to examine the trade-off between the geo-acoustic[1] versus spatial resolution of classification results. The final goal is to determine the patterns of sediments on different parts of the megaripple cycle using the acoustic classification results.

3.2. Study area, materials, and methods

3.2.1. Study Area

The Brown Bank is located 85 km off the coast of the Netherlands, in the middle between the UK and the Netherlands, due west of Egmond aan Zee (52°32′59.994″

---

[1] Geo-acoustic resolution: the scale at which different types of sediments can be resolved using a certain acoustic classification/characterization technique [15].

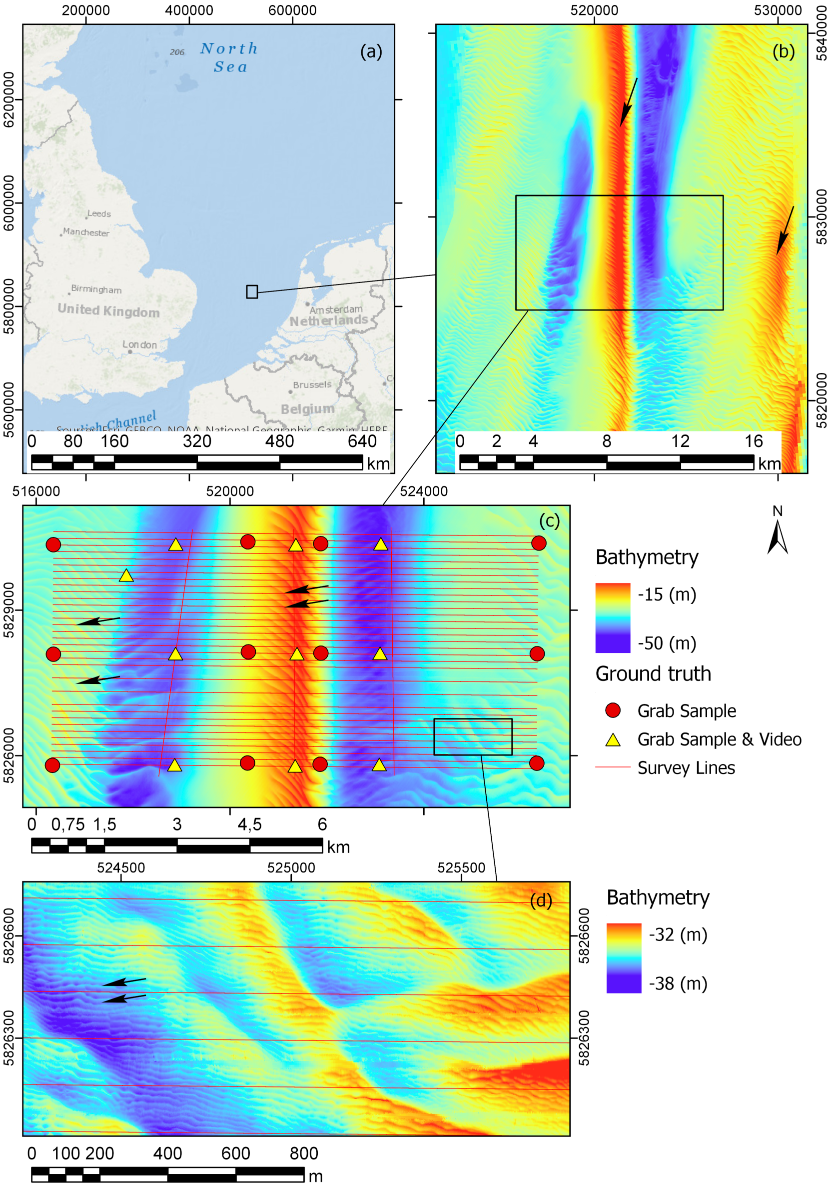

Figure 3.1: (**a**) Location of Brown Bank area in North Sea (data source: [17]); (**b**) Bathymetry of Brown Bank; arrows indicate sand banks; (**c**) Survey area; red circles and yellow triangles are ground truthing locations, survey lines are in red, and arrows point to sand-wave structures (spatial resolution 1 m × 1 m); (**d**) Megaripple bed forms, indicated by arrows (spatial resolution is 1 m × 1 m, all depths are given in meters (m)).

N, 3°18′36.400″ E; Figure 3.1). This area was visited in 2017 with the Royal Netherlands Institute for Sea Research (NIOZ) vessel, the Pelagia, from 27 October to November 3 (Cruise number/name: 64PE428disclose). Tidal currents in this area oscillate between a north eastern and south western flow direction with current flow rates exceeding 1 km/h. The average water current is in the north eastern direction [19]. The annual mean significant wave height is 2 m [20]. The main seabed substrate in this part of the North Sea is sand, with sand waves of various sizes clearly visible in the bathymetry. The dominant bathymetric features of the research area are sand banks (Figure 3.1b), which can be tens of meters high and have a length of 5–10 km [21]. In the study area there is mainly one sand bank, i.e., the most dominant one in the North Sea [21], which is called the Brown Bank. The Brown Bank runs from north to south, with a water depth on the top of the bank of ∼19 m, and a water depth in the troughs on either side being ∼45 m.

In addition to the sand banks, there are two other periodic bed forms that are defined in this chapter as sand waves (Figure 3.1c) and megaripples (Figure 3.1d) [22], respectively. Sand waves occur with a wavelength of around 200 m, with the occasional wavelength as short as 100 m and others as long as 300 m. In [23] it was found that sand waves migrate at a rate of several meters per year, and that the migration speed is strongly correlated with the sand-wave shape. Superimposed on the sand waves are megaripples [22], which have a wavelength of 15 m, where some wavelengths are as short as 10 m and others as long as 25 m. The megaripples move faster than the sand waves, in the scale of weeks [22, 24] or even hours [25]. The troughs of the Brown Bank consist of muddy sediments mixed with gravel and shell fragments and the crests contain well sorted medium sand [18].

3.2.2. Multibeam echosounder data

Multibeam echosounder settings

The acoustic survey was performed with a hull-mounted Kongsberg EM 302 multibeam echosounder (MBES). The EM 302 has a central frequency of 30 kHz and has 2° and 1° beam opening angles in the across and along track directions respectively. Four transmit sectors were used during the survey, each using a slightly different frequency of 26.5 kHz, 30.5 kHz, 33.5 kHz, and 28.5 kHz for sectors 1 to 4. The beam coverage of the 432 beams was set to equidistant (vs. equiangular). A swath opening angle of 130° was used, with port and starboard coverage both being 65°. The pulse length was 750 µs for the entire survey. The EM 302 has a sensitivity resolution of 0.1 dB. Bathymetry, backscatter, and water column data were recorded using Kongsberg's native seafloor information system (SIS) software. A Seapath global positioning system (GPS) and motion reference unit (MRU) provided position and motion correction information. GPS information was fed into the MBES processing, and was sufficient to eliminate the need to perform tide corrections. The MBES data were corrected for roll, heave, and yaw.

The data from the Pelagia were cleaned using the following steps. Firstly, the data was imported into the QPS Qimera software, and a spline filter was used to flag data points that were depth outliers. Subsequently, the cleaned data from Qimera

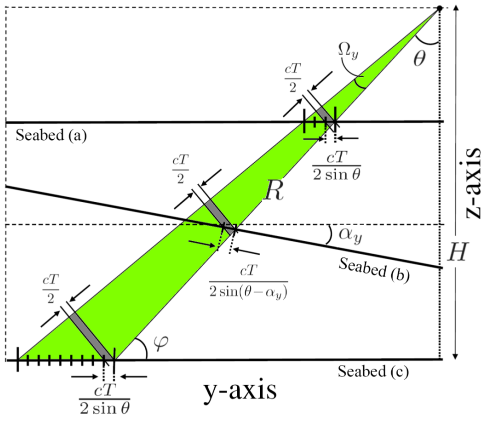

Figure 3.2: Across-track cross section (y-z) plane for the signal footprint of an oblique beam for three environments: shallow water (a), non-flat bottom (b), and deep water (c), (figure after [1] and [16] and similar to Figure 2.4).

were imported into Qinsy to convert them into an ASCII tabular format. Further processing was then carried out in Matlab. Aeration artifacts were filtered out if the average backscatter over 15 adjacent pings was more than 1.5 dB lower than the average backscatter over the nearest 700 pings.

Backscatter corrections for seafloor slopes

Because the survey area is dominated by sand waves and megaripples, with seafloor slopes as steep as 20 degrees, a slope-corrected grazing angle is needed. If not corrected, the significant slopes of the seafloor can in principle degrade the classification results. This is thus an essential pre-processing step because the Bayesian classification method uses the backscatter data at a specific grazing angle. We closely follow the pre-processing steps proposed by [16]. Figure 3.2 shows the across-track cross section of the signal footprint for three different environments, i.e., a shallow water, a deep water and a non-flat seafloor.

A three-step algorithm is employed to estimate and hence apply the corrections required due to the local slopes. The steps are as follows: (1) Estimating the along- and across-track seafloor slopes; (2) Correction of the true beam grazing angle; and (3) Correcting the backscatter data. These steps require the along- and across-track slopes in the time-varying coordinate system of the vessel. The details of the above steps are as follows.

Step 1 Estimation of local slopes

The least-squares method is employed to estimate the local slopes using the bathymetry data. The slopes are computed in the time-varying coordinate system of the vessel. The bathymetry data of a given MBES line was gridded to a grid size of 2 m × 2 m. Such a regular surface patch includes a few pings and beams around the central beam angle. For the discrete points within the surface patch, we then have $z_i = f(x_i, y_i), i = 1, ..., n$, n indicating the number of bathymetry data within the surface patch. Here x_i and y_i refer to the along and across-track coordinates in

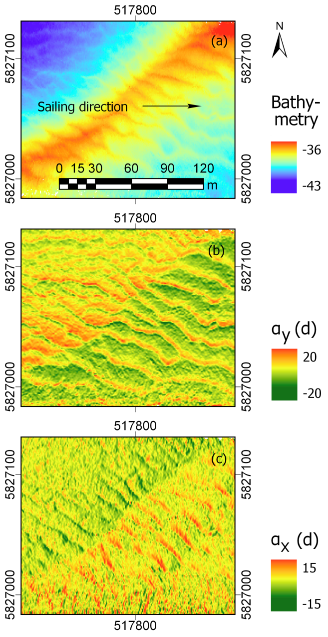

Figure 3.3: (**a**) Bathymetry data on a crest of a sand wave, (**b**) across track slopes α_y and (**c**) along track slopes α_x; depths are given in meters, slopes are in degrees (**d**)

relation to the vessel for point i. The surface patch is assumed to be a plane, with the form

$$f(x,y) = a_0 + a_x x + a_y y \tag{3.1}$$

consisting of three unknown coefficients a_0, a_x and a_y. The model of observation equations is of the form $z = Da$, where $z = [z_1, ..., z_n]^\top$ is the n-vector of observations containing the bathymetry data within the 2 m × 2 m surface patch, $a = [a_0\ a_x\ a_y]^\top$ is the vector of unknown parameters, and D is the $n \times 3$ design matrix for which its i^{th} row is $D_i = [1\ x_i\ y_i]$. Assuming the observations are independent and have identical variances, the least squares estimate of the parameters is $\hat{a} = (D^\top D)^{-1}$. A procedure called 'data snooping' can also be used to test for the presence of outliers in the bathymetry data [26, 27]. This will then leave out some outlying depth measurements when computing the local slopes.

Having estimated the parameters of the above surface patch $f(x,y)$, one can obtain the local slopes $f_x(x,y) = a_x$ and $f_y(x,y) = a_y$ where a_x and a_y are the ratios of the vertical to horizontal changes in the along and across-track directions respectively. Figure 3.3 shows one typical area in which the along and across-track slopes have been estimated. The signature of the megaripples is clearly visible from the computed slopes.

Step 2 Grazing angle correction

After estimating the local surface, the local slopes a_x and a_y of the plane are known (Equation (3.1)). The normal vector to the plane is the gradient of the surface, expressed as $\vec{\mathbf{n}} = [a_x \ a_y \ -1]^\top$. The nominal receiving-beam direction based on the flat surface in the z-y plane is provided as $\vec{\mathbf{m}} = [0 \ -\sin\theta \ \cos\theta]^\top$, where θ is the nominal incident angle. The angle between the two vectors $\vec{\mathbf{n}}$ and $\vec{\mathbf{m}}$ is the true incident angle, given as

$$\cos\theta_t = \frac{\sin\varphi + a_y\cos\varphi}{\sqrt{1 + a_x^2 + a_y^2}} \tag{3.2}$$

where $\varphi = \frac{\pi}{2} - \theta$ is the nominal grazing angle. Therefore, the nominal incident angle θ should be corrected to the true incident angle θ_t. This is an essential step because the classification method uses the backscatter data at a specific angle.

Step 3 Backscatter correction

The local slopes also affect the backscatter data. This is because the received backscatter refers to a flat signal footprint A'_f [16]. In the presence of local slopes, the signal footprint will change and hence the corresponding backscatter values need to be corrected for the actual ensonified area A_f using the along and across-track slope angles ($\alpha_x = \arctan(a_x)$ and $\alpha_y = \arctan(a_y)$) [16] (Figure 3.2). The correction C of the backscatter for the actual ensonified area, expressed in decibels (dB) is given as

$$C = 10\log\left(\frac{\sin(\theta - \alpha_y)\cos\alpha_x}{\sin\theta}\right). \tag{3.3}$$

The corrected data is then supplied to the Bayesian classification method.

Bayesian classification method

This section provides an overview of the essential steps to generate the acoustic classification maps from the backscatter (BS) data. The central limit theorem expresses that the BS follows a Gaussian distribution for one sediment type, if sufficient independent measurements are considered for determining the BS values. For a given frequency and angle, the backscatter strength depends on the seabed properties. If the survey area contains m sediment types, the BS histogram of the backscatter data for a specific incident angle is then represented by a linear combination of m Gaussian distributions as

$$f(y_j|\mathbf{x}) = \sum_{k=1}^{m} c_k \exp\left(-\frac{(y_j - \bar{y}_k)^2}{2\sigma_{y_k}^2}\right) \tag{3.4}$$

where y_j is the BS value at bin $(y_j, y_j + \Delta)$ of the BS histogram, with $j = 1, \ldots, M$ and M being the total number of bins. The bin size Δ is set by the sensitivity resolution of the MBES. The vector $\mathbf{x}$ contains the unknown parameters of the Gaussian distribution: $\mathbf{x} = (\bar{y}_1, \ldots, \bar{y}_m, \sigma_{y_1}, \ldots, \sigma_{y_m}, c_1, \ldots, c_m)$, where the triple ($\bar{y}_k$, σ_{y_k}, and c_k) indicates the mean, standard deviation and contribution of each Gaussian distribution for $k = 1, \ldots, m$. The curve fitting procedure is performed in an iterative manner for increasing m. The error in the fitting is tested by the χ^2 goodness of fit test, which is of the form

$$\chi^2 = \sum_{j=1}^{M} \frac{\left(n_j - f(y_j|\mathbf{x})\right)^2}{\sigma_j^2} \tag{3.5}$$

where n_j denotes the number of backscatter measurements per bin j in the BS histogram. For n_j a Poisson-distribution is postulated, indicating that the variance σ_j^2 is equal to n_j. The goodness of fit statistic has a chi-squared distribution with $\nu = M - 3m$ degrees of freedom. The goodness-of-fit criterion is then defined as the reduced chi-squared statistic, given by

$$\chi_\nu^2 = \frac{\chi^2}{\nu} \tag{3.6}$$

which has a value close to 1 for a good fit, indicating that the difference between modelled and measured histograms fall within the uncertainties of the BS data. The value of m for which no significant improvement on the reduced chi-squared statistic is obtained, or when it has a value close to 1, can be considered to be the optimal value of m based on the backscatter data.

The final classification step uses the Bayes decision rule. The above m Gaussians introduce m hypotheses as H_k, $k = 1, \ldots, m$ which correspond to the m seafloor sediment types. It is assumed that the hypotheses are equally likely and the Bayesian decision rule for multiple hypotheses then indicates to accept H_k if $\max_i \left\{f(y_j|H_i)\right\} = f(y_j|H_k)$. Given the observation y, the hypothesis that maximizes the likelihood $f(y|H)$ gets accepted. Thus, in principle, the intersections of the m Gaussians result in m non-overlapping acceptance regions A_k, corresponding to m acoustic classes (ACs).

Two levels of data averaging

To ensure that the central limit theorem is satisfied, namely the backscatter strength per angle and sediment type is Gaussian distributed, the backscatter values used should be the result of a sufficient number of independent measurements. The backscatter per beam is an average value, i.e., the result of N_s measurements, with N_s representing the number of signal footprints (or scatter pixels) within the beam footprint, see Figure 3.2. Sometimes the number of scatter pixels in a beam is small. Then the backscatter values are averaged over a certain number of neighboring beams and consecutive pings. This, though reducing the spatial resolution, ensures that each BS value is representative of a sufficient number of scatter pixels. In addition, a larger number of scatter pixels per backscatter strength value provides narrower Gaussian distributions per sediment type, i.e., increased geoacoustic resolution. For beams away from nadir, the ensonified area A_f is (much) smaller than the beam footprint. Therefore many scatter pixels fall within the footprint of the receiving beam. The number of scatter pixels N_s within a beam is a function of θ and α_y, and is given by

$$N_s(\theta,\alpha_y) = \frac{\left(\frac{R\Omega_y}{\cos(\theta-\alpha_y)}\right)}{\left(\frac{cT}{2\sin(\theta-\alpha_y)}\right)} \tag{3.7}$$

where Ω_y is the beam aperture in the across-track direction, c is the average water sound speed, T the length of the transmitted pulse, and $R = H/\cos\theta$, where H is the water depth. Equation (3.7) only holds for the beams sufficiently away from nadir. For beams closer to nadir the ensonified area is limited by the beam aperture and not the projected pulse duration. Thus, the nadir beams have only one scatter pixel.

To investigate the trade-off between the spatial and geo-acoustic resolution, two levels of data averaging were performed. In the first averaging scheme, no averaging was done as long as a data point was based on 20 or more scatter pixels, which was the case for the outer beams. If a data point had less than 20 scatter pixels, it was averaged with the geographically nearest neighbors until it was representative of at least 20 scatter pixels.

For the second scheme the data of a given MBES line was gridded to a grid size of 2 m × 2 m. The average backscatter and the average depth of all the points in a grid cell are used to form a single data point for that grid cell. It was further required that a grid cell contained at least 10 data points, otherwise the data within that grid cell was discarded. The advantage of this method is that the averaging of the backscatter increases, and hence it reduces noise in the classification results. The disadvantage is that it decreases the number of data points used in the classification, and thereby decreases the spatial resolution of the classification.

Megaripple partitioning

To investigate the distribution of sediments over megaripples, thirty two areas with a size of ~ 100 m × 100 m, where a clear megaripple pattern was present, were selected for further study. Using the orientation of the megaripples and the values of the absolute slopes, a direction specific slope was computed such that positive slopes would be on the stoss side (the side that receives dominant tidal current, also the less steep side) and the negative slopes would be on the lee side of the megaripple (Figure 3.4). The polarity of the computed slopes thus separated the area into the different sides of a megaripple. Further subareas were created by defining the crests and troughs of the megaripples. This was done by fitting a plane $Z = f(E,N) = a_0 + a_1E + a_2N$ to the bathymetric data using the least squares method. Here E and N refer to the easting and northing coordinates of the bathymetry data in a UTM (Universal Transverse Mercator) coordinate system. The points above the fitted plane are classified to be on the crest, and those below the plane, in the trough of the megaripple. The area was then binned based on the directional slope, ranging from −20 to 20 degrees with a bin size of 5 degrees (Figure 3.4). The bin centers are then at −17.5, −12.5,..., 17.5 degrees. The mean and mode occurrences of acoustic classes were calculated per bin and per trough and crest area for each of the 32 selected areas and used for determining sediment patterns over megaripples.

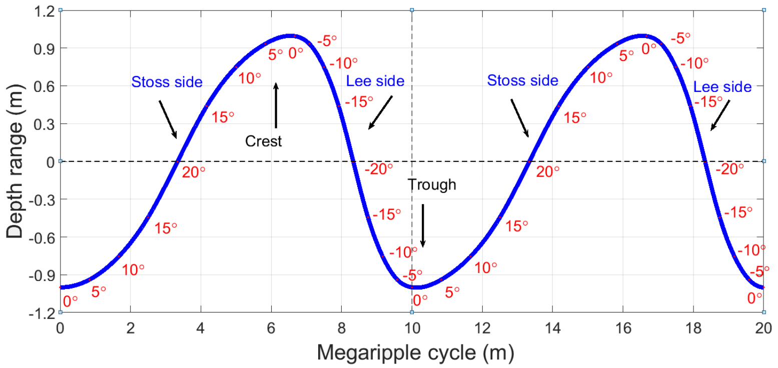

Figure 3.4: Schematic structure of a megaripple; wavelength is 10 m and depth variation is ~1 m. Also indicated are crest versus trough area and stoss versus lee sides. Slopes of the megaripple are presented with a bin size of 5 degrees.

3.2.3. Video data

Videos of the seabed were collected along 150 m transects at 10 stations (Figure 3.1c) with a towed video camera system. This system was inspired by the one used in [28]. The aluminum frame houses a remote controlled forward-facing video camera (Kongsberg OE14-522A-0009 Colour HD Pan), a downward facing DSRL camera (NIKON D750), eight lights (Fisheye FIX NEO 1000DX SW II LED), and two sets of lasers (Z-Bolt, SCUBA-II green) with a fixed separation distance. The video camera was set to view the seabed just in front of the frame. Moreover, the frame was equipped with multiple floats, resulting in a small positive buoyancy. Two drag chains underneath the frame cause for negative buoyancy. The varying length of the part of the drag chain which touches the seabed stabilizes the frame's height above the seabed. Three towing cables were attached to the frame at different points, which were combined after 6.5 m into one towing cable. A drop weight of 55 kg was attached to this merging point, which reduced the vertically oriented towing forces of the vessel on the frame. The video camera was connected to a computer on-board with a video data "umbilical cord", which was held in place separate from the towing cable. Using the live stream from the video camera, the length of the towing cable was adjusted to maintain seabed view during transects. During video operations, the vessel had a speed of ~0.1 m/s.

The collected video footage was analyzed and the superficial seabed type determined. The time of every observed change in seabed type was recorded. All recordings in which the seabed was not (clearly) visible, due to particle clouds or motion, or in which at least one of the lasers was not visible were defined as invalid. The position of the camera was estimated based on a time-match with the position of the vessel, which was saved by the vessel's logging system every 30 seconds. As the distance between the camera and vessel varies, depending on the prevailing depth and current, the exact position of the camera cannot be determined. However, because the camera was deployed on the starboard side of the vessel, with as little towing cable as possible, we assume the positioning error to be >10 m but

<100 m.

3.2.4. Grab-sample data

Twenty two grab sample locations were selected, with twenty one of these falling on a regular grid. That includes seven vertically oriented parallel lines each with three locations; in the eastern most border of the survey area, in the troughs on both sides, on the slopes on either side, and on the crest of the Brown Bank, and in the western most border of the survey area (Figure 3.1). At each sampling location three replicate samples were taken resulting in a total of 66 grab samples. The grab samples were acquired with a 30 cm Box Core. Subsamples were taken for particle size analysis (PSA). Between the time that the samples were gathered until they were processed in the lab, they were stored at −20° C. Prior to PSA the samples were freeze-dried. For the particle size analysis the contents of the sample were successively sieved over 4, 2, and 1 mm sieves and the weights of these fractions were measured. The particles that were larger than 2 mm were separated to determine the gravel fraction. The grain size distribution of the portion smaller than 1 mm was determined by means of laser diffraction with a Malvern Mastersizer 2000 (Malvern Instruments, Worcestershire, UK). The sieving and laser diffraction results were combined by scaling the results from the Malvern by the mass proportion of the sample that was smaller than 1 mm. This combined dataset was then used for further analysis.

The results of the grab sample sieving process were converted into the phi grain size units by using $\phi = -\log_2 d$, where d is the representative diameter of the grains in millimeters. Two measures are often used to describe the sediment grain size of a grab sample, that is, the median or the mean grain size. The median corresponds to the 50th percentile on the cumulative curve of which half the particles by weight are larger and half are smaller than the median. It is therefore of the form $M_z = \phi_{50}$. The mean is the average grain-size for which several formulas are used in the literature. The most commonly used formula is that given by [29]

$$M_z = \frac{\phi_{16} + \phi_{50} + \phi_{84}}{3} \tag{3.8}$$

where ϕ_{16}, ϕ_{50} and ϕ_{84} represent the size at the 16th, 50th, and 84th percentiles of the sample by weight. For the work presented here the mean grain size is used; but similar results are obtained using the median grain size.

In addition to the mean grain size, provided by Equation (3.8), statistics for sorting σ (Equation (3.9)), skewness s (Equation (3.10)), and kurtosis k (Equation (3.11)) of the grain size distribution were also calculated [29].

$$\sigma = \frac{\phi_{84} - \phi_{16}}{4} + \frac{\phi_{95} - \phi_5}{6.6} \tag{3.9}$$

$$s = \frac{\phi_{16} + \phi_{84} - 2\phi_{50}}{2(\phi_{84} - \phi_{16})} + \frac{\phi_5 + \phi_{95} - 2\phi_{50}}{2(\phi_{95} - \phi_5)} \tag{3.10}$$

$$k = \frac{\phi_{95} - \phi_5}{2.44(\phi_{75} - \phi_{25})} \tag{3.11}$$

These were used to create a feature matrix $Y = [M_z \ \sigma \ s \ k]$. Principal component analysis of this matrix, which is of size 66×4, was performed and the most informative principal components (PCs) were selected. These are then used to determine the correlation between the acoustic classification results and the full grain size spectrum of the grab samples.

Folk classification of the grab samples is also used. According to this classification method, sediments are given a descriptive label based on the proportions of Mud, Sand, and Gravel. Gravel particles are those larger than 2 mm, Sand those between 2 mm and 0.0625 mm, and Mud what is less than 0.0625 mm. A 0.01% boundary was used between a "no gravel" content and a "slightly gravelly" label.

3.3. Results and discussion

3.3.1. Acoustic Classification Results

The classification method of Section 3.2.2 is now applied to the backscatter (BS) data that was cleaned and pre-processed according to the description in Section 3.2.2. That is, the correct grazing angles are known and the backscatter data has been corrected for the change in the ensonified area induced by the seafloor slopes.

In the first step, the number of sea bottom types, distinguishable in the acoustic data, is determined. This is achieved by increasing the number of Gaussians to well describe the histogram of the BS values at a given grazing angle. The number of seafloor types, m, was found to be 4 (Figure 3.5). The beam angles used to create the histograms and to perform the Gaussian fitting procedure were the 30°, 28°, and 26° grazing angles, for both the port and starboard sides. The error bars in Figure 3.5 give the standard deviation of the χ^2_ν statistic, $\sqrt{2/\nu}$. Because the backscatter data from the EM 302 multibeam is recorded at a resolution of 0.1 dB the number of bins M per histogram tended to be well above 100. The variable ν gets larger with larger M and therefore the standard deviations of the χ^2_ν statistic, represented by the error bars in Figure 3.5, become small.

Figure 3.6 shows the BS histograms along with their best fit for the grazing angles 30°, 28°, and 26°. The intersecting points of the corresponding probability density functions (PDFs) are used to form the acceptance regions of the four classes. The percentages of the histogram at these reference angles that fall into a specific class were then recorded and used to divide, and thereby classify, the histograms for the grazing angles from 65° to 25°.

The acoustic classification results are presented in Figure 3.7. The broad scale

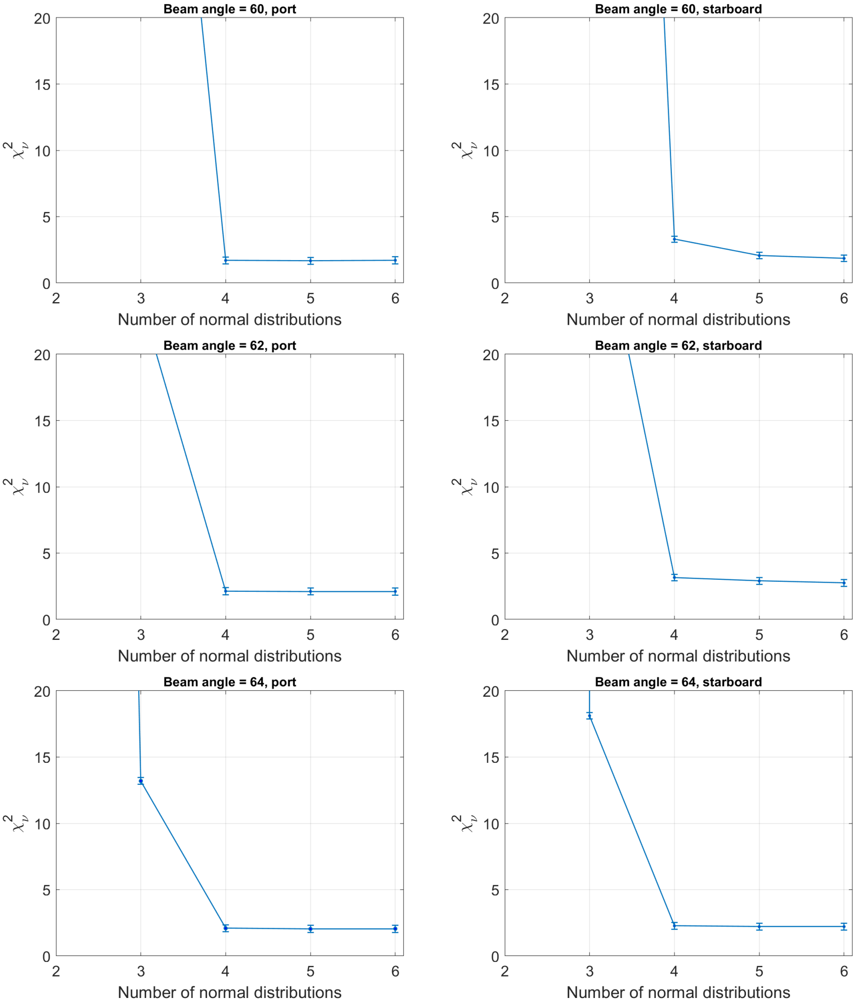

Figure 3.5: Reduced chi-square as a function of number m of Gaussians. Error bars, which were multiplied by a factor of 2 for distinction, indicate standard deviation of reduced chi-square test statistics.

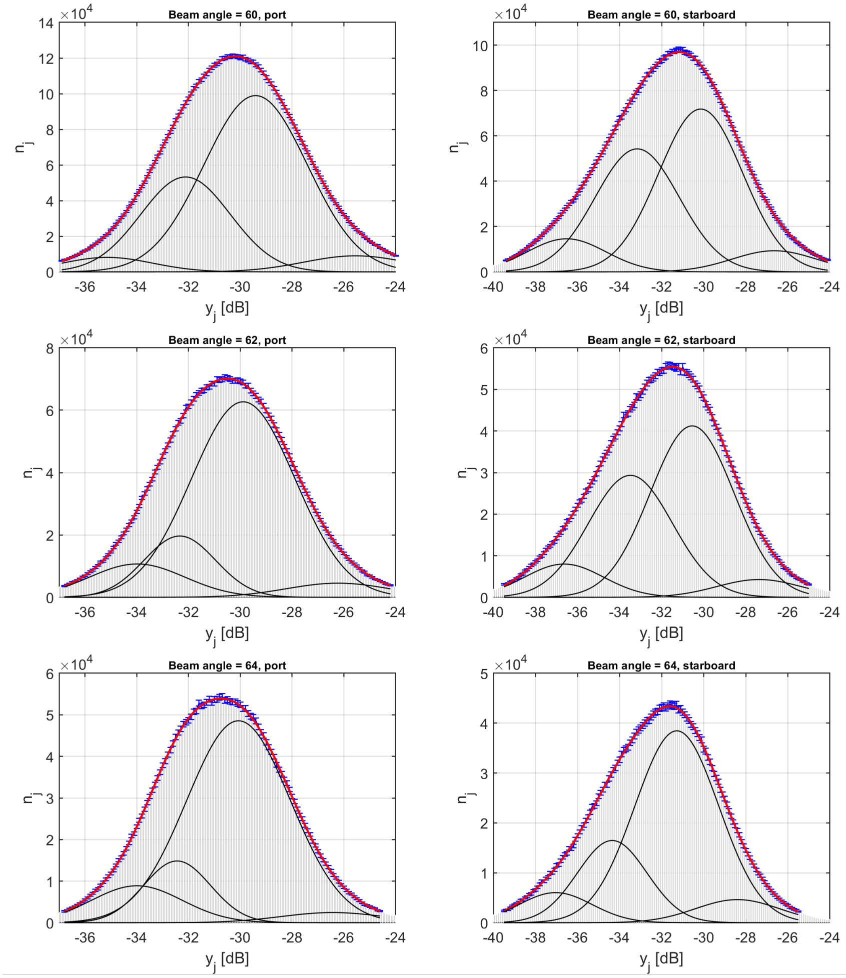

Figure 3.6: Measured histograms for grazing angles 30°, 28°, and 26° for both port and starboard sides, in gray; sum of $m = 4$ number of Gaussians, in red (see: Equation (3.4)), individual Gaussians are in black. Error bars (in blue) were multiplied by a factor of 3 for distinction.

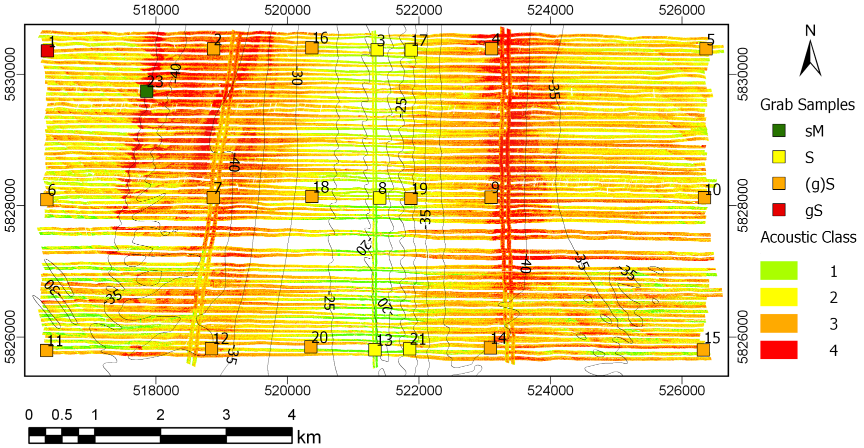

Figure 3.7: Acoustic classification map of Brown Bank obtained from backscatter data for beams between 25° and 65°. Also shown are grab Folk classes with their station numbers. Depth contours (solid black lines) are presented at 5 m intervals.

classification results fall into the following patterns. For water depths shallower than 25 m, on the crest of the Brown Bank, mainly acoustic classes 1 and 2 occur. Lower classes (1 and 2) generally correlate with smaller grain sizes [13]. In the troughs on either side of the Brown Bank, for water depths deeper than 35 m, the classes are higher, mainly classes 3 and 4. In the remainder of the area the classes tend to be a mixture of classes 2 and 3.

3.3.2. Ground truth data

In total there were 16,594 classified, and geo-referenced, seconds of valid video footage (video frames, Table 3.1). In all areas where video data was collected "Sand with a ripple structure" was found (Figure 3.8). The presence of shell fragments (Figure 3.8 b), smaller and larger stones (or Granules and Pebbles according to the Udden-Wentworth grain size classification scheme [30]) (Figure 3.8 c), and Sabellaria fragments (Figure 3.8 d) varied from one area to the next. Figure 3.9 represents the video classification results overlaid on the acoustic classes. The class "Sand with hardly any shell fragments" was only found on the crest of the Brown Bank, see Figure 3.9 (upper right). The remaining 3 classes were all found in the troughs on either side of the Brown Bank.

At Station 2 (Figure 3.9, upper left), alternating video classes of "sand with some shell fragments" and "sand with small stones and incidental larger stones" are seen. The alternation matches with the wavelength of the megaripples in this area. The acoustic classification also alternates on this spatial scale, between class 4, as the highest class, and class 3 or 2 for the lower classes. The video data at Station 8, containing "Sand with hardly any shell fragments", have mainly lower acoustic classes 1 and 2. At Stations 9 and 14 (lower parts of Figure 3.9) the video is classified as mostly "Sand with some shell fragments". However, some frames are

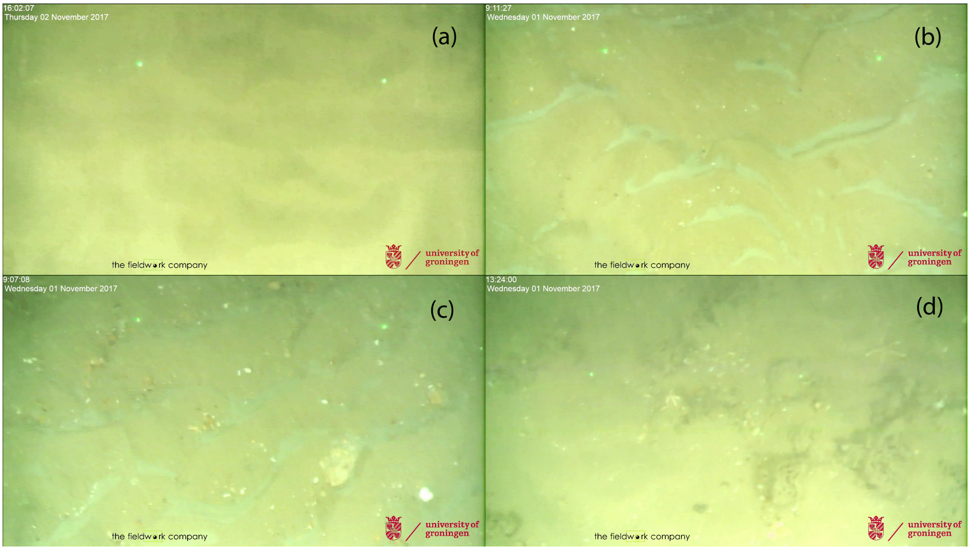

Figure 3.8: Sample video frames classified as (**a**) Sand with hardly any shell fragments, (**b**) Sand with some shell fragments, (**c**) Sand with small stones and incidental larger stones, and (**d**) Sand with Sabellaria fragments and incidental larger stones.

classified as also having either "Small stones and incidental larger stones" at Station 14, or "Sabellaria fragments and incidental larger stones" at Station 9. Their locations match with areas of higher acoustic classes (Figure 3.9).

To further investigate the relation between the video data and the acoustic classification results, the two datasets were geographically matched, and the occurrences of the acoustic and video classifications were counted. The mode of the acoustic class within a one-meter radius was used. If there were no acoustic classes within this radius then the video data point was discarded. The results are presented in Figure 3.10. In areas where the video recordings indicate "sand with no shell fragments" the occurrence of acoustic class 1 is dominant. There are no instances of acoustic class 4 in these areas. In areas where the video data indicate the presence of "sand with some shell fragments" the occurrence of acoustic classes 2 and 3 is highest at 32% and 49%. For "Sand with Sabellaria fragments and incidental larger stones" and "Sand with small stones and incidental larger stones" the distribution of acoustic class occurrences is very similar, with higher percentages for the higher acoustic classes. There were hardly instances of acoustic class 1 in these areas.

As for the grab samples, the majority have a mean grain size ranging from $M_z = 1.50\phi$ to $M_z = 1.75\phi$. The standard deviation of the mean grain sizes from the three samples taken at each station was at the same level as the size range of all the samples i.e., $\sigma_{M_z} = 0.25\phi$. There was one triple of grab samples (from Station 23) with a smaller mean grain size, $M_z = 4.04 \pm 1.18$, than the rest of the grab samples. The grab at this station was composed of very fine particles that

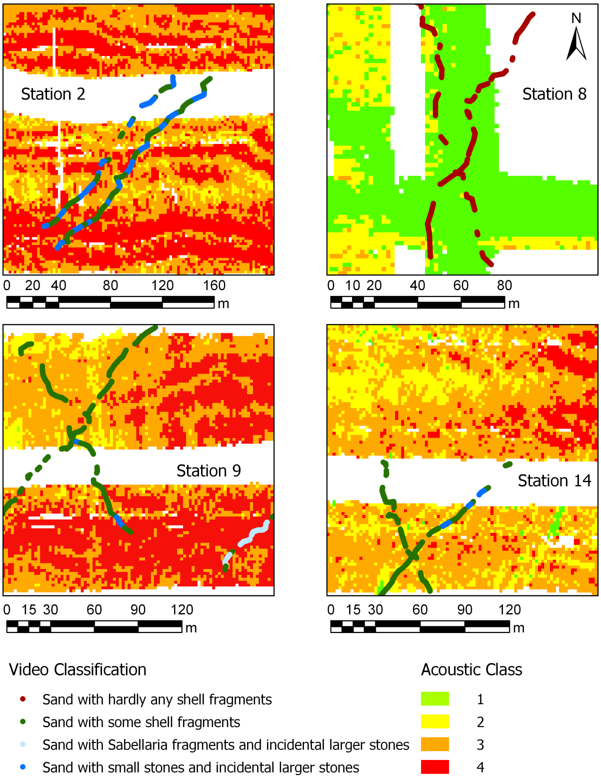

Figure 3.9: Video classification results at four stations. Per station, indicated location and class of video frame in colored dots and MBES classification results as background.

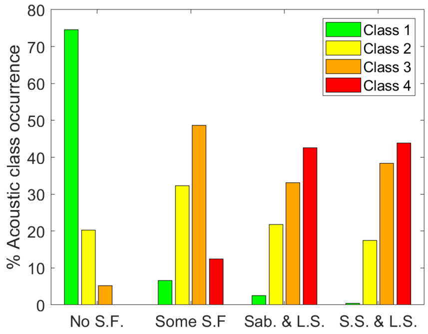

Figure 3.10: Percentages of occurrence of acoustic classes within one-meter radius of video data points, classified as follows: "Sand with hardly any shell fragments" (No S.F.), "Sand with some shell fragments" (Some S.F.), "Sand with Sabellaria fragments and incidental larger stones" (Sab. & L.S.), or "Sand with small stones and incidental larger stones" (S.S. & L.S.)

Table 3.1: Classification of video data with numbers and percentages of total frames per class

Classification	**Number of Frames**	**% of Total Frames**
Sand with hardly any shell fragments	4,495	27.1%
Sand with some shell fragments	8,651	52.1%
Sand with Sabellaria fragments and incidental larger stones	1,257	7.6%
Sand with small stones and incidental larger stones	2,191	13.2%
Total	16,594	100.0%

were compacted and stuck together. For most grab samples, clumps of particles that were stuck together could be brushed lightly in order for them to be sieved. The grab samples from Station 23, however, had to be crushed through the various sieve sizes with force. After doing this, the particle size analysis (PSA) indicated small grain sizes for this grab sample.

Often, backscatter-based acoustic classes are compared to the mean grain sizes to create sediment maps [12, 31, 32]. Figure 3.11a shows the results of such a comparison. It can be seen that the acoustic classification results are not correlated with mean grain size values. This observation not only holds when the mean grain size is compared with the acoustic classes, but also when the mean grain size of a grab sample is compared to its Folk classification (Figure 3.11b). Thus, a grab sample with different Folk class can have the same mean grain size.

When using Folk classes, the sediments “sandy mud” (sM), “sand” (S), “slightly gravelly sand” ((g)S), and “gravelly sand” (gS) were encountered. Out of the 22 grab sample positions there is 1 location that is classified as sM. There were 5, 15, and 1 locations that were classified as S, (g)S and gS, respectively. Thus, the dominant sediment types in the surveyed area is either sand or slightly gravelly sand, again indicating an almost non-distinctive sedimentary environment.

The number of matches between the Folk class and acoustic class at the grab sample locations shows a general trend of coarser sediments for higher acoustic classes (Figure 3.12). Sand corresponds mainly to acoustic classes 1 and 2. Slightly gravelly sand is matched dominantly with acoustic classes 2 and 3, and gravelly sand with acoustic class 3. However, the finest sediment sM correlates with acoustic class 4. This is likely due to the compactness of the sediment for this grab sample, as was described earlier. We may assume that (g)S of the grab samples corresponds to “Sand with some shell fragments” in the video data. This correspondence is also observed when comparing the grab samples and acoustic classes in Figure 3.12 with the video data and acoustic classes in Figure 3.10.

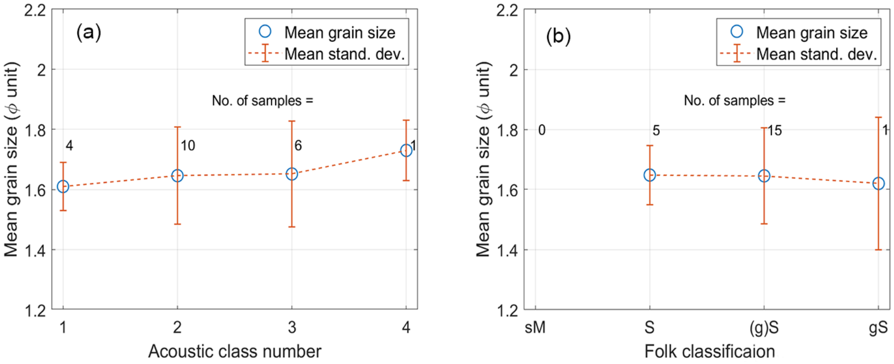

Figure 3.11: Averaged mean grain sizes and standard deviations versus acoustic class numbers (**a**) and Folk classification (**b**) for 21 of the grab samples with M_z from 1.50 to 1.74ϕ

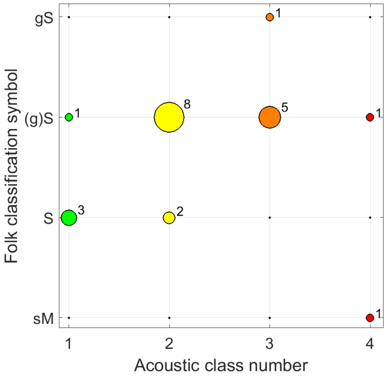

Figure 3.12: Correlation between sediment type and acoustic class at grab sample locations. Size of dots and numbers indicate number of matches between sediment types and acoustic classes.

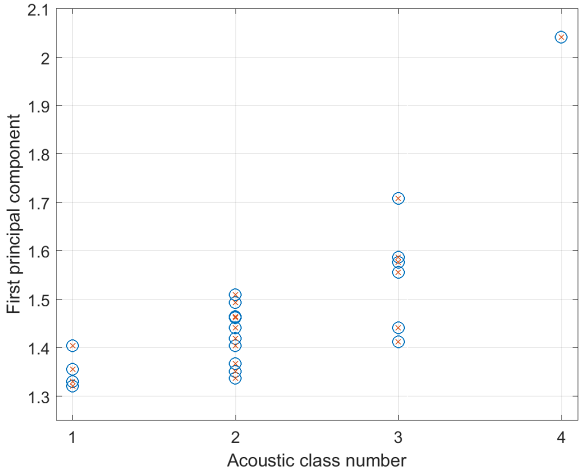

Figure 3.13: Acoustic class numbers versus first principal component obtained from grain size statistics given by [29]

3.3.3. Full spectrum of grain size distribution for classification

Based on the mean grain size of the grab samples, the survey area is very homogeneous. However, both the Folk classes of grab samples and the acoustic data indicate four sediment types. This indicates that the acoustic classes are to be attributed to the full spectrum of the grain size distribution and not just the mean grain size.

This is now investigated by using the variables M_z, σ, s, and k from Equations (3.8)–(3.11) and performing PCA on these as explained in Section 3.2.4. The first PC, representing 53% of the feature variabilities, is not far from being just the sign-corrected average of the above four features with the dominant contributions from σ, M_z and s. This PC is thus considered to be the most informative feature and hence will be used for comparison. Figure 3.13 shows this PC versus the acoustic classification results. A positive correlation is observed. This verifies that the full spectrum of the grain size distribution should be used when comparing grab samples with the acoustic classes and not just the mean grain size.

From the literature, it is expected that higher backscatter values would correspond to larger grain sizes. As indicated in Figure 3.11 there is no correlation with higher acoustic classes (which correspond to higher backscatter values) for larger mean grain sizes, because the mean grain size does not vary much over the grab samples. To check what influence larger grains have on backscatter values, the backscatter values from the beam angles ranging from 25 to 65 degrees were averaged over a few pings around each grab sample. These averaged backscatter values were compared to the percentage of the grab sample with a grain size greater than 0.5 mm (Figure 3.14). This showed that larger percentages of large grain sediments correspond to higher backscatter values (the linear correlation coefficient is 0.51). This finding is in agreement with the results presented by [33] who found

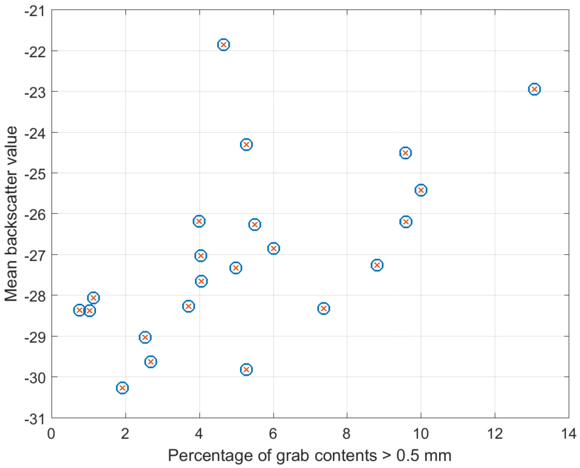

Figure 3.14: Mean backscatter value of angular response curve (excluded data around nadir) versus percentage of grab contents with grain sizes greater than 0.5 mm.

a positive correlation between backscatter levels and shell or gravel percentage of grab samples. It can therefore be concluded that the areas of high backscatter values (classes 3 and 4) correspond to slightly gravelly sand and lower backscatter values (classes 1 and 2) correspond to sand. Further investigation would be needed to quantify the influence of other factors affecting backscatter strength, such as surface roughness and volume scattering [34].

3.3.4. Geo-acoustic versus spatial resolution

The classification of sediments in the Brown Bank area brings to the forefront a dilemma of resolutions. On the one hand sediments may vary from crest to trough of some of the smallest sand waves, i.e., megaripples, which have a wavelength of a few tens of meters. It would be desirable to accurately classify sediments over these features at a high spatial resolution. On the other hand a high geo-acoustic resolution is needed to account for small changes in sediment composition from the crest to the trough of the megaripple. When applying the Bayesian classification method, the geo-acoustic resolution is increased when the data points are representative of a higher number of scatter pixels due to the standard deviation of the Gaussians being less. The theoretical standard deviation of the Gaussians is $\sigma_y = 5.57/\sqrt{N_s}$, where N_s is the number of scatter pixels [14]. An approach to increasing the number of scatter pixels per data point is to average the backscatter (BS) data over several beams in the across track direction, and several pings in the along track direction as employed by [16]. Performing such an averaging procedure has the added benefit of averaging out much of the ping to ping variability of backscatter data that is not dependent on the seafloor properties. While such averaging increases the geo-acoustic resolution, it directly decreases the spatial resolution of the classification.

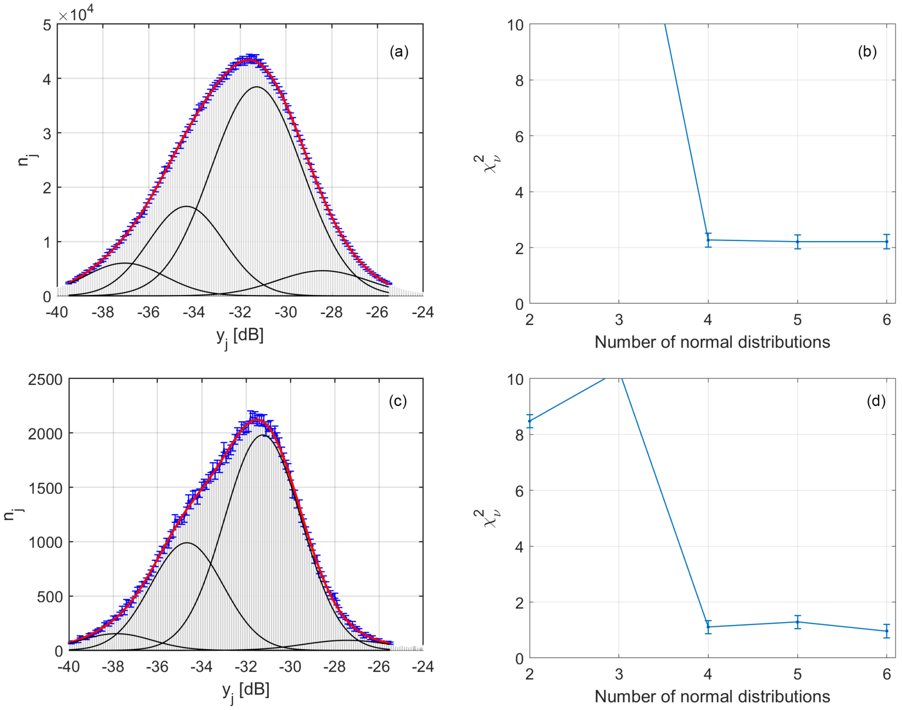

Figure 3.15: Comparison of Gaussian curve fitting to histogram of backscatter under two levels of averaging; limited averaging (top), heavier averaging (bottom); indicated in plots are Gaussian curve fitting (a and c), and chi-square test statistics (b and d). Fitting was done on grazing angle 26 degrees starboard.

For determining a good trade-off, the acoustic data were preprocessed with different levels of averaging (see Section 3.2.2). Figure 3.15 shows the fits of a Gaussian PDF to the BS histogram at the 26° starboard grazing angle for both approaches. A few observations are highlighted:

- The above averaging procedure can in principle reduce the noise of the backscatter data. This may, however, not decrease the standard deviation proportionally to the square root of the number of scatter pixels represented. This is because this rule is valid only for independent and identically distributed data. This cannot be the case for the backscatter data averaged over a small surface patch, because the variation and uncertainty in the BS data has independent and dependent components. The independent component is known as noise, which can be averaged out. This however does not hold for the dependent component, which is intrinsic to acoustic sediment properties and its heterogeneity. The fact that the two histograms in Figure 3.15 look similar also verifies the above reasoning; otherwise the second data set would have a significantly narrower histogram due to the averaging procedure.

- There is a trade-off between the spatial and geo-acoustic resolutions. While heavier averaging increases the geo-acoustic resolution of the classification, it directly decreases its spatial resolution. Narrower and relatively more separated Gaussians as well as chi-squared values closer to 1, obtained for the averaged data set (Figure 3.15 bottom subplots), indicate a better geo-acoustic resolution.

- The results obtained in Figure 3.15 show that the means and standard deviations of the Gaussians are characteristic of the acoustic properties of the sediment types. Given that the mean grain sizes of the grab samples suggested a homogeneous seabed in this survey area, it might be thought that if the parameters of the Gaussian were given a significant range within which they could vary, only one (or a few) Gaussians would be fitted to the entire histogram. The results show that this is not the case. For both datasets, the bounds for the standard deviation were set to a range of 0.5–2 dB but for neither dataset were the lower or upper bounds used after the curve fitting was implemented. This indicates that the Bayesian classification results are not significantly affected by the averaging procedure.

3.3.5. Classifying sediments over megaripples

Now we investigate to what extent MBES backscatter data can be used to classify the sediments over megaripples. This is of particular interest for detailed habitat mapping [35], engineering projects such as offshore wind farms or pipe laying [23], and for modelers of sand waves who study the morphology, hydrodynamics, and sand transport at the seafloor [2, 25]. In the previous sections it is found that higher acoustic classes correspond to sediments with a larger proportion of coarse sediments in this study area. These terms will thus be used interchangeably in the following paragraphs.

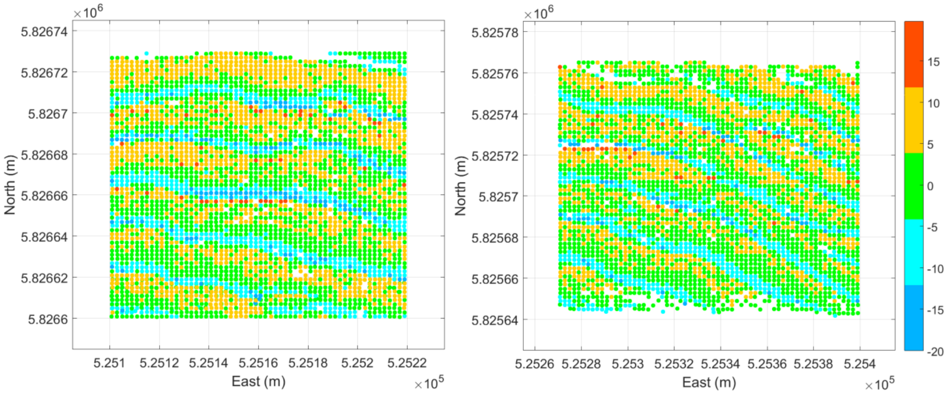

Figure 3.16: Maximum slopes (in degrees), representing megaripple structures, in two typical examples in Brown Bank area.

Thirty two areas where megaripples were present were selected and partitioned as described in Section 3.2.2; see Figure 3.16 for two examples. Figure 3.17 shows the histogram of the maximum slopes computed for the above-mentioned areas. For these areas the occurrences of acoustic classes per location on the megaripples were counted. These classification results for the slope bin centers are presented in Figure 3.18. At the lowest point of the stoss side of the trough, i.e., bin center (BC) $= 2.5^\circ$, the dominant AC is 3 (Figure 3.18, right). From the trough moving towards the crest, this gradually changes from higher classes to lower classes. The finest sediments (class 1) are found on the stoss side at BC $= 17.5^\circ$, for both the trough and crest areas. Continuing towards the crest, the sediments are classified as either class 2 or class 3. At the highest point on the lee side of the crest, BC $= -2.5^\circ$, the dominant acoustic class is again 3. This tends to become coarser when continuing down the crest towards the trough on the lee side. At BC $= -17.5^\circ$, the steepest point on the lee side, on the boundary between the crest and trough areas (specified by rectangles in Figure 3.18), a mixture of acoustic classes, ranging from fine to coarse (class 1 to 4), is observed. This is also clearly visible in the two typical areas (out of the 32) in Figure 3.19. An important characteristic of this part of the megaripples, is that the coarsest sediments appear only here (see also Figure 3.19, left). In the remaining parts of the trough, at BC$= -12.5^\circ$, -7.5°, and -2.5°, the sediments are again classified as coarse-grained.

To create a generalized acoustic class per position on the megaripple structure a weighted average of the dominant acoustic class was calculated for each slope bin, side of the megaripple, and trough or crest area. This can be considered a combining of the classification results presented in Figure 3.18. The result is shown in Figure 3.20. The alternating green and red line on the steepest part of the lee side slope indicates that the entire range of acoustic classes was found on this part of the megaripple. We hypothesize that this is a result of megaripple migration.

Megaripples migrate towards the lee side, known based on bathymetry comparisons with older data. This is also the average flow direction. We hypothesize

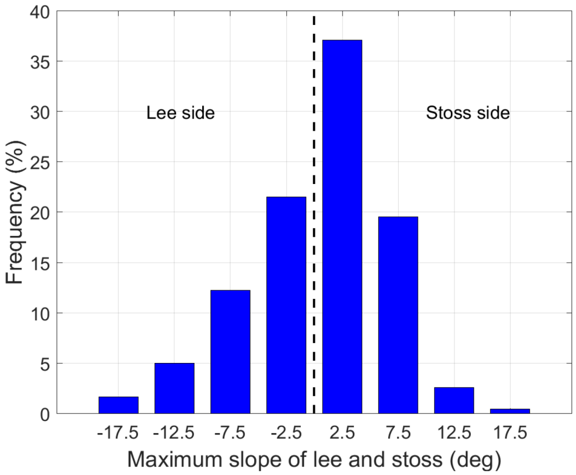

Figure 3.17: Histogram of maximum slopes computed in 32 typical areas with megaripple structures.

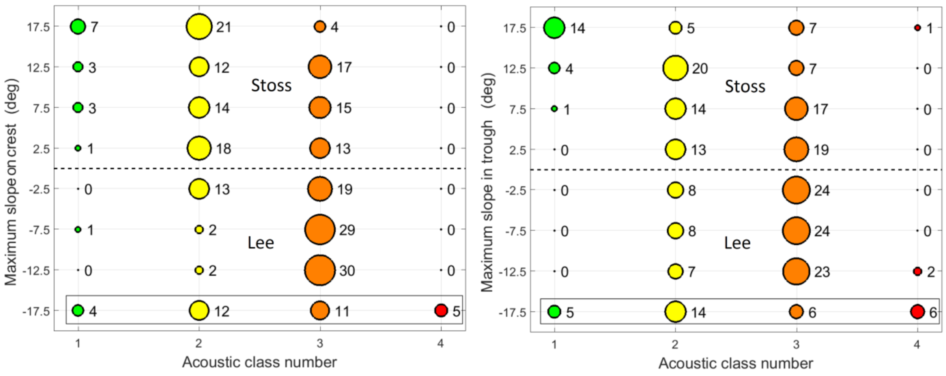

Figure 3.18: Acoustic classification results of 32 typical areas with megaripple structure given for bin centers ranging from –17.5 to 17.5 degrees; crest (**left**), trough (**right**).

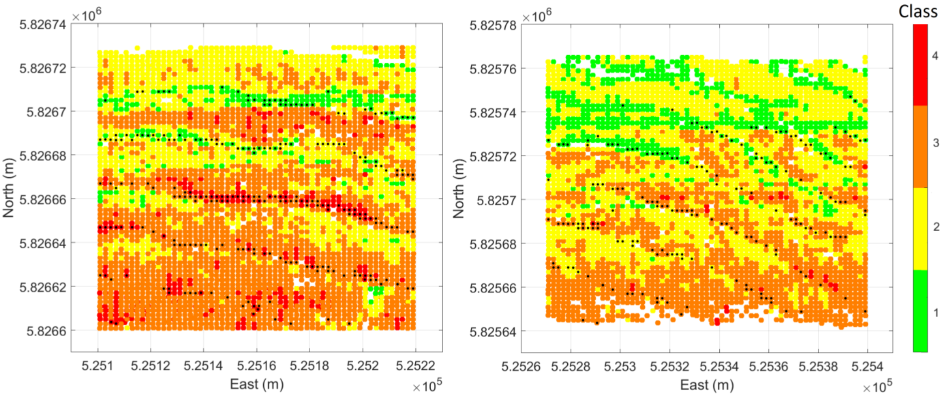

Figure 3.19: Acoustic classification results in two typical areas of Figure 3.16. Black dots indicate steep slopes of <−10° on the lee side of megaripples.

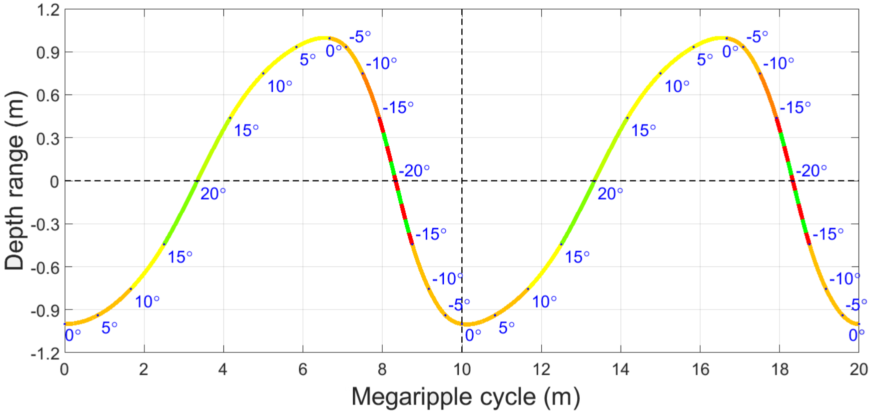

Figure 3.20: Schematic sedimentary composition of megaripple migrating to right; wavelength is 10 m and depth variation is ±1 m. Colors represent interpolated classes among class numbers 1, 2, 3, and 4, as in Figure 3.18; dashed green-red lines indicate all variants of sediment types (from fine to coarse).

that fine suspended sediments are deposited on the lee side of the megaripple. Then low acoustic classes are expected. At times of high tidal currents, the combination of the steep slope and a downward current causes an avalanche of the fine sediment deposition [25], leaving only the coarse sediments exposed. For that area high acoustic classes are then expected. This is why such a range of acoustic classes are encountered on the steepest leeward slopes of the megaripples.

3.4. Summary and conclusions

The Bayesian classification method was applied to MBES backscatter data gathered in the Brown Bank area of the North Sea. To obtain reliable classification results, steep and rapidly changing slopes over tens of meters had to be corrected for. Acoustic classification results were then compared with video and grab-sample data.

Based on the results of the sediment grain size analysis it was found that the seafloor sediments of the Brown Bank area are very homogeneous. The variance in the mean grain size over the entire area was at the level of the variance within the triplicate grab samples from individual sampling stations. However, Folk classification of grab samples, as well as the acoustic classification results were more discriminative. A further analysis showed that for areas like the Brown Bank, the full grain size distribution should be used when classifying the grab samples and when relating this ground truth data to the acoustic classification results. This should be taken into account for any future sediment studies in homogeneous sandy environments.

For acoustic classification of sediments in relatively homogeneous environments, especially over megaripple structures, high spatial and geoacoustic resolutions are required. There is, however, a trade-off in these resolutions. Therefore, depending on the aim of a classification application, either of these resolutions can be optimized for. It was found that the Bayesian classification method remains statistically sound when optimizing for the spatial resolution, as long as the number of scatter pixels used in the averaging satisfies the central limit theorem requirements. This is a pivotal result that underscores the validity of our acoustic classification results over megaripples.

The results revealed that there was a significant sorting of sediments over megaripples. Higher acoustic classes, and therefore coarser sediments, were found in the troughs and on the crests. Low acoustic classes were consistently found to be on the steepest part of the stoss side of a megaripple. On the, even steeper, lee side slope of the megaripple a mixture of all acoustic classes was found. These detailed results have a number of implications. First, for detailed habitat maps, the size of the megaripple and not that of the sand wave should define the resolution scale of the map. Next, researchers gathering ground truth data, such as grab samples and video data, should strive to geo-reference the point measured on the seafloor with an accuracy well below the wavelength of megaripples to avoid ambiguities in measurement. Finally, it confirms that the classification of backscatter data from MBES systems is a powerful method to further study and display the spatial distribution of sediments over megaripple bed forms. As such, it can provide valuable information for habitat mapping, engineering projects such as offshore wind farms or pipe laying, or to serve as field validation data for sand-wave modelers.

3.5. Acknowledgments

The authors would like to thank Rob Witbaard for being the chief scientist during the data gathering cruise and the crew of the NIOZ vessel the Pelagia for all of their assistance during the acquisition of the data. Karline Soetaert of NIOZ is acknowledged for her role in organizing the cruise, as well as Tom Ysebaert, who also coordinated the particle size analysis of the grab samples. Peter van Breugel was key in performing the particle size analysis in the NIOZ lab. Laura Govers and Han Olff of the University of Groningen are acknowledged for their valuable comments to earlier versions of this manuscript. We also thank Leendert Dorst and Daniëlle van Kuijk of the Hydrographic Service within the Royal Netherlands Navy for making full-coverage bathymetry data of the Brown Bank area available. We acknowledge the Gieskes-Strijbis Fonds for the financial support of the DISCLOSE project, within which this research took place.

References

[1] L. Koop, A. Amiri-Simkooei, K. J van der Reijden, S. O’Flynn, M. Snellen, and D. G Simons, *Seafloor classification in a sand wave environment on the Dutch continental shelf using multibeam echosounder backscatter data,* Geosciences **9**, 142 (2019).

[2] P. C. Roos, R. Wemmenhove, S. J. Hulscher, H. W. Hoeijmakers, and N. Kruyt, *Modeling the effect of nonuniform sediment on the dynamics of offshore tidal sandbanks,* Journal of Geophysical Research: Earth Surface **112** (2007).

[3] A. Stolk, *Variation of sedimentary structures and grainsize over sandwaves,* in *Marine Sandwave Dynamics, International Workshop, Université de Lille,* Vol. 1 (2000) pp. 23–24.

[4] C. Svenson, V. B. Ernstsen, C. Winter, A. Bartholomä, and D. Hebbeln, *Tide-driven sediment variations on a large compound dune in the jade tidal inlet channel, southeastern North Sea,* Journal of Coastal Research , 361 (2009).

[5] V. Van Lancker and P. Jacobs, *The dynamical behaviour of shallow-marine dunes.* in *Proceedings of the International Workshop on Marine Sandwave Dynamics / TRENTESAUX A., GARLAN T., (eds.). - Lille : University of Lille 1, 2000* (2000) pp. 213–220.

[6] C. J. Brown, S. J. Smith, P. Lawton, and J. T. Anderson, *Benthic habitat mapping: A review of progress towards improved understanding of the spatial ecology of the seafloor using acoustic techniques,* Estuarine, Coastal and Shelf Science **92**, 502 (2011).

[7] I. Marsh and C. Brown, *Neural network classification of multibeam backscatter and bathymetry data from Stanton Bank (Area IV),* Applied Acoustics **70**, 1269 (2009).

[8] G. Y. Ojeda, P. T. Gayes, R. F. Van Dolah, and W. C. Schwab, *Spatially quantitative seafloor habitat mapping: example from the northern South Carolina inner continental shelf,* Estuarine, Coastal and Shelf Science **59**, 399 (2004).

[9] J. H. Clarke, B. Danforth, and P. Valentine, *Areal seabed classification using backscatter angular response at 95 khz,* in *SACLANTCEN Conf on High Frequency Acoustics in Shallow Water* (1997) pp. 243–250.

[10] G. Lamarche, X. Lurton, A.-L. Verdier, and J.-M. Augustin, *Quantitative characterisation of seafloor substrate and bedforms using advanced processing of multibeam backscatter—application to Cook Strait, New Zealand,* Continental Shelf Research **31**, S93 (2011).

[11] C. J. Brown, B. J. Todd, V. E. Kostylev, and R. A. Pickrill, *Image-based classification of multibeam sonar backscatter data for objective surficial sediment mapping of georges bank, canada,* Continental Shelf Research **31**, S110 (2011).

[12] D. Eleftherakis, A. Amiri-Simkooei, M. Snellen, and D. G. Simons, *Improving riverbed sediment classification using backscatter and depth residual features of multi-beam echo-sounder systems,* The Journal of the Acoustical Society of America **131**, 3710 (2012).

[13] M. Snellen, T. C. Gaida, L. Koop, E. Alevizos, and D. G. Simons, *Performance of multibeam echosounder backscatter-based classification for monitoring sediment distributions using multitemporal large-scale ocean data sets,* IEEE Journal of Oceanic Engineering **44**, 142 (2019).

[14] D. G. Simons and M. Snellen, *A Bayesian approach to seafloor classification using multi-beam echo-sounder backscatter data,* Applied Acoustics **70**, 1258 (2009).

[15] E. Alevizos, M. Snellen, D. G. Simons, K. Siemes, and J. Greinert, *Acoustic discrimination of relatively homogeneous fine sediments using Bayesian classification on mbes data,* Marine Geology **370**, 31 (2015).

[16] A. Amiri-Simkooei, M. Snellen, and D. G. Simons, *Riverbed sediment classification using multi-beam echo-sounder backscatter data,* The Journal of the Acoustical Society of America **126**, 1724 (2009).

[17] Esri, *World topographic map,* Online (2012).

[18] T. A. van Dijk, J. A. van Dalfsen, V. Van Lancker, R. A. van Overmeeren, S. van Heteren, and P. J. Doornenbal, *Benthic habitat variations over tidal ridges, North Sea, the Netherlands,* in *Seafloor Geomorphology as Benthic Habitat* (Elsevier, 2012) pp. 241–249.

[19] P. Herman, O. Beauchard, and L. van Duren, *De staat van de noordzee,* (Noordzeedagen, 2014).

[20] *Msl swan annual mean significant wave height,* MetOcean Online database https:// app.metoceanview.com/ hindcast/.

[21] M. A. Knaapen, *Sandbank occurrence on the Dutch continental shelf in the North Sea,* Geo-marine letters **29**, 17 (2009).

[22] R. C. Lindenbergh, T. A. van Dijk, and P. J. Egberts, *Separating bedforms of different scales in echo sounding data,* in *Coastal Dynamics 2005: State of the Practice* (2006) pp. 1–14.

[23] M. Knaapen, *Sandwave migration predictor based on shape information,* Journal of Geophysical Research: Earth Surface **110** (2005).

[24] A. Nemeth, *Modelling offshore sand waves,* (2003).

[25] D. Idier, A. Ehrhold, and T. Garlan, *Morphodynamique d'une dune sous-marine du détroît du pas de calais,* Comptes rendus geoscience **334**, 1079 (2002).

[26] P. Teunissen, *Testing Theory: An Introduction*, Delft University of Technology (2000).

[27] P. Teunissen, D. Simons, and C. Tiberius, *Probability and observation theory,* Delft University Press (2004).

[28] E. V. Sheehan, T. F. Stevens, and M. J. Attrill, *A quantitative, non-destructive methodology for habitat characterisation and benthic monitoring at offshore renewable energy developments,* PLoS One **5**, e14461 (2010).

[29] R. L. Folk and W. C. Ward, *Brazos river bar [texas]; a study in the significance of grain size parameters,* Journal of Sedimentary Research **27**, 3 (1957).

[30] C. K. Wentworth, *A scale of grade and class terms for clastic sediments,* The journal of geology **30**, 377 (1922).

[31] J. Collier and C. Brown, *Correlation of sidescan backscatter with grain size distribution of surficial seabed sediments,* Marine Geology **214**, 431 (2005).

[32] D. Eleftherakis, M. Snellen, A. Amiri-Simkooei, D. G. Simons, and K. Siemes, *Observations regarding coarse sediment classification based on multi-beam echo-sounder's backscatter strength and depth residuals in Dutch rivers,* The Journal of the Acoustical Society of America **135**, 3305 (2014).

[33] D. G. Simons, M. Snellen, and M. A. Ainslie, *A multivariate correlation analysis of high-frequency bottom backscattering strength measurements with geotechnical parameters,* IEEE Journal of Oceanic Engineering **32**, 640 (2007).

[34] D. R. Jackson, A. M. Baird, J. J. Crisp, and P. A. Thomson, *High-frequency bottom backscatter measurements in shallow water,* The Journal of the Acoustical Society of America **80**, 1188 (1986).

[35] K. J. Van Der Reijden, L. Koop, S. O'flynn, S. Garcia, O. Bos, C. Van Sluis, D. J. Maaholm, P. M. Herman, D. G. Simons, and H. Olff, *Discovery of sabellaria spinulosa reefs in an intensively fished area of the Dutch continental shelf, North Sea,* Journal of Sea Research **144**, 85 (2019).

4

The measuring of cm scale sand ripples by their effect on multibeam echosounder backscatter data

> *Become a student of change.*
> *It is the only thing that will remain constant.*
>
> Anthony J. D'Angelo

> *Things don't have to change the world to be important.*
>
> Steve Jobs

Backscatter data from multibeam echosounders are commonly used to classify seafloor sediment composition. It has been shown that the survey azimuth affects backscatter when small organized seafloor structures, such as sand ripples, are present. These sand ripples are too small to be detected in the multibeam bathymetry. In this chapter we show that such azimuth effects are time dependent and are useful to examine the orientation of sand ripples in relation to the flow direction of the tide. To this end, multibeam echosounder data at four different frequencies were gathered from the area of the Brown Bank in the North Sea. The acoustic results were compared to video and tide-flow data for validation. The sand ripples affected the backscatter at all frequencies, but for the lowest frequencies the effect was spread over more beam angles. Using the acoustic data made it possible to deduce the orientations of the sand ripples over areas of multiple square kilometers. We found that the top centimeter(s) of the seafloor undergoes a complete transformation every six hours, as the orientation of the sand ripples changes with the changing tide. Our methodology allows for morphology change detection at larger scales and higher resolutions than previously achieved.

Parts of this chapter have been published in Geosciences **10** (12), 495 (2020) [1]

4.1. Introduction

The North Sea is one of the busiest seas of the world [2], with heavy shipping traffic [3] from major international ports such as Rotterdam, Antwerp, Hamburg, and Bremen. At its southernmost point, it connects to the English Channel at the Dover Strait, which is the busiest shipping lane in the world [4]. In addition to the shipping activity on the North Sea, it is also one of the most bottom-trawled continental shelves in the world [5]. Fishing activity is not distributed evenly, but focused on specific habitats [6]. Shallow nearshore areas are targeted by Beam-Sole fishers, non muddy flanks of large-scale elevations such as the Doggerbank by beam-Plaice fishers, and Otter-Mix fisheries are concentrated in deeper areas with low bed shear stress. To maintain a "Good Environmental Status" amidst multiple pressures, the European Marine Strategy Framework Directive (MSFD) requires European states to monitor their marine waters [7]. The use of acoustic methods is an important component of marine monitoring efforts [8].

Since their introduction in 1964 [9], multibeam echosounders (MBESs) have become a very useful tool for monitoring ocean environments. Initially, these systems were used mostly for measuring bathymetry. Recently, the use of the co-located and co-registered backscatter has been increasingly used for seafloor classification [10]. The desired backscatter level for seafloor classification is called backscatter strength, which is only dependent on the frequency of the transmitted signal, the angle of incidence of the acoustic wave relative to the seafloor [11], and the morphology and composition of the seafloor [12]. To get backscatter strength from backscatter, it needs to be corrected for the source level of the transmitter, transmission loss due to absorption and spreading, the angle-dependent sensitivity of the receiver array, the ensonified area of the seafloor, and any electronic gains applied by the sonar between signal reception and the logging of the backscatter data [12]. To characterize the composition of the seafloor accurately by the use of the backscatter strength, the effect of seafloor morphology on backscatter needs to be well understood.

The effect seafloor morphology has on backscatter can be particularly strong and unpredictable when the seafloor roughness is organized. For example, the presence of small sand ripples had an effect of up to 10 dB on angular-response curves (ARCs) according to [13]. In terms of sediment classification, an error of 10 dB could mean that Sandy Mud would be classified as slightly Gravelly Sand, a difference of three acoustic classes in [14]. It was further found that this effect was dependent on the survey azimuth. Lurton *et al.* [13] showed this with experimental data collected by sailing a compass rose survey pattern over the same area of the seafloor. ARCs were mainly affected between beam angles of 5° to 30°. The sand ripples were too small to be identifiable in the bathymetry measurements, despite their noticeable effect on the backscatter. It was further found in [15] that for sandy seafloors the backscatter values from a single area of seafloor changed significantly (>3 dB over the full angular range) during a 13 hour time series. This change was attributed to the changing of the seafloor roughness.

The fact that sand ripples affect the backscatter without them being detectable in the measured bathymetry increases the complexity of correcting for their effects. A means of detecting the presence of sand ripples might be by the use of high-frequency Side Scan Sonar (SSS) imagery. In [16], statistics-based modeling was used to simulate the effect that sand ripples would have on SSS imagery. The sand ripples in that study were larger, with a wavelength of ~0.5 m, than the ones encountered in this study. In [17], very high resolution (~0.04 m pixel size) SSS survey data were used to map stones and boulders for habitat mapping. In addition, sand ripples of a similar size were visible as those in this study. However, the orientation of the lee- and stoss-side slopes could not be discerned. This suggests that, in order for SSS data to be used to detect the sand ripple orientation, the survey would have to be carried out specifically for this purpose and with the SSS operating at its highest frequencies. As was the case for boulder detection in [17], it is likely that only a specific and small range of the SSS data would be usable for the detection of sand ripple orientations when operating with such settings. By using an interferometric synthetic aperture sonar [18], sufficient resolutions might be achievable.

Photographic and videographic methods can also be used to detect sand ripples [19, 20]. In [20], stereo-photo images of the seafloor were used to create digital terrain models (DTMs) of the sand ripples. Video methods can be used to create statistics on the presence and organization of sand ripples [19] or to confirm the presence and size of sand ripples [13].

The research site for this study is located in the Brown Bank area of the North Sea. Here, superimposed sand wave structures of multiple sizes are found [11]. The largest of these, tidal ridges, have a wavelength of ten(s of) kilometers and have been well studied [21–25]. Sand waves have a wavelength of (several) hundreds of meters and have also been extensively studied in the southern North Sea [11, 19, 23, 26, 27]. Megaripples have a scale of tens of meters [11, 26, 28]. All of the above bedforms are easily detectable in modern MBES bathymetry data. There is, however, an even smaller sand wave like structure, referred to as a sand ripple. These sand ripples have a wavelength of ten(s of) centimeters, and it will be examined to what extent their size, form, and orientation can be ascertained based on how they affect MBES backscatter.

The goal of this chapter is four-fold. Firstly, we link the patterns that deviate from normal (ARCs) to physical seafloor features that are smaller than the bathymetric resolution of the MBES. We then use the acoustics to predict the orientations of sand ripples at a given time. These two findings are confirmed with video data, and matched with the oscillation of the modeled tidal currents. Then, we examine the relationship between the acoustic results and the angles of the stoss- and lee-side ripple slopes. We furthermore examine how the backscatter of different frequencies is affected by these seafloor ripples. Finally, we convey to the reader that the effects that the bedforms, which are smaller than the MBES bathymetric resolution, have on the backscatter should be viewed not only as a source of ambiguity, but also as a powerful diagnostic tool.

4.2. Study area, materials, and methods

4.2.1. Study area

The The research data were collected in May of 2019 in the area of the Brown Bank. The Brown Bank is in Dutch territorial waters close to the border with the United Kingdom (Figure 4.1). This area was visited with the NIOZ research vessel the R/V Pelagia. Two multibeam echosounders (MBESs) were used. The NIOZ hopper camera was also deployed to collect video data of the seafloor [19, 29].

The main seafloor sediment at the Brown Bank is sand [11, 24]. In the troughs of the Brown Bank, there is a wider distribution of sediments than on the crest, but the mean grain size ($\phi \approx 1.65$ or $\mu m \approx 318$) is similar [11]. The average water flow in this area is in the northern direction [30], but the tidal flows oscillate between dominantly North and South in six-hour cycles. Based on modeled tide data, the maximum northward flow during the time of the survey was ~0.8 m/s and the maximum southward flow was ~0.7 m/s.

The seafloor in this area has repeating superimposed seafloor structures of at least four different sizes. The first two are tidal ridges and sand waves, both of which are visible in Figure 4.1a. The third are megaripples, which are detectable in MBES bathymetry data and the last are sand ripples. The wavelengths of these structures are ~10 km, ~200 m, ~15 m, and ~15 cm, respectively. The length L of the sand ripples can be determined from the video data. However, it is challenging to measure the height H of the sand ripples from the data collected during this cruise. From the literature, there are a few estimates of typical ripple heights. Ashley [31] gives two equations to calculate the height of sand ripples and sand waves as a function of their length L (Figure 4.2):

$$H_{avg} = 0.0677L^{0.8098} \tag{4.1}$$

$$H_{max} = 0.16L^{0.84} \tag{4.2}$$

Equation (4.1) is based on fitting a curve to the measurements of over a thousand flow-transverse bedforms [32]. Equation (4.2) gives an upper bound of H based on the same raw data. Baas [33] gives slightly different values in the form of a *vertical form index* (or *ripple index*), given as L/H, for which the most common value is 8–9. However, Baas [33] also indicates that it is not uncommon for ripples, of the type found in this study area, to have lower or higher values. The high values can be as high as 20. Figure 4.2 depicts a typical variation of height along a ripple, for several of these values of H. The length of the ripple in the schematic is based on the average observed length of sand ripples in the current study area. The ripple form is after [33]. The values of H used here are $H = H_{avg}$, $H = H_{max}$, $H = L/8$, and $H = L/20$. Regardless of the value of H used, these sand ripples will not be detectable in the available MBES bathymetry.

4.2.2. Multibeam echosounder data

For this survey, two MBESs were used, a Kongsberg EM 302 (Kongsberg Maritime, Kongsberg Gruppen ASA, Kongsberg, Norway) operating at 30 kHz, and a

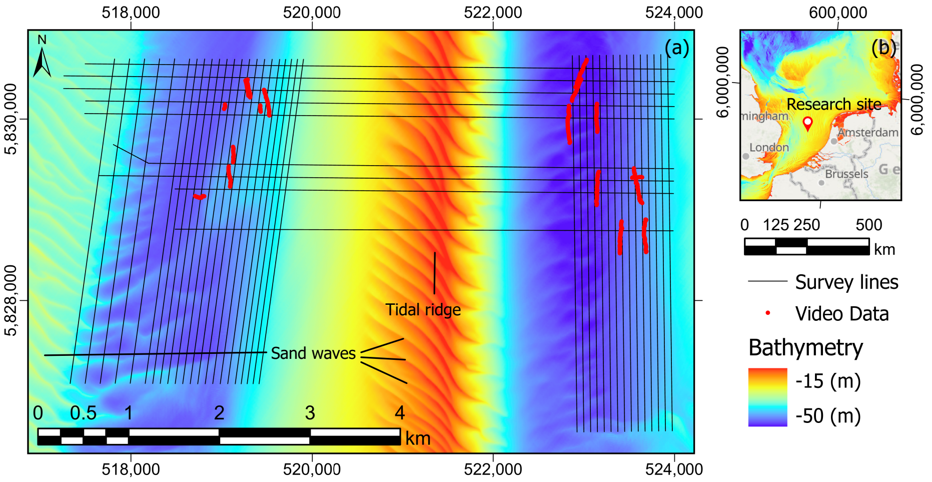

Figure 4.1: (**a**) Bathymetry of the Brown Bank area with black lines indicating survey lines, red lines indicating the location of video transects, and black arrows indicating the tidal ridge and superimposed sand waves; (**b**) geographic setting of the research site at the Brown Bank, color indicates bathymetry.

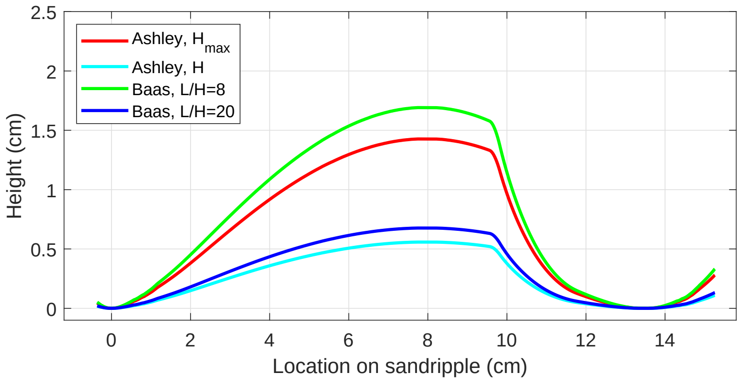

Figure 4.2: Schematic structure of the sandripples expected in the survey area deduced from the ripple wavelength.

multi-spectral R2Sonic 2026 MBES (R2Sonic, Austin, Texas) operating at 90, 200, and 450 kHz. While the EM 302 was hull mounted, the R2Sonic was mounted on a pole on the side of the vessel. Because the R2Sonic was installed only for this survey, a patch test was performed prior to survey operations, using a shipwreck as a ground object. Location data were acquired with a global positioning system (GPS). Ship motion data were supplied by a motion reference unit (MRU). The GPS and MRU were both Kongsberg Seapath 360 (Kongsberg Seatex, Kongsberg Gruppen ASA, Trondheim, Norway) units. Just prior to this survey, the MRU system was replaced on the R/V Pelagia. During the survey, an incorrect MRU offset was discovered. In the Seapath software, an MRU yaw offset of 35°, towards starboard, was registered when the actual yaw offset of the MRU was 0.57° towards port. The ray-tracing error thus induced was corrected in post-processing. For the EM 302 data, there were no lingering artifacts after the correction. The R2Sonic operated with roll compensation enabled some of the data collected before the MRU offset error was corrected, falling outside the beam angles of −60° and 60° after data correction in post-processing. This does not affect the reliability of the results.

The bathymetry and backscatter data from all EM 302 survey lines were logged in the Kongsberg *Seafloor Information System* (SIS). For this sonar, the SIS software is used for both data logging and sonar control. The R2Sonic, on the other hand, was operated and controlled using R2Sonic's *Sonic Control* software, while the data were logged in the Quality Positioning Services (QPS) (Quality Positioning Services, Zeist, The Netherlands) *Qinsy* software. Both bathymetry and backscatter data were collected. During survey operations, the R2Sonic was constantly monitored to ensure that the backscatter (BS) data would not be saturated (clipped). If there was a danger of saturated data, then the gain was adjusted as needed.

After the cruise, the data from both MBESs were cleaned. As a first step, all bathymetric outliers were removed using the QPS software *Qimera*. After this, *Qimera's* automated data-cleaning algorithm was applied. The spikes in the 90-kHz data that resulted from the occasional interference from the 30-kHz sonar were removed. In post-processing, it was noticed that there had been some movement in the side pole from one survey to the next. This introduced lever-arm errors in the R2Sonic data, mainly related to the yaw and minimally to the roll of the R2Sonic MBES. These offset artifacts were also corrected, using *Qimera* and data from overlapping survey lines. The side pole was also not perfectly stiff. When there was wobble in the pole, it was very evident in the bathymetric data, especially in the outer beams. Unlike the error introduced between surveys, which was correctable, the errors induced by pole wobble were not correctable and the data containing these errors were deleted.

The GPS data had a vertical accuracy of 0.5 m. Because the R2Sonic MBES system had better precision than 0.5 m, unpredictable vertical offsets in the bathymetry data were visible. Therefore, the vertical GPS data were disregarded, and the depth measured based on motion-corrected MBES data in conjunction with the known vessel draft. To overcome the effect of the tide, corrections were applied in *Qimera* from known tide data. After all corrections were applied, the EM 302 data were read into *Qinsy* and converted to ASCII format. The R2Sonic data were exported from *Qimera* in generic sensor format (gsf) from which the data were converted to the ASCII format. The ASCII data were read into MATLAB for further processing.

The backscatter (BS) data were corrected for spreading and frequency specific absorption. The corrections used ocean conditions as measured during the cruise based on conductivity, temperature, and pressure (CTD) data collected at the survey site. For the EM302 data, source levels applied during acquisition were used as outlined in [34]. For the R2Sonic data, receiver gain and source level corrections, which included directivity patterns, were applied in post-processing according to manufacturer recommendations. The backscatter values should be considered to be relative values, since absolute target strength calibrations were not performed. Ensonified area correction was performed for both sonars. For the R2Sonic data, an ensonified area correction was applied that took seafloor slopes into account, as was done in [35]. For the EM 302 data, it was necessary to first remove a flat seafloor based ensonified area correction that is implemented by Kongsberg. After this, slope and ensonified area corrections were applied as was done in [11, 36] by the use of a digital terrain model based on the bathymetry from the MBES data. As part of the verification process, data that are not corrected for slope, receiver gain, and source levels are used; it is indicated when this is done.

The ARCs were computed by binning the beam angles from lowest to highest. The number of bins was determined by the number of beams of the MBES. In the case of the EM 302, there were 432 beams and in the case of the R2Sonic, 256 beams. All of the backscatter data within each angle bin were averaged per survey line. The average backscatter value per bin was then plotted as a function of beam angle to form the ARC.

For part of the analysis, the backscatter values are not plotted as a function of angle relative to the transducer, but of angle relative to North (Figure 4.3). This was done in order to obtain ARCs independent of sailing direction. This was only done for lines that were sailed in the East and West directions.

4.2.3. Video data

Videos of the seabed were collected in the troughs on either side of the Brown Bank. Video transects ranged in length from ~50 m to ~425 m (Figure 4.1). The NIOZ hopper camera (Figure 4.4) that was used is described well in [19, 29]. It consists of a custom-made drop frame with a downward-facing HD video camera, an underwater light source (100 W), and two parallel green lasers (30 cm apart). The camera system was lowered to 0.5 m above the seabed, tethered to the vessel by a Kevlar cable with a glass fiber core allowing real-time video transfer. During camera survey operations a sailing speed of ~0.15 m/s was maintained.

In order to determine the orientation of the sand ripples on the seafloor from the video data, the following methodology was used. Based on the modeled tide data (Section 4.2.4), four video transects were selected, two of which were sailed when the tide was the strongest in the northern direction and two when the tide was the strongest towards the South. Of the selected transects, valid recordings were selected. Invalid recordings were those in which the seabed was not (clearly) visible, owing to particle clouds or motion, or in which at least one of the lasers was

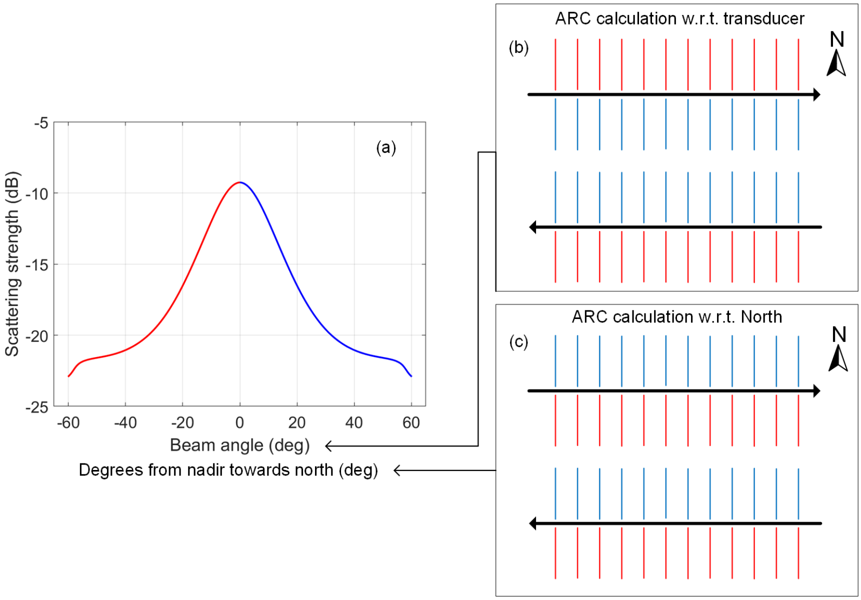

Figure 4.3: Schematic of the different ways the ARCs are calculated throughout the paper. (**a**) backscatter strength as a function of beam angle as calculated by the UW-APL model [37] at 90 kHz for medium sand. The different colors for the negative beam angles and positive beam angles indicate what data are used for the calculation of the ARCs as indicated in sub-figures (**b**,**c**); (**b**) a schematic of the data typically used to calculate ARCs. The black arrow indicates the sailing direction of the survey vessel per survey line. Red lines indicate port-side data, each line representing a ping. The red lines are the data that would be averaged per angle and represented by the red portion of the ARC in sub figure (**a**). Blue lines indicate starboard-side data and correspond to the blue portion of the ARC in sub figure (**a**); (**c**) similar to sub figure (**b**), but red lines are now always South of and blue lines are always North of the survey vessel.

Figure 4.4: Front view of the NIOZ hopper camera.

not visible. Of the valid recordings, seven images (still frames from the continuous video) were selected. Because the orientation of the video camera was not known, it was checked if the video camera was moving towards the top of the image, determined by observing the continuous video, or not. If not, the image was discarded and a replacement was found. For one of the transects, the video camera dominantly moved towards the bottom of the images. For this transect, images when the video camera moved towards the bottom of the image had to be used. (Care was taken to use the correct offset to calculate the sand ripple orientation also for this transect.) After the images were selected, the software *ImageJ* was used to draw seven lines on the images from crest to crest of the sand ripples. The statistics for line direction, relative to the image, and line length, relative to the laser points in the image were then computed in *ImageJ*. The mean compass direction of the sailed video transect was computed in *ArcGIS*. Both the calculations from *ImageJ* and from *ArcGIS* were then imported into the *R* software package and the ripple directions, relative to the images, were corrected using the mean transect direction, to have compass headings. The results indicated the compass direction that the lee-side of sand ripples were facing towards, in degrees from 0 to 360. In this case, 0° and 360° are both due North.

The lines in *ImageJ* used to calculate the orientation of the sand ripples were also used to determine the wave length L of the ripples. The known distance between the laser points in the image were used to scale the length of the lines drawn from crest to crest of the sand ripple to a physically meaningful length.

4.2.4. Tidal model data

The tide data for this research were generated by the Dutch Continental Shelf Model, version 6 (dcsm v6) [38]. This model is maintained by Rijkswaterstaat and Deltares. The tidal model covers the Dutch Continental Shelf (DCS) from 48° to 62.25° N and 12° W to 13° E. The resolution is 1/8 degrees in longitude and 1/12 (~6.5–9.3 km and 9.25 km respectively) degrees in latitude. The model uses a set of eleven tide stations at the boundaries and space and time varying wind and pressure fields as boundary conditions and input parameters, respectively. A timestep of 10 min is used. The output is validated by the use of nineteen tide stations on the DCS that are not a part of the tide stations used for boundary conditions. The root mean square error in the model output is less than 0.094 m.

Modeled tidal data were retrieved for the center of the survey area, at 52.6167° N and 3.3167° E. The tidal flow velocities were obtained in the North and East directions in meters per second. These data were read into and used in MatLab for comparison to ARC types and the analyzed video data.

4.3. Results

4.3.1. Angular response curves

The method of computing the ARCs that was described in Section 4.2.2 is applied to the backscatter data from both the EM 302 and the R2Sonic multibeam echosounders (Figure 4.5). Backscatter data are often affected by errors induced by the mechanical properties of the transducer [12]. A characteristic of such errors is that they occur in all survey lines collected by the given sonar as long as the settings are kept constant. This means that the errors are independent of survey azimuths and sediment type. In the ARCs computed for all the different frequencies, there are a few examples of this. The clearest of these is at ± 35° in the 450-kHz data (Figure 4.5d). This artifact is removed for the remainder of the figures by using the mean of the ARCs that were least affected by the sand ripples, interpolating the area of the dip with a line, and adding the difference between this line and the mean ARC to all the ARCs. The second most evident one is at 45° in the 30-kHz data (Figure 4.5a). For the purpose of the analysis of this paper, it was not necessary to remove this artifact.

The remaining artifacts are not present across all ARCs of a given frequency. The most noticeable case of this is in the ARCs of the 200-kHz data at ± 30° (Figure 4.5c). At these angles, there is an increased backscatter intensity for some survey lines but not for others. A further analysis reveals that the lines with increased backscatter intensity were surveyed either from East to West or from West to East. Unlike the typical behavior of an ARC (Figure 4.3) [37], these ARCs do not peak at nadir but slightly off nadir. In addition, between 30° and 35°, there is a bump in the ARC. When the backscatter data are corrected both with respect to the seafloor slope and ensonified area, this behavior is still present (Figure 4.6c,d). The main difference in the slope corrected data is that the peaks in question are more widely distributed across more beam angles.

From Figure 4.5c, there is not a clear pattern, but some of the curves do show

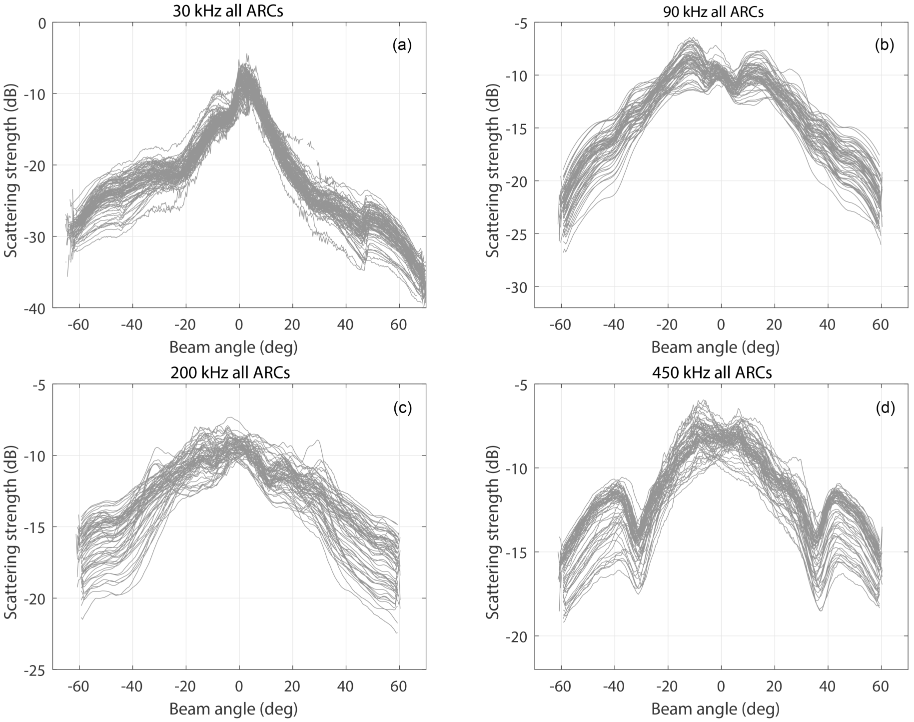

Figure 4.5: ARCs for frequencies 30, 90, 200, and 450-kHz in sub figures (**a**–**d**) respectively. Each curve is obtained as an average over a full survey line. The artifacts at ±35° of the 450-kHz data are removed from the remainder of the analysis.

a mirrored pattern. An obvious hypothesis is that these inconsistencies are due to sailing direction. Comparing only specific lines to each other as in Figure 5, this hypothesis would be supported. However, a further investigation showed that the ARC pattern is not consistent when only one sailing direction is considered (Figure 4.7). To investigate the cause for this change, ARCs were plotted not as a function of beam angle relative to the transducer but relative to North (Figures 4.3 and 4.8). This allowed the ARCs to be classified into four different types. ARCs which follow a typical pattern, with the peak at nadir (Figure 4.3), are referred to as Type 0. ARCs where the close-to-nadir peak is North of the transducer were called Type 1. When there were symmetrical peaks on either side of nadir, it was defined as Type 2 (only 1 survey line was Type 2). In addition, when the close-to-nadir peak was to the South, it was classified as Type 3. All of the East West lines that were sailed occurred between the evening of 21 May and the night of 23 May 2019. During the night of 21 May, acoustic surveys were carried out continuously for 11 h (ARC Type indicated by solid blue line in Figure 4.9). Then, on the morning and evening of 22 May, and the evening of May 23, single East–West survey lines were sailed (ARC type indicated by blue stars in Figure 4.9). It was found that the ARC type switched from Type 1 to Type 3 on six hour intervals (Figure 4.9). There was one instance of a Type 2 ARC on the evening of 22 May, at the point of a switch from Type 1 to Type 3. When the times of the switch in ARC Type are compared to the modeled tidal flow data, it is clear that the ARC Type change matches the switch in tidal flow direction (Figure 4.9).

4.3.2. Video results

Video transects were selected and analyzed as explained in Section 4.2.3. An example of a selected image from the video footage is seen in Figure 4.10. The seafloor in this image is lit from the above right. Visible in this image is a seafloor with sand ripples. The gentle stoss-side slopes of these ripples and the lee-side slopes that are at the angle of repose[1] (more on this in Section 4.4.1) are both clearly visible. Also shown are small yellow lines with a black dot in the middle. These are examples of the lines that were drawn in the software *ImageJ* to determine the ripple direction. The black arrow indicates the resulting estimate for the direction of these lines. Additionally, close to the top of the image are two greenish yellow dots. These are from the laser pointers of the camera system that are positioned exactly 30 cm apart.

The results from the analysis of the four video transects are shown in Table 4.1. This table gives the date and time, the mean orientation, mean length, and the associated standard deviations of the sand ripples for each transect. For the first two of these transects, $S1_4$ and $S2_3$, the lee side of the sand ripple was facing South. For the last two transects, $S2_8$ and $S2_4$, the lee side was facing North. The southward facing sand ripples had a length just over 10 cm. The North facing sand ripples had a length closer to 15 cm. The standard deviation for the orientation of the sand ripples was much greater in the first line than in the others, but still

---

[1] *Angle of repose* is the maximum slope, measured in degrees from the horizontal, at which loose solid material will remain in place without sliding.

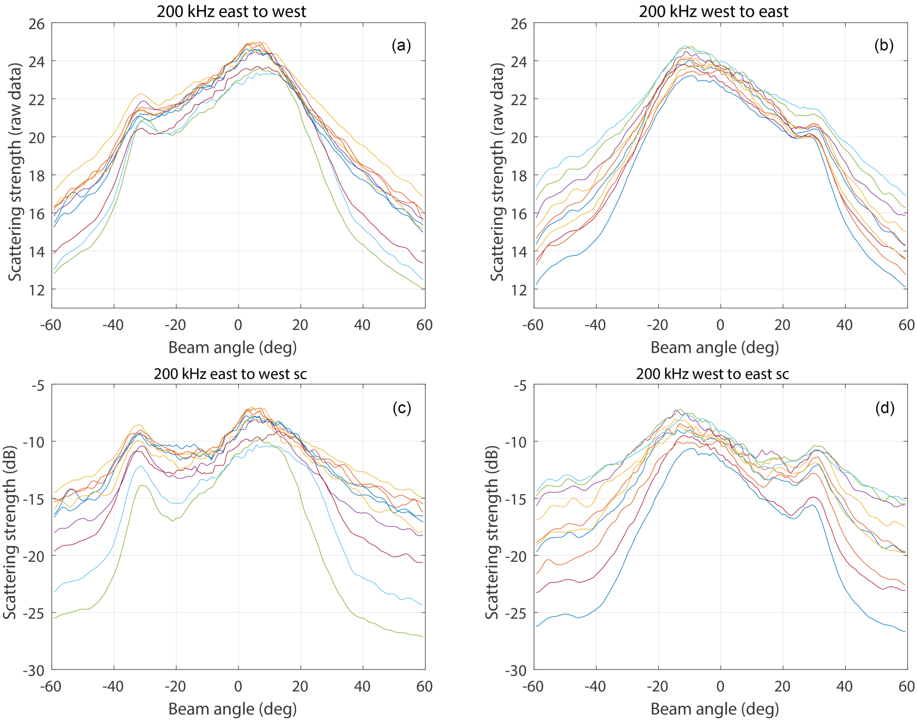

Figure 4.6: (**a**,**b**) ARCs using the "as logged" data for a survey line sailed from East to West and vice versa. Each ARC is computed based on data from consecutive subsets of pings of the survey line in question; (**c**,**d**) slope corrected ARCs from the same lines as in (**a**,**b**). All ARCs are of 200-kHz data.

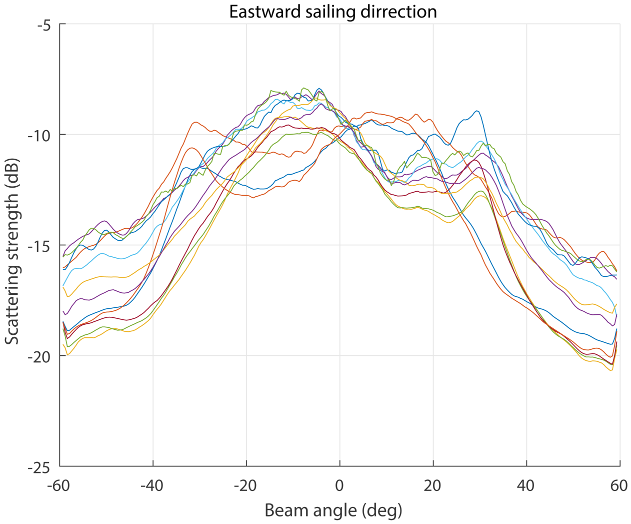

Figure 4.7: ARCs from 200-kHz data for all survey lines sailed from West to East.

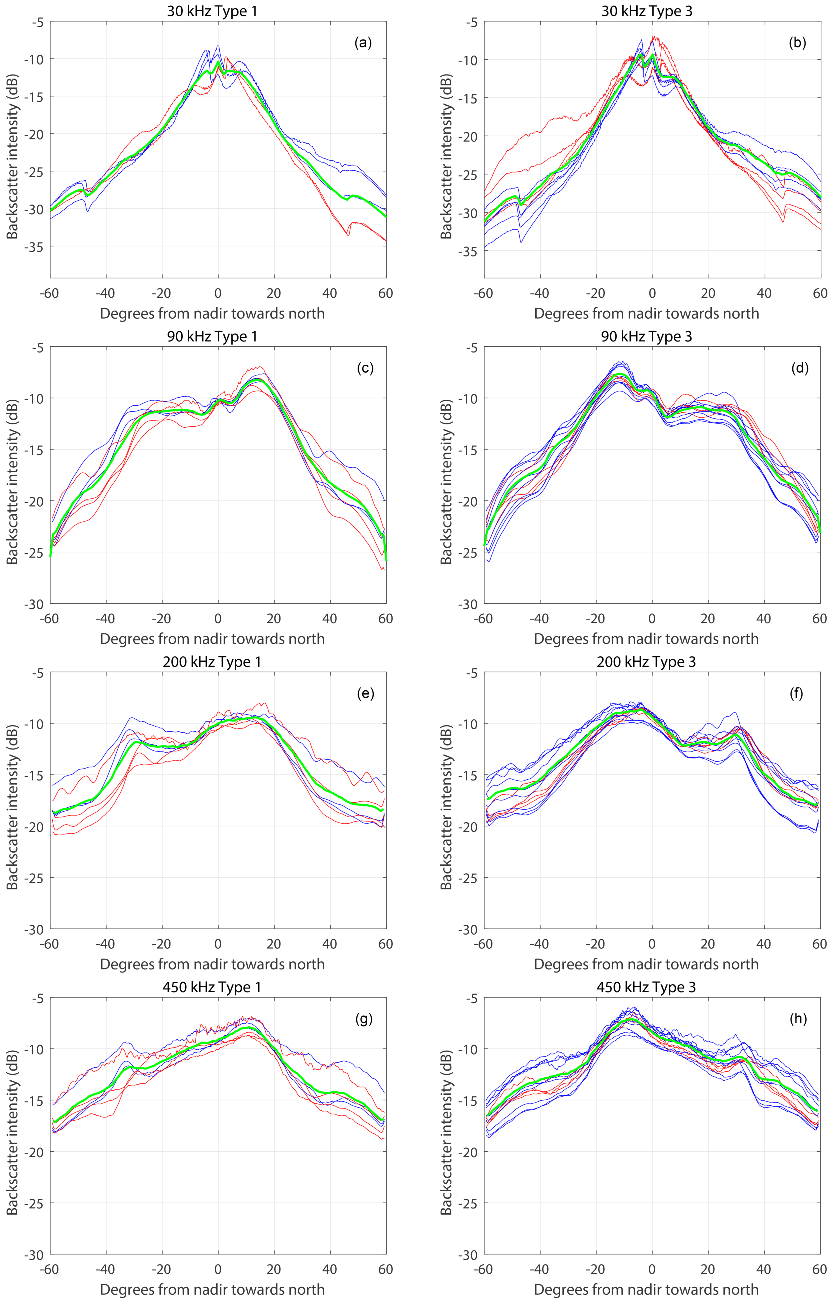

Figure 4.8: ARCs by frequency and type in sub figures. ARCs depicted in blue are from lines surveyed from East to West, and those depicted in red were sailed from West to East. The green curve is the average backscatter intensity of all ARCs.

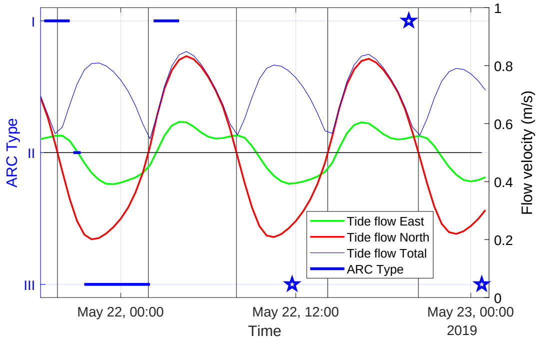

Figure 4.9: ARC type superimposed on modeled tidal flows. Bold blue lines indicate times when multiple consecutive lines were of a particular ARC type. The blue stars indicate times when single survey lines of the given type were available. Northward tide velocity is shown in red, eastward in green, and total tidal flow velocity is shown with narrow blue lines.

Table 4.1: Sand ripple statistics from video data.

Transect	Date, Time	Orient. (°)	Len. (cm)	SDO (°)	SDL (cm)
$S1_4$	19-5-19, 08:40	179.7	10.6	32.2	2.5
$S2_3$	20-5-19, 09:00	149.3	11.0	5.9	1.9
$S2_8$	20-5-19, 14:30	351.6	14.8	7.8	1.2
$S4_2$	22-5-19, 15:00	41.1	17.7	10.2	3.9

mainly facing South.

In order to compare this information to the modeled tidal flows, the data are superimposed on the tidal flow data in Figure 4.11. It is evident that the orientation of the sand ripple as derived from the camera measurements matches the tidal flow direction. This indicates that the ripple direction changes with the turning of the tide. In the East and West direction, for which the tidal flow is less strong, there is not a clear match with ripple directions (Figure 4.11).

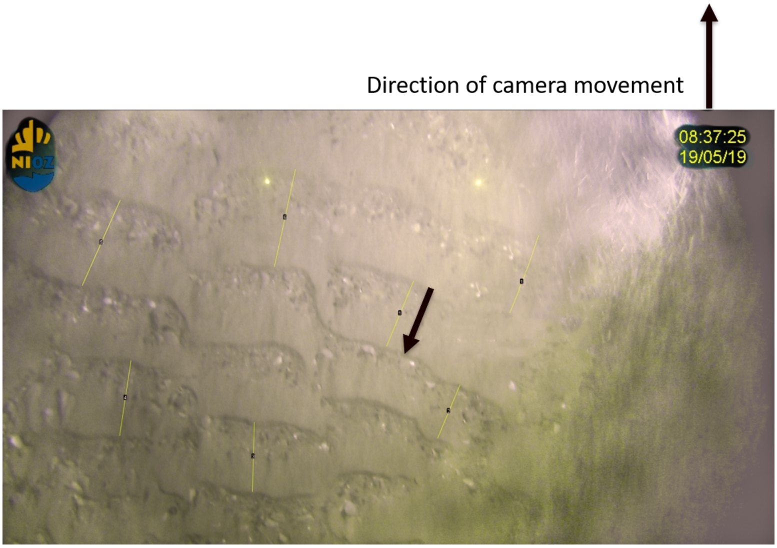

Figure 4.10: Still frame from video data. The black arrow in the frame indicates the direction of the sand ripples. The arrow above the frame indicates the direction of camera movement. Yellow lines were drawn in *ImageJ* to determine ripple orientation and length.

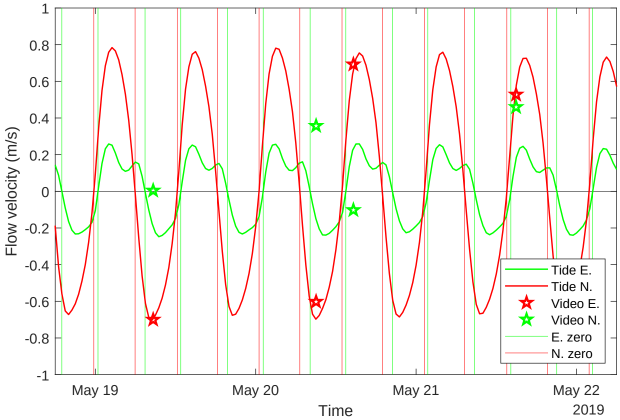

Figure 4.11: The East and North components of the sand ripples calculated from video ground-truth data given by the star symbols. The East and North components of the tidal flow data in thick lines, and the respective zero crossings in thin vertical lines.

4.4. Discussion

Thus far it has been shown that there are small sand ripples on the seafloor that are not detectable in MBES bathymetry data. They are, however, visible in the video data and they also cause a discernible pattern in the backscatter ARCs. These sand ripples change direction with the changing of the tidal flow. The backscatter behavior that was found, can be used as a diagnostic tool. On the one hand a diagnostic tool to characterize the properties of the sand ripples themselves. Even more powerfully, it is an acoustic tool with which the orientation of sand ripples can be measured over the scales of kilometers. For the situation considered, the results point to the complete reworking of the top layer of sediment in a matter of hours.

4.4.1. Quantifying sand ripple slopes based on backscatter data

Modeled results in [13] indicate that the angles at which the off-nadir peaks in the ARCs occur should match the angles of the slopes of the sand ripples. For the model, they used a "facet" model approach based on [39] for the close-to-nadir angles. For the oblique angles, Lambert's law was used to describe the backscatter coefficient angle dependence. They simulated two seafloor ripple types. The first was a strictly sawtooth shaped sand ripple and the second a rectified-sine-shaped sand ripple. For the rectified-sine-shaped sand ripples, the resulting modeled ARC had peaks at the beam angle γ_0, where γ_0 was also the maximum slope in the simulated sand ripples. For the simulated seafloor with a sawtooth-shaped sand ripple, the stoss and lee slopes had angles of γ_1 and γ_2, respectively. For this simulated seafloor, there were peaks in the modeled ARCs at beam angles γ_1 and γ_2. Based on this theory, it is expected that off-nadir peaks in the ARCs correspond to the slopes of the seafloor sand ripples.

The ARCs of Type 1 and Type 3 show peaks around ~10° and ~35° (Figure 4.12). These peaks are a little easier to recognize if the difference between the average ARC of either Type 1 or Type 3 and the average ARC of Type 0 is considered (Figure 4.13a,b Types 1 and 3, respectively). Based on the location of these peaks, sawtooth-shaped sand ripples with lee-side slopes of ~35° and stoss slopes of ~10° would be expected. Sawtooth-shaped sand ripples do indeed characterize the corresponding ground-truth video data. Furthermore, during the analysis of the video data, it was noticed that there were active avalanches on the lee side of the sand ripples. This video evidence implies that the lee-side slopes of the sand ripples are near the angle of repose. According to [40], this angle, for "water filled" sand, is between 15° and 30° and, for dry sand, it is 34°. The peaks in the ARCs (Figure 4.13) would indicate that the lee-side slopes are at ~35°. These values are somewhat higher than the "water filled" values given in [40] and up to values listed for dry sand. When the angle of repose was studied for non-uniform sediment in [41], the "in water" angle of repose for the same sediment mixtures was found to be higher than that of the "in air" angles. They listed angles of 38.29° (in air) to 40.96° (in water). These angles are higher than the ARCs would suggest, but this could be explained by the fact that [41] considered larger grain sizes than those found in the current study area. The match between the implied lee-side slopes indicated by the ARCs and the theoretical and experimental angles of repose from

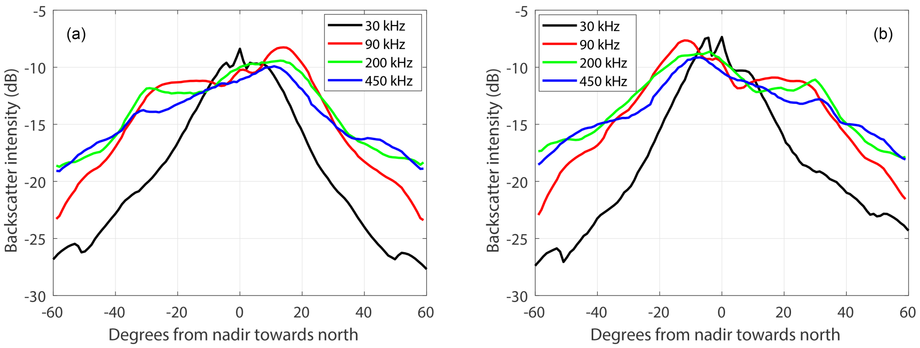

Figure 4.12: Average ARC per type superimposed for each frequency. ARCs were vertically shifted to be of similar intensity around nadir. (**a**) ARCs of Type 1; (**b**) ARCs of Type 3.

the literature supports the use of these acoustic methods to indicate the angles of sand ripples. It should be noted that this angle measurement does not come from the bathymetric measurements, but from the behavior of the backscatter at specific beam angles.

For the lee side of the sand ripple, we get an accurate independent estimate of the steepness of the slope, owing to the fact that avalanching occurs at a known angle of repose. For the stoss-side slopes, it is much harder to obtain independent information of the angles. From the video data, it is not possible to measure these angles. Furthermore, the surfaces of the box cores that were taken in this survey were deemed insufficient in size for accurate measurements. In addition, it is not known whether the surfaces remained intact in the grab taking process. As such, from the data in this research, we cannot conclusively say what the angles of the stoss sides of the sand ripples are. However, because of what we know from the lee slopes and the accuracy of their measurement, it is believed that the close-to-nadir peak in the ARCs is an accurate measure of the stoss slopes of the sand ripples. These slopes, thus, would be at ~10° (Figure 4.13).

To further investigate if these results are reasonably accurate, a strictly sawtooth-shaped sand ripple, with the angles derived from the ARCs for the stoss- and lee-side slopes, is superimposed on the schematic of typical sand ripples of the size found in the study area. This comparison depicts that the derived slopes match well with the expected slopes as reported in the literature (Figure 4.14). Using the stoss- and lee-side angles as 10° and 35° would give a *vertical form index* of 7.5 when assuming a strictly saw-tooth shape. Given that the sand ripples are unlikely to have a perfect sawtooth form, a larger *vertical form index* is expected, which would match well with the values given by [33]. We thus conclude that both the stoss- and lee-side angles of 10° and 35° are reasonable values for the sand ripples in the study area.

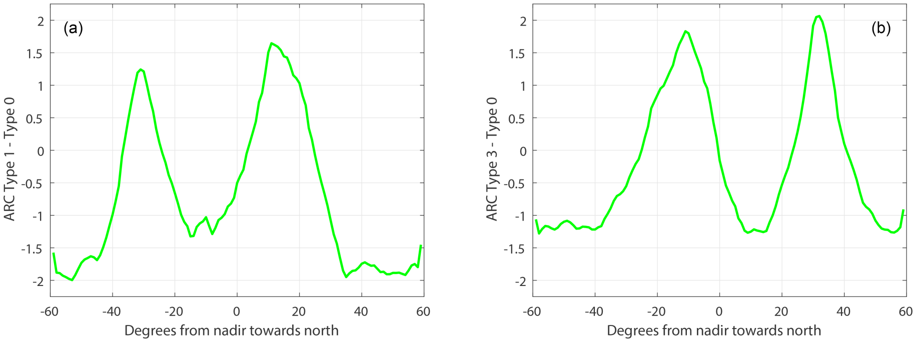

Figure 4.13: **a**) the difference between the average ARC of Type 1 and Type 0 as a function of angle away from nadir; (**b**) the difference between the average ARC of Type 3 and Type 0 as a function of angle away from nadir. Positive angles are towards North. The curves are based on the 200-kHz data.

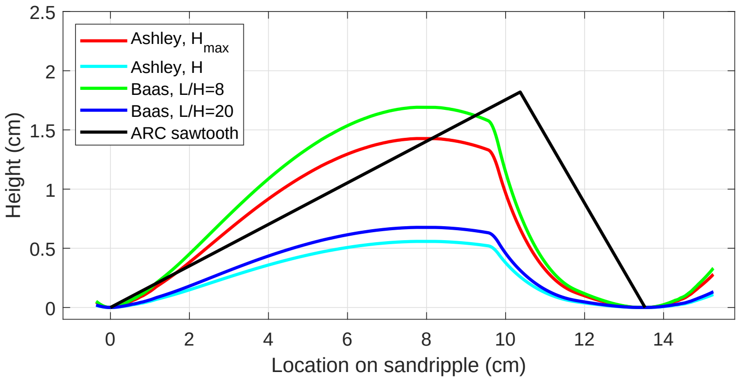

Figure 4.14: Schematic sand ripples from Figure 4.2, compared with a hypothetical, strictly sawtooth-shaped sand ripple with angles deduced from ARC indications.

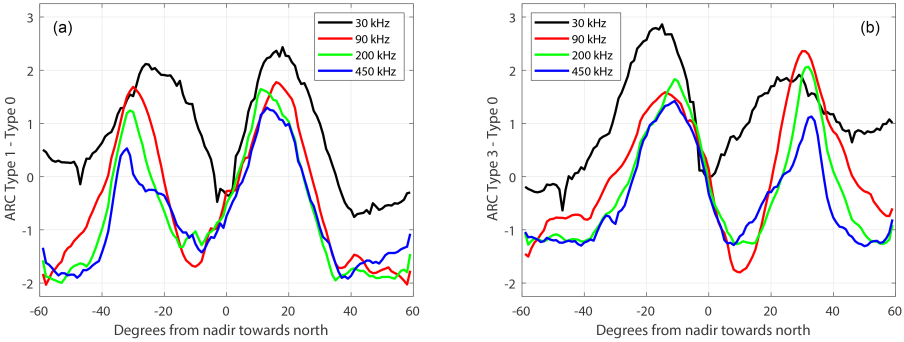

Figure 4.15: (**a**) the difference between the average ARC of Type 1 and Type 0 per frequency; (**b**) the difference between the average ARC of Type 3 and Type 0 per frequency.

4.4.2. Sand-Ripple Effects on Different Frequencies

We now analyze how the sand ripples affect different frequencies. For each frequency, there are clear peaks around ~10° and ~35° (Figures 4.12, 4.13 and 4.15). For the peaks corresponding to the steep lee slopes of the sand ripples lower frequencies generally correspond to higher peaks, with a difference as large as 1.5 dB between the frequencies. For lower frequencies, the peaks are also closer to nadir by up to 8°. For the peaks corresponding to the stoss-side slopes of the sand ripples, no trend for the increasing or decreasing frequencies was found. However, the 200-kHz peak was at 11° and the 30-kHz peak was at 15°, a difference of 4°. The 450-kHz peaks were between the 200-kHz and 90-kHz peaks.

According to [13], different frequencies were similarly affected by sand ripples. They used 300 kHz and 100 kHz, although they did not show the 100-kHz results. They also claimed that angles higher than 40° would not be affected, which is confirmed by our results for frequencies between 90 kHz and 450 kHz. For the 30-kHz data, however, angles higher than 40° were also affected. Furthermore, the effect of the lee slopes was spread over more angles in the case of the 30 kHz data. We hypothesize that this is because the flanks of the lee side slopes are shorter than the 5 cm signal wave length at 30 kHz. As such, these flanks no longer follow a specular scattering regime as assumed by the “facet” model [13], but more of a roughness scattering regime.

For each of the frequencies considered here, the extent of the beam footprint should not have a significant effect on the backscatter response at the angles of the sand ripple slopes. Even in the case of the 450-kHz data, the beam footprint in the shallowest water still had an across-track extent covering more than one sand ripple (Figure 4.16). Additionally, the fact that the lee slopes of the sand ripples affected more angles in the 30-kHz data were not due to a difference in beam footprint. The 90-kHz beam footprint of the R2Sonic had a larger extent than that of the 30-kHz EM 302, and the data were not affected over as many angles.

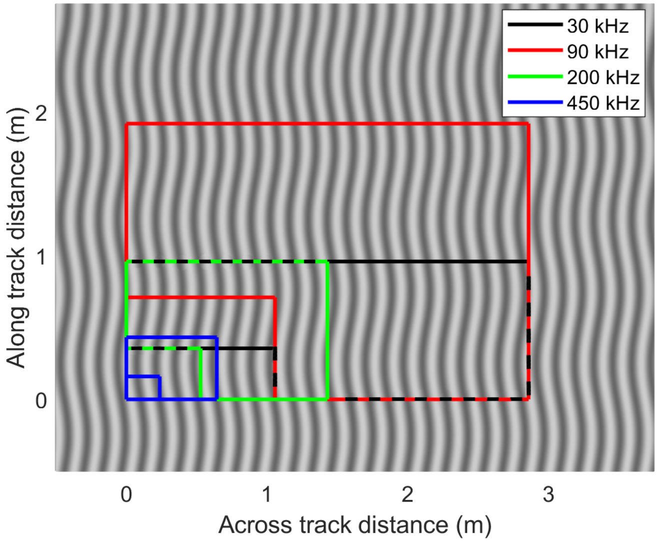

Figure 4.16: Indications of beam footprint extents in comparison to the wavelength of the sand ripples. Black, red, green, and blue rectangles correspond to the footprints for 30, 90, 200, and 450 kHz. The smaller rectangles indicate the extents of the footprint at a 10° beam angle and with the shallowest water depths encountered during the survey. The larger rectangles indicate the extents of the footprints at a 35° beam angle and with the deepest water depths encountered during the survey. The lighter and darker background areas correspond to troughs and crests of sand ripples of the size found in the survey area.

4.4.3. Implications for Backscatter-Based Sediment Classification

Because backscatter is affected by sand ripples, the results in this paper also have implications for the outcome from a number of different types of backscatter-based classification algorithms [42]. These include algorithms where the classification is based on parameter estimation by the fitting of curves to the ARCs [43], algorithms where backscatter intensities are considered per beam angle [11, 14], and algorithms where a correction curve for the mechanical properties of the transducer is calculated [12] using survey data tainted by the presence of undetected sand ripples.

This is not to say that such algorithms cannot be used in sandy areas with high-velocity tidal currents. Algorithms based on ARC fitting may need to be adjusted in such areas—for example, by giving the angles that are the most likely to be affected less weight when fitting the curves. Algorithms considering single beam angles should avoid using beam angles that are affected. According to [13] and our results for frequencies 90 kHz and higher, angles farther from nadir than 40° should not be affected by these types of seabed features. As for the calculation of correction curves for the mechanical properties of the transducer, this research and that of [13] strongly suggest that data from a sandy seafloor area with high current velocities should not be used to calculate the correction curves.

It is common to correct backscatter values for the seafloor slope [11, 12, 36]. The slope correction is performed by using the bathymetry that comes from the same data as the backscatter. As is clear from the case in this research, see Figure 4.6, and is also from [13], the seafloor features that affect the backscatter data here are smaller than the resolution of the MBES bathymetry. As such, for these features, a slope correction cannot be carried out. For future work, it would be worth examining if new developments, like R2Sonic's Ultra High Density (UHD) settings, could resolve these seafloor features. If that is possible, then a slope or other correction may also be within reach for these seafloor features.

However, if a survey was designed and carried out specifically to detect sand ripples, with bathymetry, of the size found here, by mounting an MBES on a remotely operated vehicle (ROV), using high enough frequencies, and slow sailing speeds, the effect encountered here could still not be ruled out, although the effect would then be caused by proportionally smaller ripples. On the flip side, it is also possible that mega ripples, which are easily detected in the bathymetry in this survey, would similarly effect the backscatter of MBESs operating in the deep oceans with low frequencies.

4.4.4. Sand Ripple Detection over Large Geographical Areas

The final and most important matter that this study shows, which would be difficult to show by another methodology, are the large geographical scales at which the sand ripples change. Tidal ridges [24, 25], sand waves [27, 44, 45], and megaripples [28, 46, 47] have been studied at great length over the years, using grab samples, MBES bathymetry, SSS data, and video data, along with sediment transport models. Although these methods are effective for large seafloor structures, it would be challenging to use these in ocean environments for sand ripples. This is due to the small scale of sand ripples and the difficulty of detecting them. Using video systems would be an effective method to study sand ripples in the ocean. However, detailed experiments, for the most part, have been carried out in the lab. SSS imagery may also be able to show at least the presence of these sand ripples, if operated correctly, but it is unknown if the orientation of the sand ripples could be determined [16]. The use of the MBES backscatter, as an acoustic instrument, allows the large-scale study of the behavior of the sand ripples in ways that the other methodologies are unable to do. The results of the backscatter data in this study conclusively show that the orientation of the sand ripples changes to opposite directions across many kilometers of seafloor in a matter of hours.

The results from this research further apply to seafloor classification and monitoring efforts over most of the sandy southern portion of the North Sea. They also apply to many other areas, including places such as the Outer Bristol Channel off the Welsh coast [48], in the western part of the Barents Sea [49], small parts of the Cook Strait [43], and large parts of the continental shelf of the East China Sea and South China Sea [50], to name just a few. All of these areas are sandy areas with a potential for high velocity currents.

4.4.5. Sand ripple detection over large geographical areas

The final and most important matter that the study shows, which would be difficult to show by another methodology, is the large geographical scales at which the sand ripples change. Tidal ridges [25], sand waves [44], and megaripples [27, 28, 45–47] have been studied at great length over the years. The methodologies of these studies include the use of grab samples, MBES bathymetry, SSS data, and video data, along with sediment transport models. Although these methods are effective for large seafloor structures, it would be challenging to use these in ocean environments for sand ripples. This is due to the small scale of sand ripples and the difficulty of detecting them. Using video systems would be an effective method to study sand ripples in the ocean. But detailed experiments for the most part, have been carried out in the lab. The use of the MBES backscatter, as an acoustic instrument, allows the large-scale study of the behavior of the sand ripples in ways that the other methodologies are unable to do. The results of the backscatter data in this study, conclusively show that the orientation of the sand ripples changes, to be in opposite directions, in a matter of hours. And we are able to show this behavior over scales of kilometers, something that another methodology is unable to do at the present time.

4.5. Summary and conclusions

In this chapter, we found that small-scale repeating seafloor structures (sand ripples) have a profound impact on ARCs. These ARCs are calculated from MBES backscatter data. Visible in these ARCs are unexpected off-nadir peaks. These patterns were influenced by the survey azimuth, but not consistent when the survey azimuth was held constant. It was found that the pattern switched on the same time intervals as the switch of the tidal flow direction. Lurton *et al.* [13] found similar survey-azimuth-dependent backscatter patterns. We further show that, even for the same area of seafloor and a constant survey azimuth, backscatter results can differ in time. Video data confirmed that the switch in ARC pattern matched an orientation switch in sand ripples on the seafloor. These results have implications for several currently used classification algorithms. In particular, care must be taken that it is not seafloor morphology, rather than seafloor sediment composition that is being characterized when performing backscatter-based seafloor characterization.

We suggest that the pattern in the ARCs is useful as a diagnostic tool. Firstly, the off-nadir peaks in the ARCs indicate the slope angles of the sand ripples. The slopes indicated by the ARCs in this research matched well with typical sand ripple slopes from the literature. From the two angles, the avalanching observed for the lee-side ripples in the video data allowed the use of the known *angle of repose* for sand in water to be compared with the angles indicated from the ARC patterns. The indicated slopes of the stoss side of the sand ripples are harder to validate.

Another strength of this research is that we had four frequencies of MBES data from the same areas of the seafloor, all gathered at the same time. This was possible by operating two different MBESs simultaneously. The first of these operated at 30 kHz and the other operated at multiple frequencies, 90, 200, and 450 kHz. All of these frequencies were affected similarly by the gentle stoss slopes of the sand ripples. This was evident by similar peaks in the ARCs that matched with the angles expected for these slopes. Furthermore, the ARCs were affected at different angles, with the higher frequencies having a peak at higher beam angles. In addition, for lower frequencies, the ARC peaks were more widely distributed. In the case of the 30-kHz data, beam angles beyond 40° were also affected. For the sand ripples encountered in this research, the 200-kHz data seemed to indicate the sand ripples the best. As such, if a survey was designed with the purpose of detecting sand ripples and only one frequency was available, then 200 kHz would be a good choice to use.

The most important result of this research is that we show a clear link between ARC pattern and sand ripple orientation on the seafloor. This was confirmed by the use of both video ground-truth data and modeled tide-flow data. These patterns could thus be predicted over spatial scales of kilometers. The use of MBES bathymetry would have failed to yield this result, owing to the insufficient resolution of the bathymetry data. Using our methodology, we were able to show that the top centimeter of the seafloor undergoes a complete transformation every six hours in this part of the North Sea. The capability to make such predictions from acoustic data makes these types of measurements an invaluable tool for ocean monitoring.

4.6. Acknowledgments

The authors would like to thank the crew of the R/V Pelagia for their hard work during the cruise to gather the research data. Jip Vrooman (then from the North Sea Foundation) is acknowledged for organizing the data collection cruise. Rian Brak and Jeroen Daams from QPS are thanked for their role in setting up the acquisition system for the R2Sonic MBES. QPS is also thanked for supplying the

Qinsy, *Qimera*, and *Fledermaus* software licenses that were used during the acquisition and processing of the MBES data. Raoul Michels and Elisabeth van Spelden are thanked for their nights of work during survey operations. Marc Philippart and Simon Bicknese from Rijkswaterstaat were vital in supplying the tide model data. Finally, Leendert Dorst and Daniëlle van Kuijk of the Hydrographic Service within the Royal Netherlands Navy were key in making full-coverage high-resolution bathymetric data available from the Brown Bank.

References

[1] L. Koop, K. J. van der Reijden, S. Mestdagh, T. Ysebaert, L. L. Govers, H. Olff, P. M. Herman, M. Snellen, and D. G. Simons, *Measuring centimeter-scale sand ripples using multibeam echosounder backscatter data from the Brown Bank area of the Dutch continental shelf,* Geosciences **10**, 495 (2020).

[2] B. S. Halpern, S. Walbridge, K. A. Selkoe, C. V. Kappel, F. Micheli, C. D'Agrosa, J. F. Bruno, K. S. Casey, C. Ebert, H. E. Fox, R. Fujita, D. Heinemann, H. S. Lenihan, E. M. P. Madin, M. T. Perry, E. R. Selig, M. Spalding, R. Steneck, and R. Watson, *A global map of human impact on marine ecosystems,* Science **319**, 948 (2008), https://www.science.org/doi/pdf/10.1126/science.1149345 .

[3] G. Glegg, R. Jefferson, and S. Fletcher, *Marine governance in the English Channel (La Manche): Linking science and management,* Marine Pollution Bulletin **95**, 707 (2015).

[4] *Busiest shipping lane,* online, Guinness World Records (2020).

[5] R. O. Amoroso, C. R. Pitcher, A. D. Rijnsdorp, R. A. McConnaughey, A. M. Parma, P. Suuronen, O. R. Eigaard, F. Bastardie, N. T. Hintzen, F. Althaus, S. J. Baird, J. Black, L. Buhl-Mortensen, A. B. Campbell, R. Catarino, J. Collie, J. H. Cowan, D. Durholtz, N. Engstrom, T. P. Fairweather, H. O. Fock, R. Ford, P. A. Gálvez, H. Gerritsen, M. E. Góngora, J. A. González, J. G. Hiddink, K. M. Hughes, S. S. Intelmann, C. Jenkins, P. Jonsson, P. Kainge, M. Kangas, J. N. Kathena, S. Kavadas, R. W. Leslie, S. G. Lewis, M. Lundy, D. Makin, J. Martin, T. Mazor, G. Gonzalez-Mirelis, S. J. Newman, N. Papadopoulou, P. E. Posen, W. Rochester, T. Russo, A. Sala, J. M. Semmens, C. Silva, A. Tsolos, B. Vanelslander, C. B. Wakefield, B. A. Wood, R. Hilborn, M. J. Kaiser, and S. Jennings, *Bottom trawl fishing footprints on the world's continental shelves,* Proceedings of the National Academy of Sciences **115**, E10275 (2018), https://www.pnas.org/content/115/43/E10275.full.pdf .

[6] K. J. Van der Reijden, N. T. Hintzen, L. L. Govers, A. D. Rijnsdorp, and H. Olff, *North Sea demersal fisheries prefer specific benthic habitats,* PloS one **13**, e0208338 (2018).

[7] J. Rice, C. Arvanitidis, A. Borja, C. Frid, J. G. Hiddink, J. Krause, P. Lorance, S. Áki Ragnarsson, M. Sköld, B. Trabucco, L. Enserink, and A. Norkko, *Indi-*

cators for sea-floor integrity under the European marine strategy framework directive, Ecological Indicators **12**, 174 (2012), marine Benthic Indicators.

[8] M. Snellen, T. C. Gaida, L. Koop, E. Alevizos, and D. G. Simons, *Performance of multibeam echosounder backscatter-based classification for monitoring sediment distributions using multitemporal large-scale ocean data sets,* IEEE Journal of Oceanic Engineering **44**, 142 (2019).

[9] M. F. Glenn, *Introducing an operational multi-beam array sonar,* The International Hydrographic Review (1970).

[10] G. Lamarche and X. Lurton, *Recommendations for improved and coherent acquisition and processing of backscatter data from seafloor-mapping sonars,* Marine Geophysical Research **39**, 5 (2018).

[11] L. Koop, A. Amiri-Simkooei, K. J van der Reijden, S. O'Flynn, M. Snellen, and D. G Simons, *Seafloor classification in a sand wave environment on the Dutch continental shelf using multibeam echosounder backscatter data,* Geosciences **9**, 142 (2019).

[12] A. C. Schimel, J. Beaudoin, I. M. Parnum, T. Le Bas, V. Schmidt, G. Keith, and D. Ierodiaconou, *Multibeam sonar backscatter data processing,* Marine Geophysical Research **39**, 121 (2018).

[13] X. Lurton, D. Eleftherakis, and J.-M. Augustin, *Analysis of seafloor backscatter strength dependence on the survey azimuth using multibeam echosounder data,* Marine Geophysical Research **39**, 183 (2018).

[14] D. G. Simons and M. Snellen, *A Bayesian approach to seafloor classification using multi-beam echo-sounder backscatter data,* Applied Acoustics **70**, 1258 (2009).

[15] G. Montereale-Gavazzi, M. Roche, K. Degrendele, X. Lurton, N. Terseleer, M. Baeye, F. Francken, and V. Van Lancker, *Insights into the short-term tidal variability of multibeam backscatter from field experiments on different seafloor types,* Geosciences **9**, 34 (2019).

[16] G. R. Elston and J. M. Bell, *Pseudospectral time-domain modeling of non-rayleigh reverberation: synthesis and statistical analysis of a sidescan sonar image of sand ripples,* IEEE Journal of Oceanic Engineering **29**, 317 (2004).

[17] G. A. von Rönn, K. Schwarzer, H.-C. Reimers, and C. Winter, *Limitations of boulder detection in shallow water habitats using high-resolution sidescan sonar images,* Geosciences **9**, 390 (2019).

[18] R. E. Hansen, *Mapping the ocean floor in extreme resolution using interferometric synthetic aperture sonar,* in *Proceedings of Meetings on Acoustics ICU,* Vol. 38 (Acoustical Society of America, 2019) p. 055003.

[19] J. H. Damveld, K. J. van der Reijden, C. Cheng, L. Koop, L. R. Haaksma, C. A. J. Walsh, K. Soetaert, B. W. Borsje, L. L. Govers, P. C. Roos, H. Olff, and S. J. M. H. Hulscher, *Video transects reveal that tidal sand waves affect the spatial distribution of benthic organisms and sand ripples,* Geophysical Research Letters **45**, 11,837 (2018), https://agupubs.onlinelibrary.wiley.com/doi/pdf/10.1029/2018GL079858 .

[20] V. L. Ferrini and R. D. Flood, *The effects of fine-scale surface roughness and grain size on 300 khz multibeam backscatter intensity in sandy marine sedimentary environments,* Marine Geology **228**, 153 (2006).

[21] V. Van Lancker and P. Jacobs, *The dynamical behaviour of shallow-marine dunes.* in *Proceedings of the International Workshop on Marine Sandwave Dynamics / TRENTESAUX A., GARLAN T., (eds.). - Lille : University of Lille 1, 2000* (2000) pp. 213–220.

[22] M. Walgreen, H. E. De Swart, and D. Calvete, *A model for grain-size sorting over tidal sand ridges,* Ocean Dynamics **54**, 374 (2004).

[23] C. Svenson, V. B. Ernstsen, C. Winter, A. Bartholomä, and D. Hebbeln, *Tide-driven sediment variations on a large compound dune in the jade tidal inlet channel, southeastern North Sea,* Journal of Coastal Research , 361 (2009).

[24] T. A. van Dijk, J. A. van Dalfsen, V. Van Lancker, R. A. van Overmeeren, S. van Heteren, and P. J. Doornenbal, *Benthic habitat variations over tidal ridges, North Sea, the Netherlands,* in *Seafloor Geomorphology as Benthic Habitat* (Elsevier, 2012) pp. 241–249.

[25] M. A. Knaapen, *Sandbank occurrence on the Dutch continental shelf in the North Sea,* Geo-marine letters **29**, 17 (2009).

[26] T. A. van Dijk, R. C. Lindenbergh, and P. J. Egberts, *Separating bathymetric data representing multiscale rhythmic bed forms: A geostatistical and spectral method compared,* Journal of Geophysical Research: Earth Surface **113** (2008).

[27] T. Van Oyen, P. Blondeaux, and D. Van den Eynde, *Sediment sorting along tidal sand waves: A comparison between field observations and theoretical predictions,* Continental Shelf Research **63**, 23 (2013).

[28] K. J. Van Der Reijden, L. Koop, S. O'flynn, S. Garcia, O. Bos, C. Van Sluis, D. J. Maaholm, P. M. Herman, D. G. Simons, and H. Olff, *Discovery of sabellaria spinulosa reefs in an intensively fished area of the Dutch continental shelf, North Sea,* Journal of Sea Research **144**, 85 (2019).

[29] M. F. Biber, G. C. Duineveld, M. S. Lavaleye, A. J. Davies, M. J. Bergman, and I. M. van den Beld, *Investigating the association of fish abundance and biomass with cold-water corals in the deep Northeast Atlantic Ocean using a generalised linear modelling approach,* Deep Sea Research Part II: Topical Studies in Oceanography **99**, 134 (2014).

[30] P. Herman, O. Beauchard, and L. van Duren, *De staat van de noordzee,* (Noordzeedagen, 2014).

[31] G. M. Ashley, *Classification of large-scale subaqueous bedforms; a new look at an old problem,* Journal of Sedimentary Research **60**, 160 (1990).

[32] B. Flemming, *Zur klassifikation subaquatischer, strömungstransversaler transportkörper,* Bochumer geologische und geotechnische Arbeiten **29** (1988).

[33] J. H. Baas, *Ripple, ripple mark, ripple structure,* Sedimentology , 921 (1978).

[34] E. Hammerstad, *Em technical note: Backscattering and seabed image reflectivity,* Horten, Norway: Kongsberg Maritime AS , 5 (2000).

[35] T. Gaida, T. Tengku Ali, M. Snellen, A. Amiri-Simkooei, T. van Dijk, and D. Simons, *A multispectral Bayesian classification method for increased acoustic discrimination of seabed sediments using multi-frequency multibeam backscatter data,* Geosciences **8**, 455 (2018).

[36] A. Amiri-Simkooei, M. Snellen, and D. G. Simons, *Riverbed sediment classification using multi-beam echo-sounder backscatter data,* The Journal of the Acoustical Society of America **126**, 1724 (2009).

[37] D. Jackson, *Apl-uw high-frequency ocean environmental acoustic models handbook,* Applied Physics Laboratory, University of Washington, Technical Report **9407** (1994).

[38] *Dutch Continental Shelf Model Modelbeschrijving*, Rijkswaterstaat and Deltares, 1st ed. (2009).

[39] D. Tang, K. L. Williams, and E. I. Thorsos, *Utilizing high-frequency acoustic backscatter to estimate bottom sand ripple parameters,* IEEE Journal of Oceanic Engineering **34**, 431 (2009).

[40] H. M. B. Al-Hashemi and O. S. B. Al-Amoudi, *A review on the angle of repose of granular materials,* Powder technology **330**, 397 (2018).

[41] F.-g. Yang, X.-n. Liu, K.-j. Yang, and S.-y. Cao, *Study on the angle of repose of nonuniform sediment,* Journal of Hydrodynamics **21**, 685 (2009).

[42] C. J. Brown, S. J. Smith, P. Lawton, and J. T. Anderson, *Benthic habitat mapping: A review of progress towards improved understanding of the spatial ecology of the seafloor using acoustic techniques,* Estuarine, Coastal and Shelf Science **92**, 502 (2011).

[43] G. Lamarche, X. Lurton, A.-L. Verdier, and J.-M. Augustin, *Quantitative characterisation of seafloor substrate and bedforms using advanced processing of multibeam backscatter—application to Cook Strait, New Zealand,* Continental Shelf Research **31**, S93 (2011).

[44] M. Knaapen, *Sandwave migration predictor based on shape information,* Journal of Geophysical Research: Earth Surface **110** (2005).

[45] A. Nemeth, *Modelling offshore sand waves,* (2003).

[46] D. Idier, A. Ehrhold, and T. Garlan, *Morphodynamique d'une dune sous-marine du détroît du pas de calais,* Comptes rendus geoscience **334**, 1079 (2002).

[47] R. C. Lindenbergh, T. A. van Dijk, and P. J. Egberts, *Separating bedforms of different scales in echo sounding data,* in *Coastal Dynamics 2005: State of the Practice* (2006) pp. 1–14.

[48] J. C. James, A. S. Mackie, E. I. S. Rees, and T. Darbyshire, *Sand wave field: the obel sands, bristol channel, uk,* in *Seafloor Geomorphology as Benthic Habitat* (Elsevier, 2012) pp. 227–239.

[49] P. Aird, *Chapter 4 - deepwater metocean environments,* in *Deepwater Drilling*, edited by P. Aird (Gulf Professional Publishing, 2019) pp. 111 – 164.

[50] Y. Yincan, *Chapter 15 - development laws of geological hazards and hazard geology regionalization of china seas,* in *Marine Geo-Hazards in China*, edited by Y. Yincan (Elsevier, 2017) pp. 657 – 687.

5

Classifying the seafloor with an object-based image analysis approach using bathymetry and bathymetric derivatives

> *The aim of science is to make difficult things understandable in a simpler way; the aim of poetry is to state simple things in an incomprehensible way. The two are incompatible.*
>
> Paul A.M. Dirac

> *After a certain high level of technical skill is achieved, science and art tend to coalesce in esthetics, plasticity, and form. The greatest sceintists are always artists as well.*
>
> Albert Einstein

In this chapter, object-based image analysis methods are developed that do not rely on backscatter to classify the seafloor. Instead, they make use of bathymetry, bathymetric derivatives, and grab samples for classification. The classification is performed on image object statistics. One of the methods utilizes only texture-based features, that is, features that are related to the spatial arrangement of image characteristics. The second method is similar, but relies on a wider set of image object features. The methods were developed and tested using a dataset from the Røstbanken area off the coast of Lofoten, Norway. The results were compared to backscatter-based classification and to grab-sample ground-reference data. The algorithm that performed the best was then also applied to a dataset from the Borkumer Stones area in Dutch waters. This allowed testing the applicability of the algorithm for different datasets. Because the algorithms that were developed do not require backscatter, the availability of which is much more scarce than bathymetry, and because of the low computational requirements, they could be applied to any area where high-resolution bathymetry and grab samples are available.

Parts of this chapter have been published in Geosciences **11** (2), 45 (2021) [1]

5.1. Introduction

Seafloor mapping has a long history with merchants in the Mediterranean making some of the first organized efforts [2]. Further development of bathymetric maps has continued to the present day [3]. Modern seafloor mapping extends beyond bathymetry and also includes backscatter, a co-located product delivered by multibeam echosounder (MBES) sonars. Backscatter is increasingly used to characterize or classify the seafloor [4–10]. Classification methods range widely, including the use of neural networks [11–13], principle component analysis (PCA) [7, 14–18], Bayesian decision rules [5–7, 9, 19, 20], and textural analysis [21], among others. A recent development to further increase the use of backscatter is the capability of some MBES systems to deliver multi-spectral backscatter data [22] in a single pass over an area of seafloor [9, 10]. Currently, only R2Sonic MBES systems [23] have this capability. Despite backscatter being the preferred datatype for seafloor classification, it remains less available than bathymetry data [24]. Due to the need for up-to-date navigational charts, large portions of the coastal seas are already mapped with high-resolution bathymetry [25]. For the Dutch Continental Shelf (DCS), and the rest of European waters, full-coverage bathymetry data, albeit at lower resolution, are also available for download via the European Marine Observation and Data Network (EMODNet) [26]. Although some backscatter data were made available by the Rijksdienst voor Ondernemend Nederland (RVO) for the De Rijke Noordzee project [27], a centralized backscatter data repository is not in place. At the global scale, less than 18% of the oceans have been directly measured by echosounders [28]. These efforts focus on bathymetry without the mention of backscatter. It would, therefore, be desirable to develop a fast and robust classification method that uses bathymetry and bathymetric derivative layers as input instead of backscatter.

An approach to use the more available bathymetry data, rather than backscatter, for a classification algorithm is an object-based image analysis (OBIA)-based method [29]. OBIA has been widely used for terrestrial mapping [30] and in the past few years has also been increasingly used for seafloor classification [29, 31–34]. Le Bas [35] also developed an arcGIS add-on for OBIA analysis. A strength of the OBIA approach is that image objects can be formed at multiple layers, and the wide range of sub-object features can all be harnessed for classification purposes.

The goal of this chapter is three-fold. The first goal is to develop an OBIA-based classification method that only uses bathymetry, bathymetric derivatives, and grab-sample ground-reference data as input. Secondly, an approach that only uses texture image object features, that is, features that relate to the arrangement of image characteristics instead of the image values themselves, is implemented and tested. Finally, the best performing method is used to investigate how transferable it is to other geographical areas with minimal loss of classification accuracy and minimal adjustment of the algorithm. The developed methods are validated by comparing them to both backscatter-based classification and to grab-sample ground-reference data. Finding a non-backscatter-based classification method would have significant implications for the use of legacy bathymetry data as well as the 2030 global coverage bathymetry [28] data for seafloor classification purposes.

5.2. Study area, materials, and methods

5.2.1. Study area

Datasets from two study areas are considered in this chapter. The first of these study areas is in the Norwegian Sea, ~50 km off the coast of Lofoten, more specifically, off the coast of the Røst Islands (Figure 5.1a). For the remainder of the chapter, this study area is referred to as the Røstbanken area. The dataset from the Røstbanken area includes both backscatter and bathymetry. The data were made available during the 2016 OBIA workshop of the GeoHab conference [36]. The second dataset is from the Borkumer Stones area of the Dutch North Sea (Figure 5.1c). This area is close to the border between Dutch and German waters and the dataset begins only ~10 km off the coast of the Dutch island of Schiermonnikoog, one of the Frisian Islands.

For the Røstbanken study area, both bathymetry and backscatter data are available for a rectangular area ~22 km wide and ~32 km long. The water depth ranges from just under 100 m to almost 300 m deep. The general Røstbanken area shows the typical architecture and glacial land forms that are produced by slow-flowing regions of an ice sheet [37]. During the last glacial maximum, slow moving ice is thought to have covered the Røstbanken area [38]. Røstbanken is also heavily scoured by linear to curvilinear depressions, likely produced by the keels of icebergs [37]. Several such plow marks are visible in the Røstbanken data. For the Røstbanken area, 157 grab samples are available, which indicate a very wide range of sediments from sandy mud to rock.

The water depth in the Borkumer Stones study area ranges in depth from 10 to 35 m (Figure 5.1c). A triangular area of data was made available by the Hydrographic Service of the Royal Netherlands Navy. In the south and north, the dataset is ~23 and ~5 km wide, respectively. In the south to north direction, the dataset is ~50 km long. Much of the seabed of the Borkumer Stones area consists of coarse sand [39], but stones and rocks have also been mapped in this area [40]. Through the years, the presence of reefs have also been found [39–41]. Coolen *et al.* [39] found areas of dense *L. conchilega* beds. For the Borkumer Stones area, 567 grab samples were used for ground truthing the classification results [42, 43].

The base Geo-tiff images

All of the bathymetry and backscatter data for this study are in the form of geo-tiff data images gridded at a 5 m × 5 m resolution. The images were geo-referenced, that is, the exact geographic location of each pixel is known. The Røstbanken data and the Borkumer Stones data used the World Geodetic System (WGS) 1984 UTM Zone 32N and the European Terrestrial Reference System (ETRS) 1989 UTM Zone 31N spatial reference systems, respectively. Although the data had several different coordinate systems, the results presented in this chapter are all projected in the ETRS 1989 UTM Zone 31N spatial reference system for uniformity.

The Røstbanken bathymetry data were collected by multibeam echosounding. The exact location of the sonar, and by extension the location of seafloor being measured, is known based on GPS data combined with the use of MRU data. The bathymetry data were cleaned and are of high quality. The backscatter data were

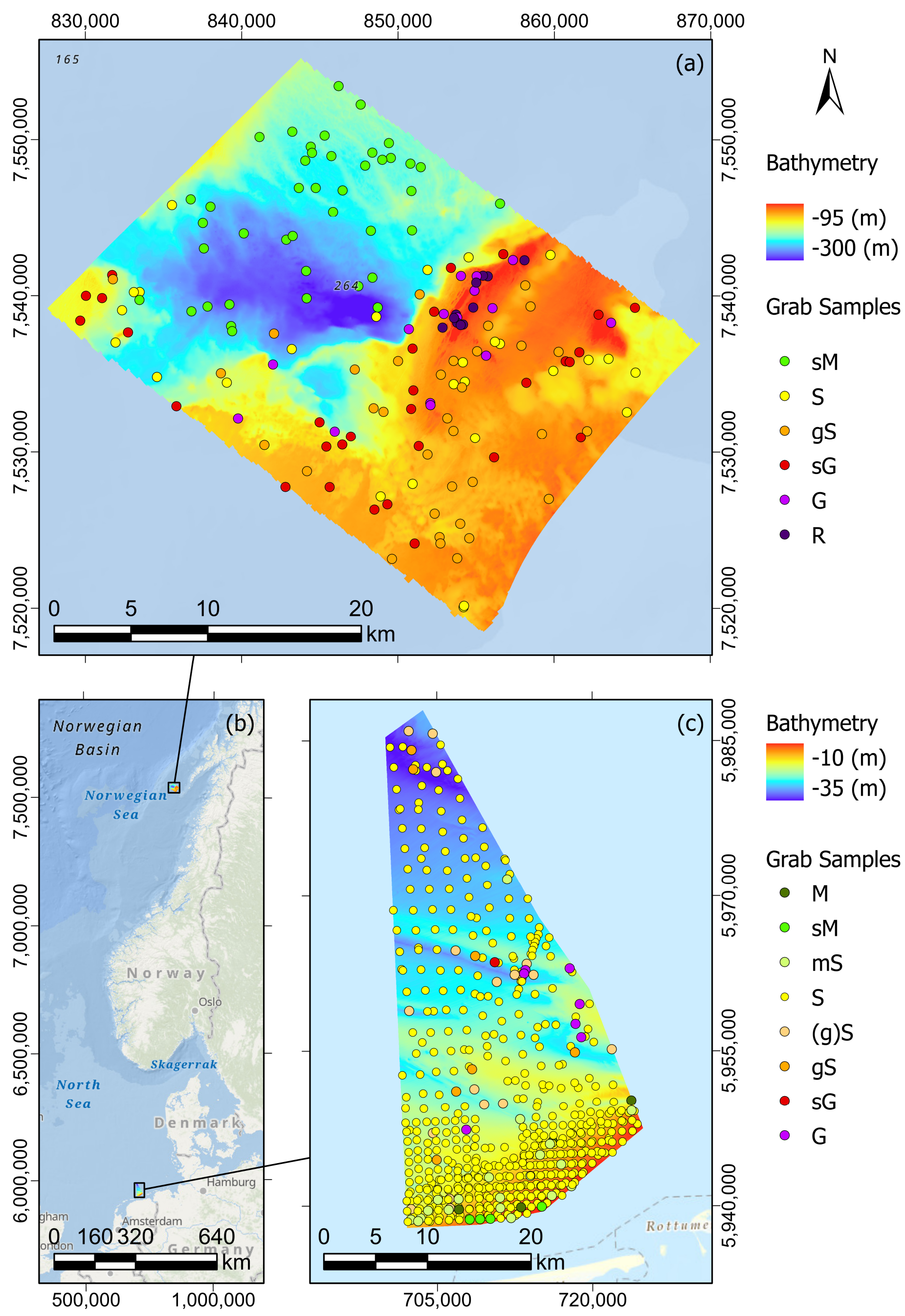

Figure 5.1: (**a**) Bathymetry of the Røstbanken study area. Grab sample locations are shown and the symbols indicate the sediment type in Folk classes (R indicates rock). (**b**) The locations of the two study areas considered in this chapter (data source: [44]). (**c**) Bathymetry of the Borkumer Stones study area. Grab sample locations are shown and the symbols indicate the sediment type in Folk classes.

geo-referenced, and the angular dependence was removed as outlined in [45]. The backscatter was also corrected to compensate for differences in ensonified area and spreading.

For the Borkumer Stones area, only bathymetry, but not backscatter, was available. The northern part of the research area had some data gaps that were interpolated in ArcGIS prior to the layer being used for analysis. Some MBES lines, especially towards the south of the area, had motion artifacts. This was suspected because there were swath wide artifacts perpendicular to the sailing direction, a tell-tale sign of motion artifacts [46]. These types of artifacts can be corrected when raw MRU motion and MBES time of travel information is available [46]. Because the raw data were not available for this research, these artifacts were not removed. The effect of the artifacts on the classification performance is discussed in Section 5.4.3.

Bathymetric derivative layers

In addition to the base layers, which are bathymetry and backscatter, several bathymetric derivative layers were created. These included slope, curvature, aspect, and Bathymetric Position Index (BPI) layers.

Slope The slope of the seafloor is calculated from the bathymetry with the values indicating the deviation from the horizontal in degrees. The slope is calculated with the built-in ArcGIS slope function from the 3D Analyst toolbox. The formula for the calculation of the slope s is as follows

$$s = \frac{180}{\pi} tan^{-1}\left(\sqrt{\left(\frac{dz}{dx}\right)^2 + \left(\frac{dz}{dy}\right)^2}\right) \tag{5.1}$$

where

$$\frac{dz}{dx} = \frac{(z_3 + 2z_6 + z_9) - (z_1 + 2z_4 + z_7)}{8x_s} \tag{5.2}$$

and

$$\frac{dz}{dy} = \frac{(z_7 + 2z_8 + z_9) - (z_1 + 2z_2 + z_3)}{8y_s} \tag{5.3}$$

where x_s and y_s refer to the cell (or pixel) size in the x and y (or north and east) directions, respectively, and z is the depth, or pixel value, where subscripts 1–9 refer to the pixels surrounding the pixel with subscript 5 as in Figure 5.2, where the slope is being calculated for pixel z_5.

Smoothed slope Additionally, a slope based layer was created namely, a smoothed slope. Each pixel in this layer is the mean of the pixels within a radius of 1 km. This layer will have larger values for pixels closer to areas of high slopes, and especially to large areas of high slopes. Importantly, the values will not drop off just outside of a high slope area like the slope layer itself does.

z_1	z_2	z_3
z_4	z_5	z_6
z_7	z_8	z_9

Figure 5.2: Schematic of the pixels used for the calculation of the slope and curvature

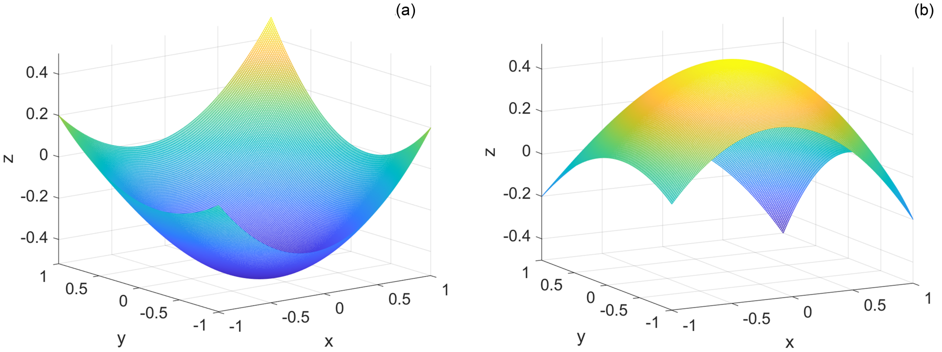

Figure 5.3: (**a**) An exmample of a convex down seafloor, (**b**) and a convex up seafloor

Curvature The curvature of the seafloor is the slope of the slope, or second derivative, of the seafloor and is created with the ArcGIS curvature function according to the method set forth in [47]. The curvature is calculated for point z_5 (Figure 5.2) by taking the depth values at points $z_1 - z_9$ as defined in Figure 5.2 and fitting a quadratic polynomial of the form

$$z = Ax^2y^2 + Bx^2y + Cxy^2 + Dx^2 + Ey^2 + Fxy + Gx + Hy + I \tag{5.4}$$

to these points. This 9-term polynomial exactly fits all 9 points in the 3×3 moving grid. The curvature is the Laplacian $-\nabla^2$ of Equation (5.4) [48, 49] and, because z can be defined such that z_5 is at $(0, 0, z_5)$, simplifies to

$$\nabla^2 z = 2(E + D) = -\frac{(4z_5 - z_2 - z_8 - z_4 - z_6)}{L^2} \tag{5.5}$$

where $E = \left(\frac{z_2+z_8}{2} - z_5\right)/L^2$, $D = \left(\frac{z_4+z_6}{2} - z_5\right)/L^2$, and L is the pixel size ($L = x_s = y_s$ for this application). In our implementation, $curvature = -100\nabla^2$ is used for the actual resultant values in the curvature layer. Thus, a negative value indicates a convex-down seafloor (Figure 5.3a) and a positive value a convex-up seafloor (Figure 5.3b). A value of zero indicates an area where there is no curvature.

Aspect The aspect indicates the compass direction of the steepest slope, and is calculated with

$$aspect = \begin{cases} 90 - \dfrac{180}{\pi}\tan^{-1}\left(\dfrac{\frac{dz}{dy}}{-\frac{dz}{dx}}\right) & \text{if } -\dfrac{dz}{dx} > 0, \\ \dfrac{180}{\pi}\tan^{-1}\left(\dfrac{-\frac{dz}{dx}}{\frac{dz}{dy}}\right) & \text{if } \dfrac{dz}{dy} > 0, \\ 180 + \dfrac{180}{\pi}\tan^{-1}\left(\dfrac{-\frac{dz}{dx}}{\frac{dz}{dy}}\right) & \text{if } \dfrac{dz}{dy} < 0, \\ 270 - \dfrac{180}{\pi}\tan^{-1}\left(\dfrac{\frac{dz}{dy}}{-\frac{dz}{dx}}\right) & \text{if } -\dfrac{dz}{dx} < 0, \\ -1 & \text{if } -\dfrac{dz}{dx} = 0 \text{ and } \dfrac{dz}{dy} = 0. \end{cases} \tag{5.6}$$

where $\frac{dz}{dx}$ and $\frac{dz}{dy}$ are as defined in Equations (5.2) and (5.3). The aspect layer is created using the Aspect tool in the ArcGIS 3D Analysis toolbox. The aspect can fall between the values of 0 being true north and 360 again being north. A shortcoming of using aspect in some situations is that there is a discontinuity at due north. That is, a slope direction of north, northwest, will have values close to 360 and a similar slope direction of north, northeast, will have values close to 0.

Bathymetric position index The BPI is the underwater equivalent of the terrestrial "Topographic Position Index" that is often used as a parameter for habitat modeling [50–52]. The BPI is a measure of seafloor depth relative to the surrounding seafloor and is defined as follows

$$BPI_{r_p} = z_5 - \overline{z_{r_p}} \tag{5.7}$$

where $\overline{z_{r_p}}$ is the mean depth indicated by all pixels within a given radius r_p of the pixel z_5. Needless to say, the resulting BPI layer depends strongly on r_p. With smaller r_p, local features are accentuated, but, with large enough r_p, regional features are dominant. Ten different BPI layers were created with r_p and r_d radius, in pixels and distance, respectively, shown in Table 5.1.

Table 5.1: Radii r_d in distances for BPI layers with radii measured in pixels r_p.

r_p	r_d
BPI_3	15 m
BPI_5	25 m
BPI_{10}	50 m
BPI_{25}	125 m
BPI_{50}	250 m
BPI_{100}	500 m
BPI_{200}	1 km
BPI_{400}	2 km
BPI_{800}	4 km
BPI_{1000}	5 km

5.2.2. Methods

All of the layers described in the previous section are used in a segmentation algorithm to create image objects. Statistics from the image objects are then used for seafloor classification. The creation of both the image objects and the classification methods is now addressed. The segmentation and classification is carried out using the *Trimble* software *eCognition* (versions 9.2.1 and 9.5.0).

Object-based image analysis

Image objects The principle for OBIA is that instead of considering an image only on the basis of its pixels, it is considered on the bases of image objects, where an image object is defined as a set of image pixels. Image objects are furthermore organized into different levels. At the pixel level the image objects are the same as the pixels (see Figure 5.4a). A segmentation of the image, starting from the pixel level, creates a higher level of image objects (this layer is called "Fine" in Figure 5.4a). Further segmentation can then be carried out on the image object level to create even higher levels of image objects ("Medium" and "Coarse" in Figure 5.4a).

For each of these image objects, a host of statistics can be calculated to create image object features. These features are later used during the classification stage. Image object features include statistics about the size, shape, or the mean color[1] of any of the layers of an object. They can also include features of image objects at different levels. For example, to carry out a classification at image object Level 3 (Figure 5.4c), image object features of sub-objects at Level 2 (objects with white borders in Figure 5.4d) or at Level 1 (objects with black borders in Figure 5.4e) can be used. Finally, the use of features from neighboring image objects are also used in this chapter.

Creating image objects by multiresolution segmentation A very commonly used image segmentation algorithm in OBIA is the multiresolution segmentation

---

[1] Color, here and for the rest of the chapter, refers to the pixel value (or the mean value of sub-objects in the case of higher level segmentations) of a particular image.

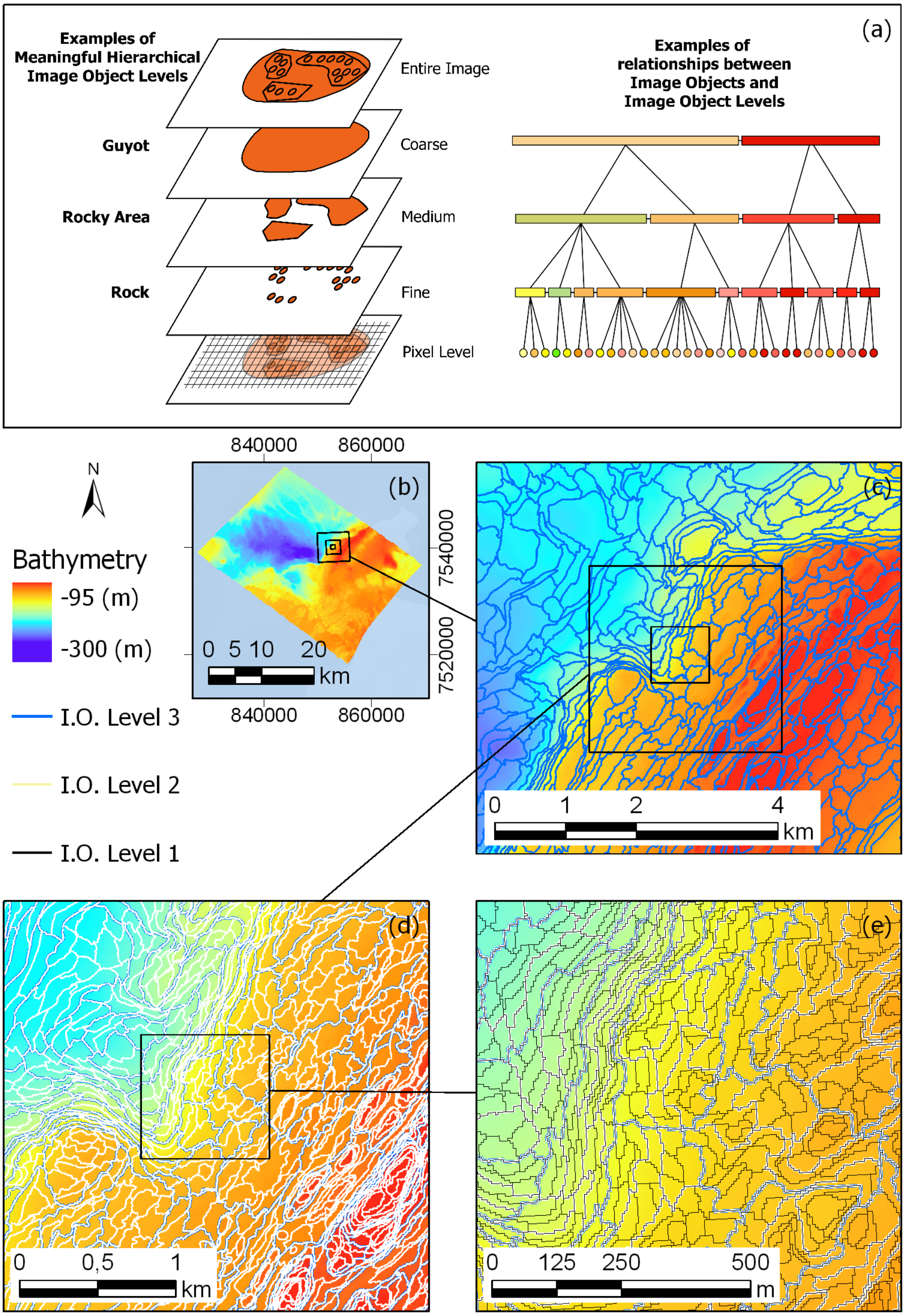

Figure 5.4: (**a**) Examples of meaningful hierarchical image object levels and relationships between image objects and image object levels (sub-figure after [53] and [54]). (**b**) Bathymetry of the Røst study area, black rectangles indicate the extents depicted in (c), (d), and (e). (**c**) Blue polygons indicate Level 3 ("Coarse" in (a)) image objects, the black rectangles indicate the extents of (d) and (e), the background color indicates bathymetry (also holds for (d) and (e)). (**d**) White polygons indicate Level 2 ("Medium" in (a)) image objects, borders shared between image objects of Level 2 and 3 have a blue outline, the black rectangle indicates the extent shown in (e). (**e**) Black polygons indicate Level 1 image objects ("Fine" in (a)), borders shared between image objects of Level 1 and 2 have a white outline, and borders shared between image objects of Level 1 and 3 have a blue outline.

algorithm [55]. This algorithm starts by considering every pixel within an image to be an image object. Neighboring image objects are iteratively merged to form larger image objects while minimizing the within object heterogeneity h [56]. The heterogeneity, as described by [54], is a combination of both color c and shape s heterogeneity. The heterogeneity change Δh is defined as

$$\Delta h = w_c \Delta h_c + w_s \Delta h_s \tag{5.8}$$

where w_c and w_s are user specified weights such that $0 \le w_c, w_s \le 1$ and $w_c + w_s = 1$. These weights allow the value of the heterogeneity to be adapted for emphasis on color or shape heterogeneity. For example, a bathymetry layer might have the value of -32 that corresponds to the depth at that pixel location. The amount of color heterogeneity change Δh_c is defined as

$$\Delta h_c = \sum_{\ell=1}^{N} w_\ell \left(n_m \sigma_{\ell,m} - \left(n_1 \sigma_{\ell,1} + n_2 \sigma_{\ell,2} \right) \right). \tag{5.9}$$

Here, N is the number of image layers considered in the segmentation process (see Table 5.2), w_ℓ is the weight assigned to the ℓth image layer, n_i refers to the number of pixels in the image object, and $\sigma_{\ell,i}$ is the within object standard deviation of image object i of image layer ℓ. The subscript $i \in (1, 2, m)$ refers to the separate objects 1 and 2 that are being considered for merging or to the potential image object m that would result from merging image objects 1 and 2.

The shape s of an image object is dependent on the compactness com and smoothness sm of an image object. Compactness is the ratio of the perimeter length of the image object and the area of the image object. Smoothness is the ratio of the perimeter length of the image object and the perimeter length of the bounding box within which the image object would fit [54]. The change in the shape heterogeneity Δh_s is given by

$$\Delta h_s = w_{com} \Delta h_{com} + w_{sm} \Delta h_{sm}. \tag{5.10}$$

where w_{com} and w_{sm} are user specified and restricted as w_c and w_s are.

Compactness change Δh_{com} is given as

$$\Delta h_{com} = \frac{n_m p_m}{\sqrt{n_m}} - \left(\frac{n_1 p_1}{\sqrt{n_1}} + \frac{n_2 p_2}{\sqrt{n_2}} \right) \tag{5.11}$$

where n is the number of pixels in the object and p is the perimeter of the image object. The subscripts $m, 1$ and 2 refer to the merged object, object 1, and object 2, as defined above. The change in smoothness Δh_{sm} is given as

$$\Delta h_{sm} = \frac{n_m p_m}{b_m} - \left(\frac{n_1 p_1}{b_1} + \frac{n_2 p_2}{b_2} \right) \tag{5.12}$$

where b is the perimeter of a box that bounds the object and n, p, and the subscripts are defined as above.

For every loop of the algorithm, each image object is "visited" once [56] (p. 68). For a starting "seed" image object o_1, the algorithm looks for the neighboring image object o_2 such that, if they were merged, the heterogeneity change Δh would be minimum, i.e. the best fit. If the best fit for image objects o_1 and o_2 is not mutual, then object o_2 becomes the seed to continue the search for objects to merge. This process is stopped when no more image objects can be merged such that Δh is less than a certain, user specified, threshold called a "scale parameter" S_p.

For this research, three levels of segmentation were performed (Figure 5.4c–e) with different settings per segmentation level (Table 5.2). For the first of the image object levels, the finest level, the image objects were intended to conform to the smallest features in the bathymetry. To accomplish this, the generated image layers were examined to see which layers most clearly showed small-scale seabed features. Small scale features, as referred to in this work, are of such size that they are present over at least a few image pixels. They are the smallest distinct features that can be reliably perceived in the data by visual inspection. Because they span a few image pixels, they are likely to measure several tens of meters physically. Image layers that were useful at first level were layers such as slope, BPI layers with a small radii, and aspect. Although the aspect layer accentuates small features, it was not used, because of its discontinuity at due north. The image layer weights and the scale parameter S_p were selected such that the shapes of the image objects conformed to the small-scale seafloor features. Additionally, the heterogeneity used during the segmentation process depended largely on color and not on image object shape (see Section 5.2.2). This allowed the shapes of the image objects to better conform to the shapes of small-scale seafloor features, which allowed shape related image object features (statistics) to better indicate the presence of seafloor features.

At the second level of image objects, it was still desired that image objects would conform to small seafloor features. However, to gain the most benefit from having multiple image object layers, it was necessary to select a scale parameter such that each image object at this level was composed of at least a few image objects from the lower level. As was the case for the segmentation at Level 1, the heterogeneity of the segmentation was set to mostly be dependent on the color parameter and not on the shape parameter.

At the third level of image object segmentation, the focus changed significantly. At this level, much more emphasis was placed on image object shape and less on image object color. In addition, the choice of layer(s) was made such that larger scale seafloor features would fall within image objects. Based on a subjective examining of the different layers, BPI_{400} was a good layer to use for this segmentation level. The larger the image objects were, the more lower level sub-objects they contained. Because the texture-based features were calculated from sub-objects, larger image objects and more sub-objects also meant that the discrimination power of texture features was greater. However, because making the image objects too large would decrease the resolution of the classification results, a balance in image object size was sought. In any case, the scale parameter was selected such that multiple image objects of Levels 1 and 2 were contained in the highest level of

Table 5.2: Parameters and layers used for each level of image object creation. The image objects from segmentation Level 1 correspond to those seen in Figure 5.4 (e), Level 2 to Figure 5.4 (d), Level 3 to Figure 5.4 (c)

Segment. level	**Scale Parameter (S_p)**	**Shape (w_s)**	**Compact. (w_{com})**	**Layer weights (w_ℓ)**	**Layers**
1	3	0.02	0.5	1	Bathymetry
				1	BPI_3
				1	BPI_5
				2	BPI_{10}
				2	BPI_{25}
				2	BPI_{50}
				2	BPI_{100}
				2	BPI_{200}
				2	BPI_{400}
				1	Curvature
				2	Slope
2	10	0.02	0.5	1	Bathymetry
				1	BPI_3
				1	BPI_5
				2	BPI_{10}
				2	BPI_{25}
				2	BPI_{50}
				2	BPI_{100}
				2	BPI_{200}
				2	BPI_{400}
				1	Curvature
				2	Slope
3	50	0.5	0.5	1	BPI 400

image objects at Level 3.

Classification

Three methods of classification are used in this chapter. Each of the methods is performed on image objects features which were discussed in the previous section. The three classification methods are as follows:

- **Method 1** is threshold based and uses image object features from the backscatter, bathymetry, and BPI_5 layers. The thresholds are those used in the 2016 OBIA workshop of the GeoHab conference [36] and were developed at the Center for Environment Fisheries and Aquaculture Science (CEFAS) [57]. This approach was not developed within the current research, but its results are considered as a standard to which Methods 2 and 3 can be measured.
- **Method 2** uses a Classification And Regression Tree (CART), a binary tree predictive model to go from observations about an item to conclusions about

the items target value or class (a more in-depth description follows below) [58]. The CART provides the thresholds which are then used in a similar way as in Method 1. This method uses only texture features from image objects.

- **Method 3** is similar to Method 2, however, it uses both texture and direct layer image object features. That is, it does not only use texture-based features, which relate to the arrangement of layer values, but it also references layer values directly, such as the average depth within an image object.

The image objects at Level 3, created by the third application of the multiresolution segmentation, are used to classify the seafloor sediments. Grab samples classified according to Folk are used to create a training dataset for a CART. Firstly, each image object that coincides with the location of a grab sample is classified according to the Folk class of that grab sample. Based on these classified image objects the CART is constructed.

The CART is constructed in a top down greedy approach. At each step, an image object feature at Level 3 is chosen that best splits the set of classified image objects. The Gini impurity index is used to measure the "best" split. It is calculated for each candidate subset and the results are combined to form a measure of the quality of the split. The Gini impurity at node n_p is calculated as

$$I_G(n_p) = 1 - \sum_{i=1}^{J} p_i^2 \tag{5.13}$$

where p_i is the fraction of items labeled as class i and $i \in \{1, 2, ..., J\}$ where J is the number of classes. I_G reaches its minimum ($I_G = 0$) when all cases in a node are of the same class.

After the classification tree is constructed, every image object at Level 3 is classified using the tree. Given the attributes of the image object, the decision tree is traversed from the root node until it is classified at a leaf node (brightly colored rectangles in of the tree.

To compare the classification to grab sample ground-reference data, the grab sample sets were subdivided to create a training and a validation set. For the comparisons against other classification methods, the full grab sample set was used as a training set for the CART.

The final classification map was greatly improved by cleaning up the classification results as follows. For each research area, the most common seafloor sediment type was used such that any image object classified in a different class, but surrounded or largely surrounded by the sediment type that was most dominant, was reclassified into the most dominant class. For the Røstbanken data, this dominant class was sandy mud. For the Borkumer Stones area, this class was sand. Making use of a clean up step similar to this is common practice in OBIA classification

5.3. Results

In this section, the classification results are shown. Firstly, Method 1 (see Section 5.2.2) is applied to the data from the Røstbanken area. These results are then

Table 5.3: Error matrix comparing backscatter-based class to grab-sample based class. The data are also shown in Figure 5.6.

		Grab-sample Class							
		sM	**S**	**gS**	**sG**	**G**	**R**	**Row Totals**	**Accuracy**
Backscatter-based class	**sM**	42	7	0	0	0	0	**49**	**85.7%**
	S	0	16	4	1	0	0	**21**	**76.2%**
	gS	0	4	21	5	1	0	**31**	**67.7%**
	sG	0	0	9	18	2	0	**29**	**62.0%**
	G	0	0	0	6	10	5	**21**	**47.6%**
	R	0	0	0	0	2	6	**8**	**75.0%**
	Column totals	**42**	**27**	**34**	**30**	**15**	**11**	**Overall accuracy:**	**71.1%**

used to validate the results of Methods 2 (Figure 5.5b) and 3 (Figure 5.5c). The quality of the classification results from Method 1 is checked by comparison to grab-sample ground-reference data (Figure 5.6). The results from Methods 2 and 3 are compared to grab-sample ground-reference data as well, and to the backscatter-based results of Method 1. After this, Method 3 is applied to the Borkumer Stones area (Section 5.3.2).

5.3.1. Røstbanken results

Method 1, backscatter-based classification

Firstly, a baseline classification is established by the use of Method 1 (Figure 5.5a). For this classification, thresholds on the different layers are used to classify the area. The most prominently used layer is the backscatter layer. Aside from backscatter, bathymetry is also used repeatedly and the within object standard deviation of BPI_5 is used once.

The deeper northwestern half (Figure 5.1a) of the study area has the largest area of uniform sediment, of type sandy mud (sM, Figure 5.5). On the northwestern edge of the study area, some coarser mixed sediments are also found. In the southeastern half of the study area, a mixture of sediments is found ranging from sand to rock.

When these classification results are compared to the ground-reference data (Figure 5.6 and Table 5.3), it is seen that there is a good agreement. For each sediment type, the classification matches the grab-sample type the majority of the time. Overall, 71% of the time the match was perfect, and 98.7% of the time the classification was within ± 1 class of the grab-sample type.

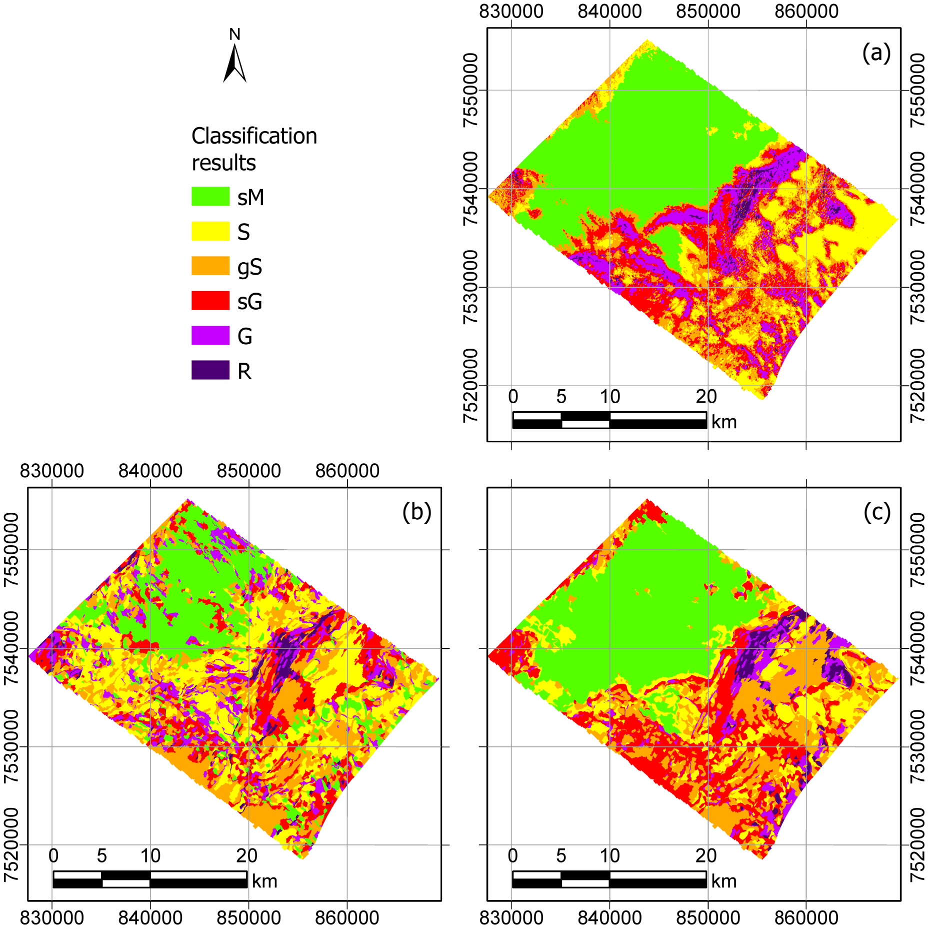

Figure 5.5: Classification maps of the Røstbanken study area. (**a**) Classification based on backscatter data (Method 1), (**b**) texture features only (Method 2), and (**c**) texture and layer features (Method 3).

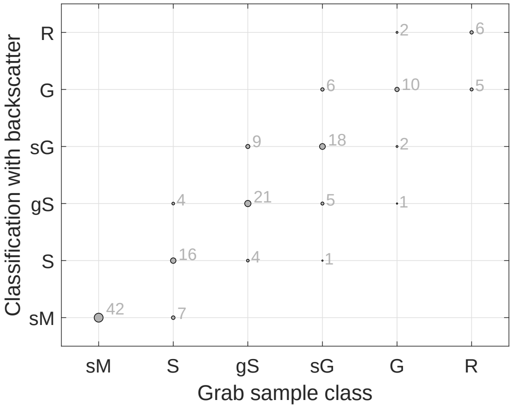

Figure 5.6: Correlation between backscatter-based classification (Method 1) and sediment type at grab-sample locations. Dots, with the associated text, indicate the number of matches class and sediment type.

Method 2, classification using only textural image object features

Next, Method 2, a texture only-based classification, is performed (Figure 5.5b). For this method, none of the layers mentioned in Section 5.2.1 are directly referenced. Rather, texture-related image object features are used. The backscatter layer is not used at any point, that is, not in the classification and also not in the segmentation stage, of the procedure. The segmentation was carried out with the layers and layer weights given in Table 5.2. The CART utilized 11 different object features at 24 different nodes (Figure 5.7a and Table 5.4). The object feature as well as its deciding value is given for each node in Figure 5.7. Left branches are followed if the values are less than the value indicated at the node. Right branches are followed if the values are equal to or greater than the decision point. The leaves of the tree indicate the class label for the image object in question. Table 5.4 gives a description of each of the image object features that are used in the CART.

When using only texture-based image object features (Method 2), the resulting classification map is mixed. The large sM area (northwest half of the research area, Figure 5.5a) is distinguishable (Figure 5.5b). There is also a rocky area close to 7,540,000 N and 854,000 E that is resolved well with this method. However, the large sM area is not cleanly classified as sM, but has small areas that are classified as harder substrate, up to and including gravel. In the mixed sediment area (southeast), there is a trend of the coexistence of harder and softer substrates in agreement with Figure 5.5a. However, the exact spatial occurrence of classes differs between the two maps.

For the results shown in Figure 5.5b, all the grab samples were used for training the CART. To further assess the performance of Method 2, a different approach is also taken, where the grab-sample dataset is subdivided into non-overlapping training and validation subsets. Figure 5.8a explicitly shows the correlation between the classification and the grab samples. The area around sand grab samples is seen to be classified as gravely sand more often than as sand. Sandy gravel areas, in turn, are just as likely to be classified as gravely sand and almost as likely to be classified as gravel. Of the 78 validation grab samples, the texture-based classification produced a perfect match 35 times, or with 45% accuracy (Table 5.5 and Figure 5.8a). The classification was accurate to ±1 class 57 times, or 73% of the time.

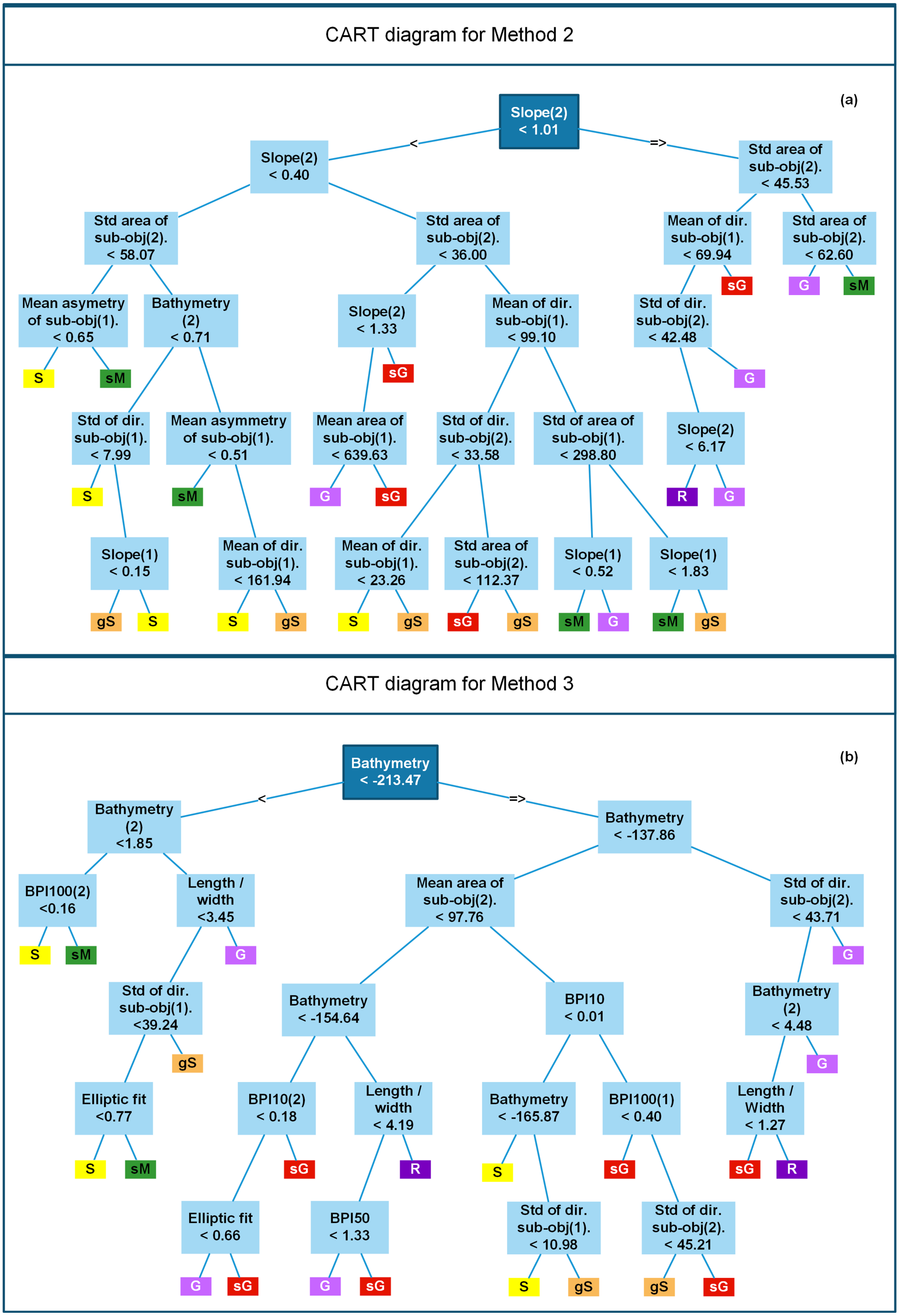

Figure 5.7: (**a**) Diagram of the CART for texture only based classification (Method 2) (see Figure 5.5 (b)). (**b**) Diagram of the CART for texture and layer based classification (Method 3) (see Figure 5.5 (c)). Text in each box indicates the object feature used and its value for the decision rule. Left branches indicate the *less than* direction and right branches indicate the *greater than or equal to* direction.

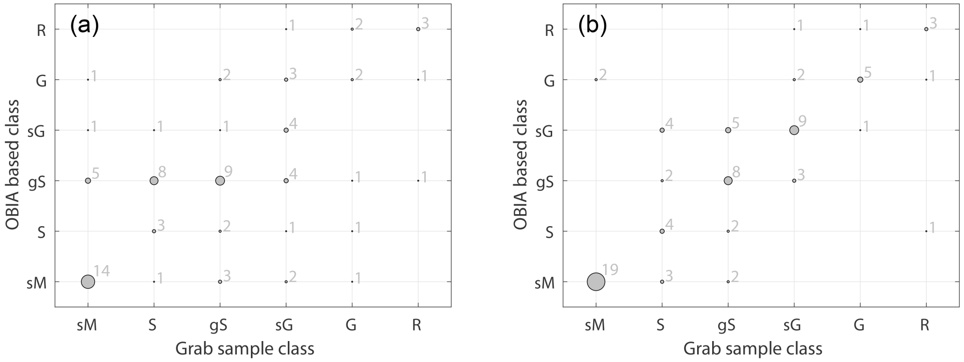

Figure 5.8: (**a**) Correlation between classification results from Method 2 and sediment type at grab-sample locations. (**b**) Correlation between classification results from Method 3 and sediment type at grab-sample locations. Corresponding error matrices are shown in Tables 5.5 and 5.7.

Table 5.4: A list of each of the image object features that formed a node in the CART of Figure 5.7(a). Also listed is the number of times each of these object features appears as a node, and a description of what the object feature is.

Layer name	**Number of times referenced**	**Object feature description**
Slope(2)	4	The standard deviation of the means of the slope values within sub-objects at Level 1 [56, p. 402-403] or the average of the mean differences of each sub-object to its neighboring objects at Level 1 [56, p. 403-404].
Std area of sub-obj(2)	4	The standard deviation of the area of the image objects at Level 1 that fall into the image object in question at Level 3.
Mean of dir. sub-obj(1)	4	The mean of the main direction of all of the sub objects at Level 2 that are in the object in question at Level 3.
Slope(1)	3	The standard deviation of the means of the slope values within sub-objects at Level 2 [56, p. 402-403] or the average of the mean differences of each sub-object to its neighboring objects at Level 2 [56, p. 403-404].
Mean asymmetry of sub-objects(1)	2	The mean of the asymmetry of sub-objects at Level 2 that fall within the object in question at Level 3. Asymmetry is the relative length of an image object compared to a regular polygon (a similar measure as the Length / Width) [56, p. 357-358]
Std of dir. sub-obj(2)	2	The standard deviation of the main direction of all of the sub objects at Level 2 that are in the object in question at Level 3.
Std of dir. sub-obj(1)	1	The standard deviation of the main direction of all of the sub objects at Level 1 that are in the object in question at Level 3.
Bathymetry(2)	1	The standard deviation of the means of the bathymetry values within sub-objects at Level 1 [56, p. 402-403] or the average of the mean differences of each sub-object to its neighboring objects at Level 1 [56, p. 403-404].
Mean area of sub-obj.(1)	1	The mean area of the image objects at Level 2 that fall into the image object in question at Level 3.
Std of area of sub-obj(1)	1	The standard deviation of the area of the image objects at Level 2 that fall into the image object in question at Level 3.
Std of dir. sub-obj(2)	1	The standard deviation of the area of the image objects at Level 1 that fall into the image object in question at Level 3.

Table 5.5: Error matrix comparing classification results using Method 2 to grab-sample-based class. The data are also shown in Figure 5.8a.

		Grab-sample Class							
		sM	**S**	**gS**	**sG**	**G**	**R**	**Row Totals**	**Accuracy**
OBIA-based class	**sM**	14	1	3	2	1	0	**21**	**66.7%**
	S	0	3	2	1	1	0	**7**	**42.9%**
	gS	5	8	9	4	1	1	**28**	**32.1%**
	sG	1	1	1	4	0	0	**7**	**62.2%**
	G	1	0	2	3	2	1	**9**	**22.2%**
	R	0	0	0	1	2	3	**6**	**50.0%**
	Column totals	**21**	**13**	**17**	**15**	**7**	**5**	**Overall accuracy:**	**44.9%**

Table 5.6: A list of each of the image object features that formed a node in the CART of Figure 5.7(b). Also listed is the number of times each of these object features appears as a node, and a description of what the object feature is.

Layer name	**Number of times referenced**	**Object feature description**
Bathymetry	4	The mean of the within object pixels (at Level 3) of the bathymetry layer.
Length / width	3	The ratio of the length / width of an image object at Level 3 [56, p. 353-354]
Elliptic fit	2	The shape of the image object at level three is compared to an ellipse the same length and width as the image object. The area of the image object that falls outside the ellipse vs. the area inside the ellipse yields the fit value [56, p. 362-363]
Std of dir. sub-obj(1)	2	The standard deviation of the main direction of all of the sub objects at Level 2 that are in the object in question at Level 3.
Bathymetry(2)	2	The standard deviation of the means of the bathymetry values within sub-objects at Level 1 [56, p. 402-403] or the average of the mean differences of each sub-object to its neighboring objects at Level 1 [56, p. 403-404].
Std of dir. sub-obj(2)	2	The standard deviation of the main direction of all of the sub objects at Level 1 that are in the object in question at Level 3.
BPI_{50}	1	The mean of the within object pixels (at Level 3) of the BPI_{50} layer.
BPI_{10}	1	The mean of the within object pixels (at Level 3) of the BPI_{10} layer.
$BPI_{100}(1)$	1	The standard deviation of the means of the BPI_{100} values within sub-objects at Level 2 [56, p. 402-403] or the average of the mean differences of each sub-object to its neighboring objects at Level 2 [56, p. 403-404].
$BPI_{100}(2)$	1	The standard deviation of the means of the BPI_{100} values within sub-objects at Level 1 [56, p. 402-403] or the average of the mean differences of each sub-object to its neighboring objects at Level 1 [56, p. 403-404].
$BPI_{10}(2)$	1	The standard deviation of the means of the BPI_{10} values within sub-objects at Level 1 [56, p. 402-403] or the average of the mean differences of each sub-object to its neighboring objects at Level 1 [56, p. 403-404].
Mean area of sub-obj.(2)	1	The mean area of the image objects at Level 1 that fall into the image object in question at Level 3.

Method 3, classification using image object parameters and non backscatter data

A significant improvement in classification is achieved, still not using the backscatter data, when referencing the image layer values directly, during the implementation of Method 3 (Figure 5.5c). The image object features and deciding values of the CART are seen in Figure 5.7b. How many times each feature is used and a description of what the features represent are given in Table 5.6.

When the classification is compared to ground-reference data, the improvement to Method 2 becomes clear (Figure 5.8b). For every grab type, except sand, the majority of the classification classes match the grab-sample class. For sand, the classification results was equally likely to be sandy gravel. Of the 78 grab samples, the classification matched exactly 48 times (or 61%) (Table 5.7 and Figure 5.8b) and (or 87%) the classification results were within ±1 class of the grab-sample class 68 times.

Comparing non-backscatter-based classification to backscatter-based classification

Assuming that the backscatter-based classification is accurate, then we can compare the results from Methods 2 and 3 with the backscatter-based classification results from Method 1, in a pixel-by-pixel comparison. For the area that has a specific class based on Method 1, Figure 5.9 shows, by percentage, how those areas were classified by Methods 2 and 3. Figure 5.9a shows this relationship where the results of Method 3 are compared to the results from Method 1. Figure 5.9b shows the results of Method 2 compared to the results of Method 1.

When using Method 3, the sM area was correctly classified above 90% of the time. For the rest of the classes, the correct classification was between 30% and just over 40%. The percentage of correct classification with a tolerance of ±1 class was 86% for the entire area. Per sediment type, it was as follows: sandy mud 92%, sand 81%, gravely sand 86%, sandy gravel 83%, gravel 77%, and rock 73%.

For Method 2 (Figure 5.9b), the results were not as good. Only sandy mud was correctly classified most of the time. The ±1 class percentage was 52% for the entire area, and per sediment type it was as follows: sandy mud 86%, sand 55%, gravely sand 59%, sandy gravel 71%, gravel 60%, and rock 8%.

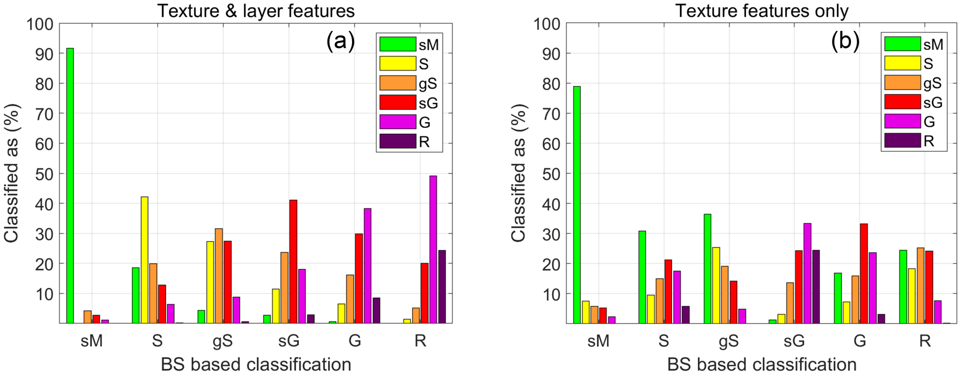

Figure 5.9: (**a**) Comparison of class result from Method 3 for areas having a specific class based on Method 1. (**b**) Comparison of class result from Method 2 for areas having a specific class based on Method 1.

Table 5.7: Error matrix comparing classification results using Method 3 to grab-sample-based class. The data are also shown in Figure 5.8b.

		Grab-sample Class							
		sM	**S**	**gS**	**sG**	**G**	**R**	**Row Totals**	**Accuracy**
OBIA-based class	**sM**	19	3	2	0	0	0	**21**	**90.5%**
	S	0	4	2	0	0	1	**7**	**57.1%**
	gS	0	2	8	3	0	0	**13**	**61.5%**
	sG	0	4	5	9	1	0	**19**	**47.4%**
	G	2	0	0	2	5	1	**10**	**50.0%**
	R	0	0	0	1	1	3	**5**	**60.0%**
	Column totals	**21**	**13**	**17**	**15**	**7**	**5**	**Overall accuracy:**	**61.5%**

5.3.2. Borkumer Stones results

By using the Røstbanken dataset where backscatter, a good sampling of grab samples, and high quality bathymetry data were available to develop a bathymetry and bathymetric derivative OBIA-based classification method, insights into the performance of the OBIA classification method were obtained. These insights can be applied to the DCS dataset. Based on its performance, Method 3 was used. However, some minor changes to the scale parameter were needed. This was done in order to have the first two levels of image objects conform to small-scale features, as was the case for the Røstbanken data.

For the Bokumer Stones area, a very similar CART was trained as for the Røstbanken data. The branches and leaves, along with the layer at each node, including the deciding value, are shown in Figure 5.10. The object features that were used in the CART, along with their description, and the number of times each feature was referenced in the CART are presented in Table 5.8.

To ground truth the classification results (Figure 5.11a) with grab-sample data, the grab samples were divided into training and validation sets. In the validation set, there were 139 grab samples, of which 123 were of class sand (Figure 5.12). For 91 of the 139 samples (65%), there was a perfect match between the OBIA class and the grab-sample class (Table 5.9 and Figure 5.12). For 117 of the samples (or 84%), the OBIA results were within ± 1 class of the grab-sample class.

For the Røstbanken area, it was possible to compare the OBIA classification results to results from a separate classification method based on backscatter (Method 1). However, for the Borkumer Stones area, backscatter was not available. Although a comparison to grab-sample ground-reference data was made, it would be preferable to also have a second comparison method. For this, a different feature of the ground-reference data was used, namely the D50 values, which are similar to the Folk classes that were used to train the CART, but not identical. These are used to generate a second full-coverage map for comparison. This map, shown in Figure 5.11b, is a Kriging-based interpolation of the D50 values of the grab samples. By visual comparison of Figure 5.11a,b, large-scale trends are found to agree.

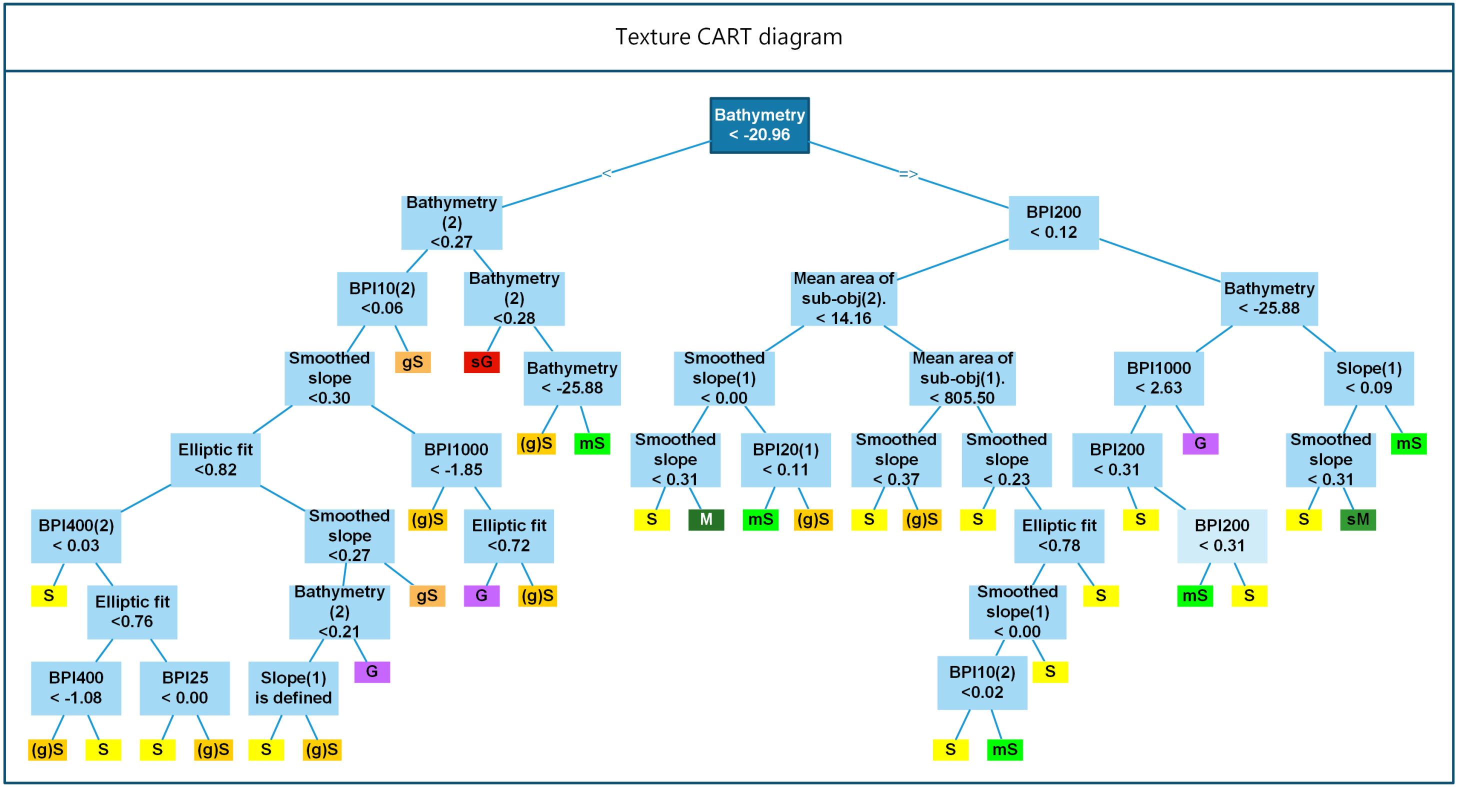

Figure 5.10: Diagram of the CART for the classification in the Borkumer Stones area. Text in each box indicates the object feature used and its value for the decision rule. Left branches indicate the less than direction and right branches indicate the greater than or equal to direction.

Table 5.8: A list of each of the image object features that formed a node in the CART of Figure 5.10. Also listed is the number of times each of these object features appears as a node, and a description of what the object feature is.

Layer name	**Number of times referenced**	**Object feature description**
Smoothed slope	6	The mean of the within object pixels (at Level 3) of the smoothed slope layer.
Elliptic fit	4	See Table 5.6
Bathymetry	3	The mean of the within object pixels (at Level 3) of the bathymetry layer.
BPI_{200}	3	The mean of the within object pixels (at Level 3) of the BPI_{200} layer.
Bathymetry(2)	3	See Table 5.4
BPI_{1000}	2	The mean of the within object pixels (at Level 3) of the BPI_{1000} layer.
$BPI_{10}(2)$	2	The standard deviation of the means of the BPI_{10} values within sub-objects at Level 1 [56, p. 402-403] or the average of the mean differences of each sub-object to its neighboring objects at Level 1 [56, p. 403-404].
Smoothed slope(1)	2	The standard deviation of the means of the smoothed slope values within sub-objects at Level 2 [56, p. 402-403] or the average of the mean differences of each sub-object to its neighboring objects at Level 2 [56, p. 403-404].
Slope(1)	2	The standard deviation of the means of the slope values within sub-objects at Level 2 [56, p. 402-403] or the average of the mean differences of each sub-object to its neighboring objects at Level 2 [56, p. 403-404].
BPI_{400}	1	The mean of the within object pixels (at Level 3) of the BPI_{400} layer.
BPI_{25}	1	The mean of the within object pixels (at Level 3) of the BPI_{25} layer.
$BPI_{400}(2)$	1	Similar to $BPI_{10}(2)$ Object feature above, but with BPI_{400} layer.
$BPI_{20}(1)$	1	The standard deviation of the means of the BPI_{20} values within sub-objects at Level 2 [56, p. 402-403] or the average of the mean differences of each sub-object to its neighboring objects at Level 2 [56, p. 403-404].
Mean area of sub-obj.(2)	1	The mean area of the image objects at Level 1 that fall into the image object in question at Level 3.
Mean area of sub-obj.(1)	1	The mean area of the image objects at Level 2 that fall into the image object in question at Level 3.

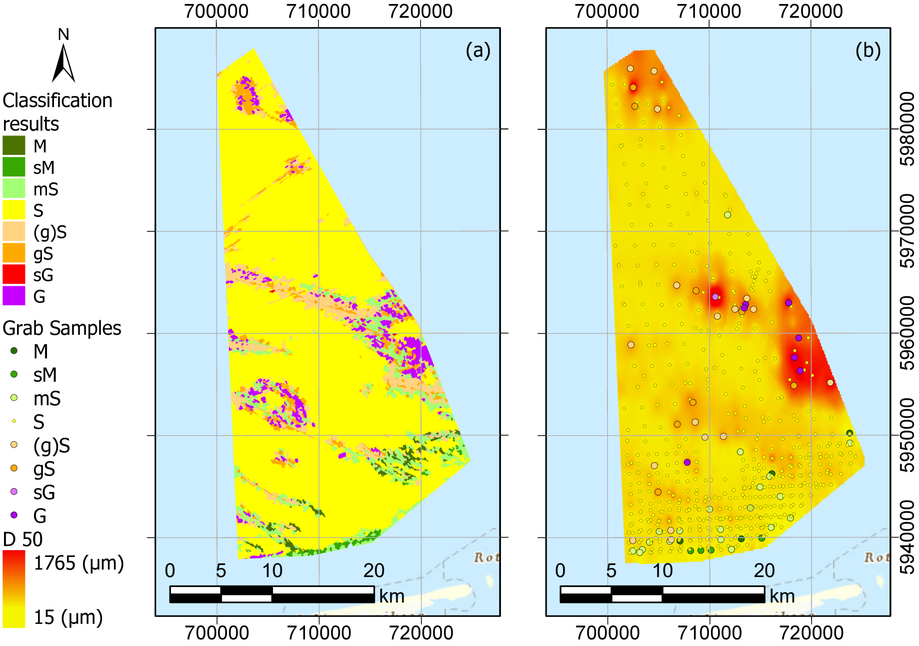

Figure 5.11: (**a**) Classification results from the Borkumer Stones area of the Dutch North Sea. (**b**) A D50 map interpolated from grab samples. Grab-sample locations are shown classified according to Folk.

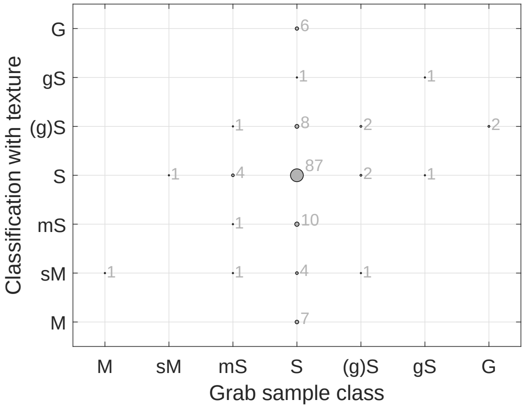

Figure 5.12: Texture based classification results from the Borkumer Stones area compared to grab-sample ground-truth data.

Table 5.9: Error matrix comparing classification results, from the Borkumer Stones area, using Method 3 to grab-sample-based class. The data are also shown in Figure 5.12.

		Grab-sample Class								
		M	**sM**	**mS**	**S**	**(g)S**	**gS**	**G**	**Row Totals**	**Accuracy**
OBIA-based class	**M**	0	0	0	7	0	0	0	**7**	**0.0%**
	sM	1	0	1	4	1	0	0	**7**	**0.0%**
	mS	0	0	1	10	0	0	0	**11**	**9.0%**
	S	0	1	4	87	2	1	0	**95**	**91.6%**
	(g)S	0	0	1	8	2	0	2	**13**	**15.4%**
	gS	0	0	0	1	0	1	0	**2**	**50.0%**
	G	0	0	0	6	0	0	0	**6**	**0%**
	Column totals	**1**	**1**	**7**	**123**	**5**	**2**	**2**	**Overall accuracy:**	**64.5%**

5.4. Discussion

5.4.1. The performance of OBIA methods

One of the research questions addressed in this chapter is if a fast and reliable texture-based classification method can be found. It should be noted that there is a family of texture-based methods, such as those based on Haralick texture features, that are commonly used in the literature which were not tested. This is because these methods tend to be exceedingly computationally intensive [59, 60] and the interest is in a fast method. Therefore, an OBIA approach was investigated. For this research, the software package *eCognition* was used. Once the rule sets for the OBIA-based classification were developed, the methods were applied to a dataset covering hundreds of square kilometers in a matter of minutes. Because of the speed of the OBIA methods, they were well suited to get a rapid overview of large areas of the seafloor. It should be noted that the OBIA methods were only used on image datasets with a resolution of 5 m × 5 m. Of the different stages of the classification process, the segmentation stage was the most computationally expensive. The run-time of the multi segmentation algorithm grows linearly with an increase in number of pixels [61]. Given the run times of Methods 2 and 3 with the datasets used in this study, it is expected that, for datasets covering areas up to the entire DCP (59,000 km^2) at resolutions currently available (5–25 m^2 pixel sizes) [25], this algorithm would remain well suited when used on modern high performance desktop computers (Quad core processor or better, 64 GB of RAM or better). However, if the method were applied to datasets that either cover much larger areas or have a much higher resolution than those mentioned in this chapter, then computation time and memory bottlenecks would need to be considered [62].

As far as the reliability of the classification results are concerned, the two methods that were developed in this chapter (Methods 2 and 3, Section 5.2.2) had differing reliability results. When compared to grab samples, classification accuracies of 98.7%, 73%, and 87% were achieved with a tolerance of ± 1 class for Methods 1–3, respectively. Assuming Method 1 to yield a correct classification allowed for Methods 2 and 3 to be compared to it on a pixel by pixel bases. When this was done, Methods 2 and 3 had an accuracy of 52% and 86%, respectively, again with a tolerance of ± 1 classes. Since the layer and grab sample inputs for Methods 2 and 3 are the same, and given the fact that they differed little in computational requirements, the use of Method 3 is recommended instead of Method 2. However, the texture features that Method 2 is based on should certainly be included in future OBIA methods. This is recommended based on the fact that they were included in Method 3 and were used for almost half of the nodes of the CART of Method 3 (Figure 5.7b and Table 5.6).

5.4.2. Application of the algorithm to different datasets

A testament to the robustness of the OBIA methods developed in this chapter is the fact that very little needed changing when Method 3 was applied to a different dataset in order to achieve good classification results. Some changes were necessary for the image objects at Levels 1 and 2 to conform to the shape of small-scale seafloor features. To accomplish this, the scale parameter was adjusted for these two levels of image segmentation. The weights of the image layers used during the segmentation was also adjusted to utilize the best layers for the given area. This indicates that, as long as image objects are allowed to conform to the shapes of small-scale seafloor features at the lower levels of image objects, then this method remains applicable to new datasets.

5.4.3. The effect of bathymetry flaws

From the data that were used in this research, the dataset from the Borkumer Stones area had some bathymetric flaws. These errors were likely the result of uncorrected or poorly corrected motion sensor or lever arm artifacts [46]. The artifacts were consistent in their across track, along track, and sailing direction specific patterns that is typical of this kind of error. Because of these flaws, there were some areas where the lower level image objects conformed to artifacts instead of to real seafloor features. This may explain why the classification from the Borkumer Stones data, when compared to grab-sample ground-reference, was not quite as good as the results for the Røstbanken data (when using an accuracy measure of ±1 acoustic class). Because of the OBIA-based classification method's reliance on image objects conforming to actual seafloor features, clean bathymetry data are of high importance for the classification method developed in this chapter.

Another research question that would be worth investigating, is to see what effect using bathymetry of different resolutions would have on the classification accuracy. This could be done by using a high-resolution data set and successively decreasing the resolution while repeatedly carrying out the same classification method. This would also answer the question of how well the OBIA methods developed in this chapter could be applied to lower resolution legacy bathymetry data.

5.4.4. Good use cases for bathymetry-based OBIA based classification

Because of the need for up-to-date navigational charts, many countries collect high-resolution bathymetry data covering big sections of their territorial waters on regularly scheduled intervals [25]. This means that high-quality bathymetry data are widely available. Furthermore, as a part of the 2030 project, high-resolution bathymetry data will become available for the entirety of the world's oceans [28]. Unlike bathymetry, backscatter data remain much harder to come by.

It is difficult to quantify the ratio of the seafloor for which bathymetry is available but backscatter is not. There is little focus on the gathering of backscatter at the global scale, and with good reason, as even the well-funded and well-organized MAREANO, Norway's national offshore mapping program, had difficulty dealing with the size of such backscatter datasets [63]. Of the efforts to collect full-coverage backscatter data, MAREANO is a good example, as well as Germany where side scan sonars are widely used [64, 65]. For the DCS, full-coverage bathymetry data are available via EMODnet [26]. In addition to this, bathymetry data up to a resolution of 25 m ×25 m (and in some cases 5 m ×5 m), can be requested of the Hydrographic

Service of the Royal Netherlands Navy. The Navy surveys the entirety of the DCS on scheduled intervals. Backscatter is not available through any of these means. The Royal Netherlands Institute for Sea Research (NIOZ) can at any moment have some backscatter data available, but they do not have a long-term storage plan for backscatter data gathered during their cruises. An example where backscatter data were made available by the RVO on the DCS is the case of the "De Rijke Noordzee", who were able to analyze ~1200 km^2 that was gathered during surveys for the placing of wind farms [27]. Because there is no centralized gathering point for backscatter data, it is difficult to quantify the area for which backscatter data exist for many regional coastal waters, while it is well known that full-coverage bathymetry exists.

At the global scale, there are organized efforts, especially after the disappearance of Malaysia Airlines flight MH370 and the subsequent search, to collect bathymetry data [28, 66]. Due to this, there are also good estimates on how much of the global seafloor has been measured by echosounders, and it is less than 18% [28]. The fact that backscatter is much less available is also demonstrated by the fact that it is not even mentioned in these efforts [28, 66]. This is further confirmed by the fact that the standardization for the acquisition and interpretation of backscatter data is still a very active field of research [24].

Because bathymetry is more readily available than backscatter, it is desirable to develop fast and accurate classification methods that do not rely on backscatter data. Such methods could then be applied in order to provide classification results of large areas of many European and American coastal seas, among others. When full-coverage bathymetry data of the entire globe become available, such methods can then be applied at the global scale. Although backscatter-based classification still yields better results, OBIA classification results using only bathymetry and its derivatives yielded classification results with a 10% loss in accuracy. As such, the methods developed in this chapter should be considered as good options in circumstances where backscatter data are not available.

5.5. Summary and conclusions

In this chapter, two seafloor classification methods were developed that use an OBIA approach. The methods use bathymetry, bathymetric derivatives, and grab samples as input, and they do not rely on the use of backscatter. The transferability of the best method was tested by applying it to two datasets. The first dataset was from Norwegian waters, specifically the Røstbanken area off the coast of Lofoten. The second dataset was from Borkumer Stones area close to the island of Schiermonnikoog in Dutch waters. The classification results were compared to the results from an existing backscatter-based classification method (Method 1) in the case of the Røstbanken data, and to grab-sample ground-reference data for both datasets.

The first of the developed methods (Method 2) used a purely texture-based OBIA approach. The second method (Method 3) was similar, but used additional image object features. Both methods are fast enough to be used over large coastal areas with data resolutions of 5 m × 5 m. To apply the method(s) to new areas, adjustments to the scale parameter of the segmentation algorithm were necessary.

Additionally, when creating the first two levels of image objects, image layer choice was important in order for the shapes of the image objects to conform to small-scale features of the seafloor. With these adjustments, the algorithm was transferable to new research areas.

When comparing Methods 1–3 to grab-sample ground-reference data, a respective classification accuracy of 98.7%, 73%, and 87% was found when a tolerance of ±1 class was used. When only perfect matches are considered, then the accuracies are 71%, 45%, and 61%, respectively. When compared to the results from Method 1, Method 2 had an accuracy of 52% and Method 3 an accuracy of 86% with a ±1 class tolerance. Because the input requirements and computation cost do not differ significantly between Methods 2 and 3, the use of Method 3 is recommended.

Having a bathymetry and bathymetric derivative-based classification method is important given that bathymetry data are more available than backscatter data for many coastal seas. This importance is even greater when considering full global coverage of bathymetric data being available through projects such as the GEBCO seabed 2030 project [28]. As such, the results presented in this chapter should be of wide interest to the seafloor classification community.

5.6. Acknowledgments

The authors would like to acknowledge Markus Diesing and his colleagues at CEFAS for their work in acquiring and processing the Røstbanken dataset. The organizers of the GeoHab 2016 workshop, where the Røstbanken data was made available are also acknowledged [36]. Leendert Dorst and Daniëlle van Kuijk of the Hydrographic Service within the Royal Netherlands Navy are thanked for making full-coverage, high resolution, bathymetric data available from the Borkumer stones area. Finally, Sytze van Heteren of TNO is acknowledged for making the grab-sample data for the Borkumer stones available for this research [42]. The EMODnet-Geology [67], TILES [68], and AufMod [69] projects are further recognized for their part in the compilation of the grab-sample data.

References

[1] L. Koop, M. Snellen, and D. G. Simons, *An object-based image analysis approach using bathymetry and bathymetric derivatives to classify the seafloor,* Geosciences **11** (2021), 10.3390/geosciences11020045.

[2] J. Blake, *The sea chart: the illustrated history of nautical maps and navigational charts* (Anova Books, 2009).

[3] D. Monahan, *Bathymetry,* in *Encyclopedia of Ocean Sciences (Second Edition)*, edited by J. H. Steele (Academic Press, Oxford, 2009) second edition ed., pp. 297 – 304.

[4] C. J. Brown, S. J. Smith, P. Lawton, and J. T. Anderson, *Benthic habitat mapping: A review of progress towards improved understanding of the spa-*

tial ecology of the seafloor using acoustic techniques, Estuarine, Coastal and Shelf Science **92**, 502 (2011).

[5] L. Koop, A. Amiri-Simkooei, K. J van der Reijden, S. O'Flynn, M. Snellen, and D. G Simons, *Seafloor classification in a sand wave environment on the Dutch continental shelf using multibeam echosounder backscatter data,* Geosciences **9**, 142 (2019).

[6] D. G. Simons and M. Snellen, *A Bayesian approach to seafloor classification using multi-beam echo-sounder backscatter data,* Applied Acoustics **70**, 1258 (2009).

[7] M. Snellen, T. C. Gaida, L. Koop, E. Alevizos, and D. G. Simons, *Performance of multibeam echosounder backscatter-based classification for monitoring sediment distributions using multitemporal large-scale ocean data sets,* IEEE Journal of Oceanic Engineering **44**, 142 (2019).

[8] G. Lamarche, X. Lurton, A.-L. Verdier, and J.-M. Augustin, *Quantitative characterisation of seafloor substrate and bedforms using advanced processing of multibeam backscatter—application to Cook Strait, New Zealand,* Continental Shelf Research **31**, S93 (2011).

[9] T. Gaida, T. Tengku Ali, M. Snellen, A. Amiri-Simkooei, T. van Dijk, and D. Simons, *A multispectral Bayesian classification method for increased acoustic discrimination of seabed sediments using multi-frequency multibeam backscatter data,* Geosciences **8**, 455 (2018).

[10] C. J. Brown, J. Beaudoin, M. Brissette, and V. Gazzola, *Multispectral multibeam echo sounder backscatter as a tool for improved seafloor characterization,* Geosciences **9**, 126 (2019).

[11] G. Y. Ojeda, P. T. Gayes, R. F. Van Dolah, and W. C. Schwab, *Spatially quantitative seafloor habitat mapping: example from the northern South Carolina inner continental shelf,* Estuarine, Coastal and Shelf Science **59**, 399 (2004).

[12] I. Marsh and C. Brown, *Neural network classification of multibeam backscatter and bathymetry data from Stanton Bank (Area IV),* Applied Acoustics **70**, 1269 (2009).

[13] D. Stephens and M. Diesing, *A comparison of supervised classification methods for the prediction of substrate type using multibeam acoustic and legacy grain-size data,* PloS one **9**, e93950 (2014).

[14] C. McGonigle, C. Brown, R. Quinn, and J. Grabowski, *Evaluation of image-based multibeam sonar backscatter classification for benthic habitat discrimination and mapping at stanton banks, uk,* Estuarine, Coastal and Shelf Science **81**, 423 (2009).

[15] C. McGonigle, J. H. Grabowski, C. J. Brown, T. C. Weber, and R. Quinn, *Detection of deep water benthic macroalgae using image-based classification techniques on multibeam backscatter at cashes ledge, gulf of maine, usa,* Estuarine, Coastal and Shelf Science **91**, 87 (2011).

[16] C. J. Brown, B. J. Todd, V. E. Kostylev, and R. A. Pickrill, *Image-based classification of multibeam sonar backscatter data for objective surficial sediment mapping of georges bank, canada,* Continental Shelf Research **31**, S110 (2011).

[17] D. Eleftherakis, A. Amiri-Simkooei, M. Snellen, and D. G. Simons, *Improving riverbed sediment classification using backscatter and depth residual features of multi-beam echo-sounder systems,* The Journal of the Acoustical Society of America **131**, 3710 (2012).

[18] D. Eleftherakis, M. Snellen, A. Amiri-Simkooei, D. G. Simons, and K. Siemes, *Observations regarding coarse sediment classification based on multi-beam echo-sounder's backscatter strength and depth residuals in Dutch rivers,* The Journal of the Acoustical Society of America **135**, 3305 (2014).

[19] A. Amiri-Simkooei, M. Snellen, and D. G. Simons, *Riverbed sediment classification using multi-beam echo-sounder backscatter data,* The Journal of the Acoustical Society of America **126**, 1724 (2009).

[20] K. J. Van Der Reijden, L. Koop, S. O'flynn, S. Garcia, O. Bos, C. Van Sluis, D. J. Maaholm, P. M. Herman, D. G. Simons, and H. Olff, *Discovery of sabellaria spinulosa reefs in an intensively fished area of the Dutch continental shelf, North Sea,* Journal of Sea Research **144**, 85 (2019).

[21] P. Blondel and O. G. Sichi, *Textural analyses of multibeam sonar imagery from Stanton Banks, Northern Ireland continental shelf,* Applied Acoustics **70**, 1288 (2009).

[22] J. E. H. Clarke, *Multispectral acoustic backscatter from multibeam, improved classification potential,* in *Proceedings of the United States Hydrographic Conference, San Diego, CA, USA* (2015) pp. 15–19.

[23] E. Vas, *Multispectral mode™ survey capability.* Online (2016).

[24] G. Lamarche and X. Lurton, *Recommendations for improved and coherent acquisition and processing of backscatter data from seafloor-mapping sonars,* Marine Geophysical Research **39**, 5 (2018).

[25] R. N. Navy, *Online availability of data of the Netherlands Hydrographic Service,* Online (2020).

[26] *Developing and providing a harmonised Digital Terrain Model (DTM) for the European sea regions,* Online (2021).

[27] T. C. Gaida, *Onderzoek naar zeebodem in de noordzee,* Online (2021).

[28] L. Mayer, M. Jakobsson, G. Allen, B. Dorschel, R. Falconer, V. Ferrini, G. Lamarche, H. Snaith, and P. Weatherall, *The nippon foundation—GEBCO seabed 2030 project: The quest to see the world's oceans completely mapped by 2030,* Geosciences **8**, 63 (2018).

[29] M. Diesing, P. Mitchell, and D. Stephens, *Image-based seabed classification: what can we learn from terrestrial remote sensing?* ICES Journal of Marine Science **73**, 2425 (2016).

[30] T. Blaschke, *Object based image analysis for remote sensing,* ISPRS journal of photogrammetry and remote sensing **65**, 2 (2010).

[31] M. Diesing, S. L. Green, D. Stephens, R. M. Lark, H. A. Stewart, and D. Dove, *Mapping seabed sediments: Comparison of manual, geostatistical, object-based image analysis and machine learning approaches,* Continental Shelf Research **84**, 107 (2014).

[32] Ł. Janowski, J. Tęgowski, and J. Nowak, *Seafloor mapping based on multibeam echosounder bathymetry and backscatter data using object-based image analysis: a case study from the rewal site, the southern baltic,* Oceanological and Hydrobiological Studies **47**, 248 (2018).

[33] M. Lacharité, C. J. Brown, and V. Gazzola, *Multisource multibeam backscatter data: developing a strategy for the production of benthic habitat maps using semi-automated seafloor classification methods,* Marine Geophysical Research **39**, 307 (2018).

[34] P. S. Menandro, A. C. Bastos, G. Boni, L. C. Ferreira, F. V. Vieira, A. C. Lavagnino, R. L. Moura, and M. Diesing, *Reef mapping using different seabed automatic classification tools,* Geosciences **10**, 72 (2020).

[35] T. P. Le Bas, *Rsobia-a new obia toolbar and toolbox in arcmap 10. x for segmentation and classification,* (2016).

[36] GeoHab, *Marine environment mapping and interpretation - from the coast to the deep ocean, second circular,* Online (2020).

[37] A. Micallef, S. Krastel, and A. Savini, *Submarine Geomorphology* (Springer, 2017).

[38] D. Ottesen, J. Dowdeswell, and L. Rise, *Submarine landforms and the reconstruction of fast-flowing ice streams within a large quaternary ice sheet: the 2500-km-long norwegian-svalbard margin (57–80 n),* GSA Bulletin **117**, 1033 (2005).

[39] J. W. Coolen, O. G. Bos, S. Glorius, W. Lengkeek, J. Cuperus, B. van der Weide, and A. Agüera, *Reefs, sand and reef-like sand: A comparison of the benthic biodiversity of habitats in the Dutch Borkum reef grounds,* Journal of Sea Research **103**, 84 (2015).

[40] O. T. Olsen, *The Piscatorial Atlas of the North Sea, English and St. George's Channels: Illustrating the Fishing Ports, Boats, Gear, Species of Fish (how, where and when Caught), and Other Information Concerning Fish and Fihseries* (OT Olsen, 1883).

[41] J. Dörjes, *Über die bodenfauna des Borkum riffgrundes (nordsee),* Senckenbergiana marit **9**, 1 (1977).

[42] J. Valerius, V. Van Lancker, S. Van Heteren, J. Leth, and M. Zeiler, *Transnational database of North Sea sediment data,* Data compilation by Federal Maritime and Hydrographic Agency (Germany); Royal Belgian Institute of Natural Sciences (Belgium); TNO (Netherlands) and Geological Survey of Denmark and Greenland (Denmark) .

[43] D. Stephens and M. Diesing, *Towards quantitative spatial models of seabed sediment composition,* PloS one **10**, e0142502 (2015).

[44] Esri, *World topographic map,* Online (2012).

[45] A. C. Schimel, J. Beaudoin, I. M. Parnum, T. Le Bas, V. Schmidt, G. Keith, and D. Ierodiaconou, *Multibeam sonar backscatter data processing,* Marine Geophysical Research **39**, 121 (2018).

[46] J. E. H. Clarke, *Dynamic motion residuals in swath sonar data: Ironing out the creases,* The International hydrographic review (2003).

[47] L. W. Zevenbergen and C. R. Thorne, *Quantitative analysis of land surface topography,* Earth surface processes and landforms **12**, 47 (1987).

[48] I. D. Moore, R. Grayson, and A. Ladson, *Digital terrain modelling: a review of hydrological, geomorphological, and biological applications,* Hydrological processes **5**, 3 (1991).

[49] D. Zaslavsky and G. Sinai, *Surface hydrology: I. explanation of phenomena,* Journal of the Hydraulics Division **107**, 1 (1981).

[50] A. Weiss, *Topographic position and landforms analysis,* in *Poster presentation, ESRI user conference, San Diego, CA*, Vol. 200 (2001).

[51] E. R. Lundblad, D. J. Wright, J. Miller, E. M. Larkin, R. Rinehart, D. F. Naar, B. T. Donahue, S. M. Anderson, and T. Battista, *A benthic terrain classification scheme for american samoa,* Marine Geodesy **29**, 89 (2006).

[52] S. Walbridge, N. Slocum, M. Pobuda, and D. J. Wright, *Unified geomorphological analysis workflows with benthic terrain modeler,* Geosciences **8**, 94 (2018).

[53] Trimble, *eCognition Developer User Guide*, 9th ed. (2016).

[54] U. C. Benz, P. Hofmann, G. Willhauck, I. Lingenfelder, and M. Heynen, *Multiresolution, object-oriented fuzzy analysis of remote sensing data for gis-ready information,* ISPRS Journal of photogrammetry and remote sensing **58**, 239 (2004).

[55] M. Baatz and A. Schäpe, *Multiresolution segmentation: an optimization approach for high quality multi-scale image segmentation. 2000,* Wichmann-Verlag , 12 (2000).

[56] Trimble, *eCognition Developer Reference Book*, Trimble.

[57] M. Diesing and N. E. Jørgensen, *Revision of cefas seabed analysis ruleset,* private communication.

[58] L. Breiman, J. Friedman, C. Stone, and R. Olshen, *Classification and Regression Trees*, The Wadsworth and Brooks-Cole statistics-probability series (Taylor & Francis, 1984).

[59] H. Zhang, C.-L. Hung, G. Min, J.-P. Guo, M. Liu, and X. Hu, *Gpu-accelerated glrlm algorithm for feature extraction of mri,* Scientific reports **9**, 1 (2019).

[60] K. Doycheva, C. Koch, and M. König, *Implementing textural features on gpus for improved real-time pavement distress detection,* Journal of Real-Time Image Processing **16**, 1383 (2019).

[61] O. Csillik, *Fast segmentation and classification of very high resolution remote sensing data using slic superpixels,* Remote Sensing **9**, 243 (2017).

[62] O. Csilik and S. Lang, *Improving the speed of multiresolution segmentation using slic superpixels,* (2016).

[63] S. Elvenes, M. F. Dolan, P. Buhl-Mortensen, and V. K. Bellec, *An evaluation of compiled single-beam bathymetry data as a basis for regional sediment and biotope mapping,* ICES Journal of Marine Science **71**, 867 (2014).

[64] H. von Nordheim and K. Wollny-Goerke, *Progress in marine conservation in Europe 2015,* (2015).

[65] C. Propp, A. Bartholomä, C. Hass, P. Holler, M. Lambers-Huesmann, S. Papenmeier, P. Richter, K. Schwarzer, F. Tauber, and M. Zeiler, *Guideline for Seafloor Mapping in German Marine Waters Using High-Resolution Sonars.*, BSH (2016).

[66] A.-C. Wölfl, H. Snaith, S. Amirebrahimi, C. W. Devey, B. Dorschel, V. Ferrini, V. A. I. Huvenne, M. Jakobsson, J. Jencks, G. Johnston, G. Lamarche, L. Mayer, D. Millar, T. H. Pedersen, K. Picard, A. Reitz, T. Schmitt, M. Visbeck, P. Weatherall, and R. Wigley, *Seafloor mapping – the challenge of a truly global ocean bathymetry,* Frontiers in Marine Science **6**, 283 (2019).

[67] EMODnet, *EMODnet geology,* Online (2020).

[68] V. van Lancker, *Transnational and integrated long-term marine exploitation strategies,* (2017).

[69] H. Heyer and K. Schrottke, *Aufbau von integrierten Modellsystemen zur Analyse der langfristigen Morphodynamik in der Deutschen Bucht,* Online (2012).

6

Bringing different sampling methodologies together

> *If you want to lift yourself up, lift up someone else.*
>
> Booker T. Washington

> *If I have seen further, it is by standing on the shoulders of giants.*
>
> Isaac Newton

DISCLOSE is a multi-disciplinary project, of which acoustic measurements are one part. The other parts use video and grab sample methods to study the seafloor. In this chapter we link acoustic results to the work and results produced in the rest of the project. The dataset comes from the Brown Bank where hydrodynamic forces from winds and tidal currents cause nested multiscale morphological features ranging from meter-scale (mega)ripples, to sand waves and kilometer-scale linear sandbanks. This multiscale habitat heterogeneity is generally disregarded in the ecological assessments of benthic habitats. In this chapter, we firstly discuss a novel approach to inverting multibeam echosounder backscatter data for sediment property parameters without the use of grab samples. Next, we consider a multiscale assessment toolbox that combines bathymetry, multibeam backscatter classification, video based surveying of epibenthos and box core grab samples of sediment and macrobenthos. We find that these methods are greatly complementary and allow for more detail in the interpretation of benthic surveys. Acoustic and video data characterized the seafloor surface and subsurface, and macrobenthos communities are found to be structured by both sandbank and sand wave topography. The results further indicate that acoustic techniques can be used to determine the location of epibenthic reefs.

Parts of this chapter have been published in Estuarine, Coastal and Shelf Science **238**, 106687 (2020) [1], Geosciences **9** (7), 292 (2019) [2], and Journal of Sea Research **144**, 85 - 94 (2019) [3].

6.1. Introduction

Within the DISCLOSE project a significant portion of the research focused on the Brown Bank area. Much of the research did not focus on the acoustics but on the benthic component. As such, the results presented in this chapter should be placed in that context. The Brown Bank area is referred to as a soft-sediment subtidal area. Subtidal, soft-sediment beds form the most widespread benthic habitat type on earth and result from the interplay of geological, physical and biological drivers [4, 5]. When occurring within the depth range affected by hydrodynamic activity from wind and currents (e.g. < 50 m deep on coastal shelves), these sediment beds typically form clear, multiscale nested structures, such as sandbanks, sand waves, or (mega)ripples [6, 7]. Consequently, heterogeneous seafloor landscapes are created, in which topographic features shape soft-sediment habitat diversity with respect to hydrodynamic exposure. This impact of topography on habitat heterogeneity is additionally complemented by variations in the physico-chemical composition of the sediment. In a sandbank system, for example, a clear spatial sediment distribution can be distinguished, with generally finer and carbonate-poorer sediments in the troughs than on the crest [8, 9]. Habitat variation resulting from this physico-chemical heterogeneity of the seafloor creates important variation in habitat conditions for benthic fauna. Spatial heterogeneity therefore influences important ecosystem features at various scales, including species diversity, density and biomass, community composition, and several ecosystem processes [10, 11]. In marine ecosystems, for example, macrobenthic communities tend to be richer, denser, and different in species composition in troughs than on crests of sandbanks [12], but also of sand wave crests [13] and small-scale ripples [14].

In terms of biodiversity, underlying gradients in the physical habitat template can be greatly amplified by biological mechanisms. Especially where the so called, 'ecosystem engineers' are present [15]. Ecosystem engineers are organisms that modify their physical habitat. Such biogenic landscape boundaries are well known from coral reefs, but also from intertidal habitats where several autogenic ecosystem engineers form complex three-dimensional structures, e.g. at the boundary of vegetated and non-vegetated tidal flats or seagrass meadows [16, 17], or in the vicinity of oyster reefs and other bivalve beds [18, 19]. Through density-dependent feedbacks, ecosystem engineers can buffer the impact of physical forces, although their occurrence is generally limited in locations where these physical forces exceed critical thresholds. In heavily trawled subtidal soft-sediment areas with high substrate mobility, such as sand wave-dominated sediments, their presence seems limited but not absent [20]. Some reef-forming organisms, such as tube worms, may occur in sandbank troughs, where food and suspended sediment needed to build their tubes are sufficiently present [3, 21]. The presence of these reefs induces high local biodiversity, sustained by increased local habitat heterogeneity, physical shelter and better food supply [22–24].

Anthropogenic physical disturbance, e.g. bottom trawl fisheries, tends to homogenise soft-bottom sediments by removing smaller-scale habitat heterogeneity in subtidal soft sediments, jeopardising their structure, function and biodiversity [25, 26]. Epibenthos is particularly vulnerable to this influence [3, 27], but infaunal organisms are also affected, resulting in a shift of benthic communities towards a dominance of shorter-lived species [28, 29]. Given the high prevalence and intensity of demersal fisheries in shallow coastal seas such as the North Sea [30–32], benthic surveys may not be sufficiently able to reveal the biodiversity potential of many benthic (sub)habitats created by the interplay between hydrodynamic and biological forces. An approach that resolves the underlying physical gradients and evaluates both the potential of this template for biogenic self-reinforcing biodiversity development, and vulnerability/sensitivity to disturbance, is therefore needed.

The most important constraint for biodiversity-oriented benthic surveys is the trade-off between extent and grain[1] of the different observational methods. As sampling is often costly and time-consuming, and areas needing coverage are large, a balance between extent and resolution needs to be found [33, 34]. With respect to the identification of the physical habitat template, a very promising approach is the use of multibeam echo-sounding (MBES). Especially when the full information in the returning acoustic signals (including backscatter intensity) is used, this acoustic technique allows for a detailed characterization of the seafloor bathymetry, but can also give information about the sediment type variation of the seafloor as seen in the previous chapters [35, 36]. However, the method does not give direct information to link the topography and acoustic classes to the species composition of benthic assemblages [37]. In situ sampling remains necessary to link topography to seafloor ecology. To map seafloor communities, multibeam data can be combined with camera surveying, such as video transects, photos of the seafloor by landing frames or Sediment Profile Imaging i.e. SPI camera (Section 6.3.3). Between these techniques, there is also a trade-off between the area covered per unit effort, and taxonomic resolution of the biodiversity surveys. An optimal combination of several techniques is likely the best compromise between these approaches.

Within the DISCLOSE project it was tested how MBES, video, photographic (SPI) and box core sampling data of the seafloor can be combined to accurately link biodiversity to seafloor morphology. It was also explored if this allows locally sampled biodiversity patterns to be interpolated and extrapolated to the wider seafloor landscape. Since different seafloor morphologies can offer different substrate characteristics and varying food availability to the benthic fauna, the relationships between benthic macrofauna abundance, biodiversity, and sediment grain size and organic matter quantity and biochemical composition were also explored. Additionally, an inversion method to obtain three sediment parameters from backscatter is presented and used to quantify the correlation between the outcomes of the different approaches of DISCLOSE and to generalize this information in the design of optimal survey approaches for larger areas of the North Sea.

6.2. The Brown Bank study area

The Brown Bank study area considered in this chapter is also described in Section 3.2.1. A summary description of the area, including some of the outcomes

---

[1] Grain refers to the resolution in space and time, and in terms of variables estimated of an observational method.

mentioned earlier in this thesis, follows. At the Brown Bank there is a large sandbank with a height difference of about 26 m between crest and trough, belonging to the north-south oriented Dutch Banks in the southern North Sea (Figure 6.1). The sandbank is located nearly halfway between the Netherlands and the United Kingdom, at about 85 km from the Dutch coast. The seafloor in this region additionally forms smaller-scale sand waves that are roughly east-west oriented, with wavelengths of about 200 m and heights of 2 m, and smaller megaripples, with wavelengths and heights of about 10 m and 0.5 m respectively. The even smaller sand ripples discussed in Chapter 4 are not considered in this chapter. Both sand waves and megaripples migrate over the seafloor, at rates in the order of several meters per year for sand waves and within weeks or even hours for megaripples [38–40]. The area is heavily fished by bottom trawlers, especially the troughs between the large sandbanks [32]. The sampling took place from 26 October till 5 November 2017, during a campaign on board RV Pelagia.

6.3. Materials and methods

6.3.1. Multibeam echosounding, classification based on the full angular response

In this section we present a method that was also used in [2]. This method is important because it provides further information from the MBES measurements, separating the contribution of roughness and volume scattering. The observed backscatter strength of MBESs is a function of the signal frequency, grazing angle, and sediment type. The angular dependence of the received backscatter data in combination with an established seafloor interaction model allows for an inversion to estimate the geoacoustic parameters. There is one complication; the fact that there is often no good calibration of the sonar systems with respect to backscatter strength. Amiri-Simkooei *et al.* [2] proposes an innovative calibration method that does not rely on the use of grab samples. The full method thus consists of three steps. Firstly, a calibration curve, together with the sediment parameters mean grain size (M_z), volume scattering (σ_2), and spectral strength (w_2) are estimated per Bayes class, see Section 3.3.1. In [2] the validity of this calibration approach is assessed by using different sets of measurements. It was found that the estimated calibration curve is independent of the set used, providing further validation of the method. Second, the backscatter data is corrected by use of the estimated calibration curve. Thirdly, the corrected backscatter is utilized to estimate the sediment parameters M_z, σ_2, and w_2 for the full area. To have a better spatial resolution, this process is implemented for the port ($-65^\circ \leq \theta \leq 0^\circ$) and starboard ($0^\circ \leq \theta \leq 65^\circ$) sides of the sonar separately.

In addition to obtaining the geo-acoustic parameters just mentioned, the bathymetry was used to calculate slope and the Bathymetric Position Index (BPI) (Section 5.2.1). We used BPI$_{2000}$ (with a 2000 m radius) as a measure for sandbank topography, BPI$_{200}$ for sand waves and BPI$_{10}$ for megaripples. All of these features were used to search for the best MBES based output to link to macrofauna data.

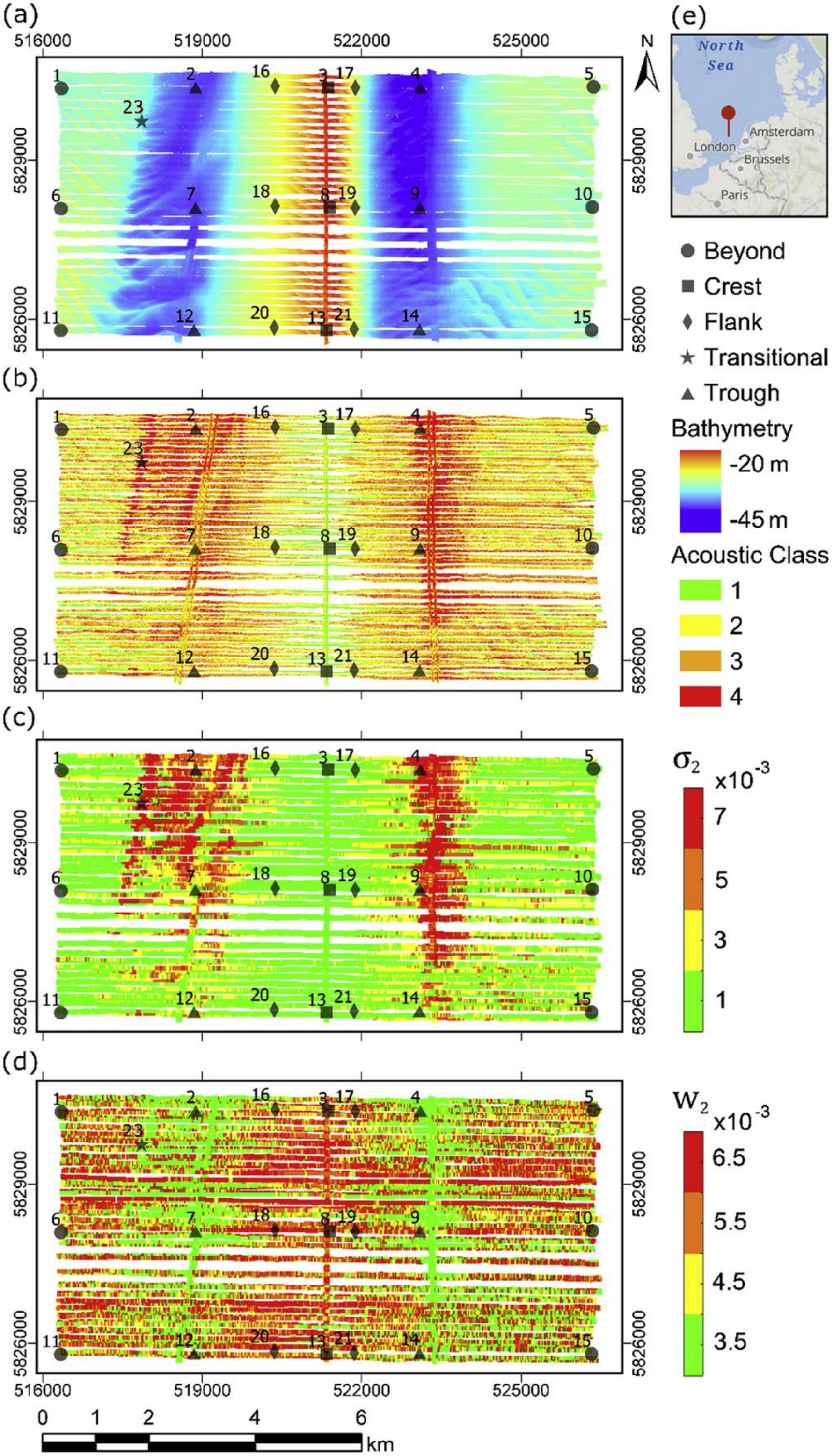

Figure 6.1: Location of the 22 sampling stations on and around the Brown Bank, with background colour indicating (**a**) bathymetry, (**b**) backscatter-based acoustic classes, (**c**) volume scattering (σ_2) and (**d**) surface roughness (w_2). The inset (**e**) shows the location of the Brown Bank in the southern North Sea.

6.3.2. Box core samples

The locations and grain size analysis of the 22 grab samples used in this chapter have been previously described in Section 3.2.4. The sampled stations were further classified according to their topographic position (TP):

- Crest
- Flank
- Trough
- Transitional
- Beyond

relative to the Brown Bank. At each station, three replicate box core samples were taken with a box corer (30 cm internal diameter).

In addition to the grab sample locations relative to the Brown Bank, the samples gathered in sand wave areas were also categorized according their position in a sand wave. Within these samples three stations were located in a sand wave trough (stations 1, 10 and 15) and one (station 5) on a crest. A further two stations were located on the stossside flank (stations 6 and 11).

In addition to the grain size analysis, which was described in a previous section (Section 3.2.4), the chemical and macrobenthic information was also determined and is now described. After extraction in a bullet blender with 90% acetone, chlorophyll *a* was analyzed using a Specord 210 spectrophotometer (Analytik Jena, Jena, Germany). Total organic carbon (TOC) and total nitrogen (TN) were analyzed according to the Dumas method [41], using a Thermo Flash 2000 Element Analyzer (Thermo Fisher Scientific, Waltham, Massachusetts, USA).

The grab samples were further sieved over a 0.5 mm mesh to extract the macrobenthos (organisms large enough to be caught in the 0.5 mm sieve). Animals were fixed in 4–6% formalin and transported to the laboratory, where they were counted and identified to the lowest possible taxonomic level. For each sample, densities, species richness (S) and Pielou's evenness (J') were calculated. Pielou's evenness indicates how comparable the number of individuals per species is between the various species. Furthermore, functional groups were defined based on combinations of sediment reworking mode as follows:

- E: epifauna
- S: surficial modifiers
- C: conveyor-belt feeders
- B: biodiffusors
- R: regenerators,

and motility, how easily they can move, in the sediment [42, 43] as follows

- A: in a fixed tube
- B: sessile, but not in a tube
- C: slow movement through the sediment
- D: free movement through a burrow system.

6.3.3. Sediment profile imaging

Another observation system, not previously used in this thesis, is the Sediment Profile Imaging (SPI) camera. It was used at the Brown Bank to determine the subsurface seabed structure. The SPI consists of a galvanized frame with a camera-comprising prism, which penetrates the seafloor when lowered onto the seabed [44]. The SPI was lowered three times at each station, except at Station 23. At each drop, two pictures were taken, resulting in 6 pictures per station. The penetration depth was measured and the presence of shell fragments was classified as follows

- 0: no shell fragments
- 1: few shell fragments
- 2: medium shell fragments
- 3: many shell fragments,

and the dominant sediment type was identified (Sand or Mud).

6.3.4. Video transects

An important sensor within DISCLOSE is the optical camera, as previously used and described in Sections 3.2.3 and 4.2.3. Within DISCLOSE a dedicated optical camera system, called Bruce, was developed. In addition to Bruce an additional drop camera from NIOZ was also used. The optical camera is key to bridge the gap between the large-scale MBES, providing a proxy for the habitat, and the very detailed grab sample that covers a very limited area. Additionally, videos of the seafloor are perhaps the most intuitive method to perceive a habitat type.

Video transects were performed at 10 stations, on the crest and in both troughs of the Brown Bank, as well as for the transitional station (Station 23, Figure 6.1). Two transects were performed for each station except the transitional station. Validity and superficial landscape type were deduced from the video footage, as well as shifts between landscape types and the number of observed organisms. The observed species were identified to the lowest taxonomic level possible. For each transect, the surveyed area was defined as the summed surface of grid cells, of size 0.5×0.5 m, that the camera traversed. The number of individuals of each species could hence be converted to densities (m^2) per transect. The number of switches in landscape type was determined as an indicator of small-scale habitat heterogeneity. For this, the number of landscape switches was divided by the length of the transect, which was determined as the sum of distances between valid recordings.

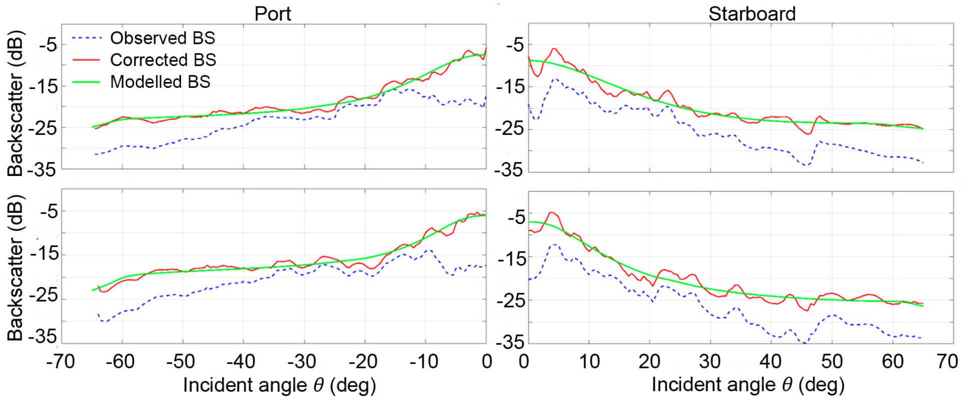

Figure 6.2: Two typical examples of the optimization problem in which three geoacoustic parameters were searched for, Port side (left), Starboard side (right). Indicated in plots are observed backscatter curve (dashed blue line), corrected backscatter curve after applying calibration curve (solid red line), and modeled backscatter curve (solid green line).

6.4. Results of DISCLOSE measurement methods

6.4.1. Acoustic characterization of the seafloor

The procedure described in Section 6.3.1 is now implemented to estimate the backscatter calibration curve. Then the inversion is performed for the three geoacoustic parameters M_z, w_2, and σ_2 for each measured backscatter curve. As stated before, this is done separately for the port and the starboard sides. The unknown parameters were constrained as $-1 \leq M_z \leq 9, 0.001 \leq w_2 \leq 0.01$, and $0.0001 \leq \sigma_2 \leq 0.02$. Figure 6.2 shows two typical mean backscatter curves for which the geoacoustic inversion was applied to estimate M_z, w_2, and σ_2. Also shown are the observed BS curves (dashed lines). The difference between the corrected and observed backscatter curves represents the calibration curve. The modeled BS curves are seen to closely follow the corrected backscatter curves after the optimization method was applied.

The inverted geoacoustic parameters are presented in Figure 6.1 (M_z is not shown), and smoothed full coverage maps of all three parameters are shown in Figure 6.3. The mean grain sizes mainly range from 1 - 2.5 ϕ with the dominant values in the range of 1.5 - 2 ϕ. This is in agreement with the grab samples collected in this survey area. The estimated mean grain sizes show high spatial variability, which may indicate that the survey area has an almost non-distinctive and heterogeneous sedimentary composition. However, the parameters w_2 and σ_2 (Figure 6.3 middle and bottom) show clear spatial patterns.

6.4.2. Importance of inverting the MBES data for three parameters

For the inversion method, the results indicate that a search for at least three geoacoustic parameters is required. Empirical models relate the roughness parameter

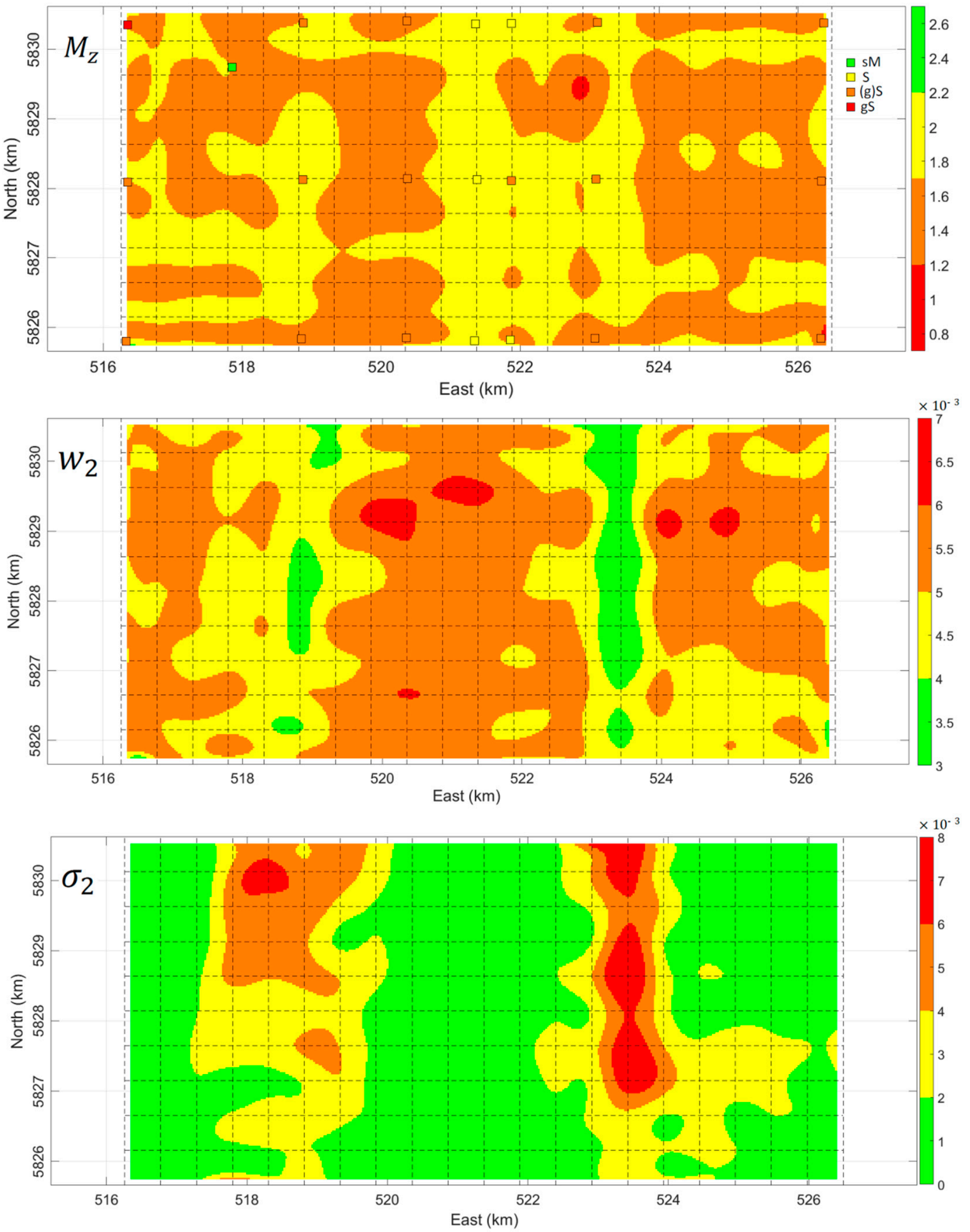

Figure 6.3: Smoothed maps of inverted mean grain size M_z (top), spectral strength w_2 (middle), and volume scattering parameters σ_2 (bottom). Also indicated in the top frame are the mean grain sizes of the grab samples based on the Folk classification scheme. Dashed lines indicates square patches connected to each other using the LS-BICSA method [45].

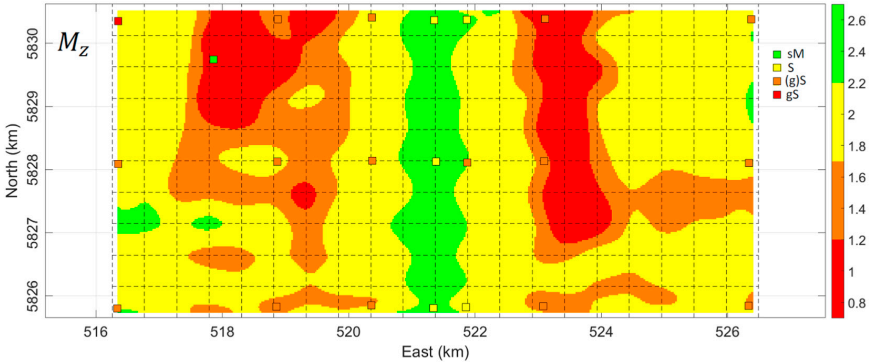

Figure 6.4: Smoothed maps of inverted mean grain size M_z along with Folk classes of grab samples when spectral strength w_2 and volume scattering parameter σ_2 were kept fixed to their average values.

w_2 and the volume scattering parameter σ_2, to the mean grain size M_z [46]. These relations are known to be rather weak, as there is a considerable range of variations in these two parameters and hence they are not much correlated with M_z [47]. Therefore, the optimization was performed by using the three parameters M_z, w_2 and σ_2.

To further elaborate on this issue, the optimization method was implemented only for the mean grain size, while keeping w_2 and σ_2 fixed to their average values or to those predicted by the empirical model of [46]. We thus search only for M_z values in the optimization method. The estimated M_z values are presented in Figure 6.4. As indicated, the range of M_z variations has been significantly increased compared to the results presented in Figure 6.3 (significant green areas having $M_z \simeq 2.5$ and red areas having $M_z \simeq 1$ appeared), which cannot be justified based on the grab samples taken. These areas indeed correspond to those having smallest and largest σ_2, respectively, and to some extent having largest and smallest w_2 values. Ignoring these two independent geoacoustic parameters in the inversion may thus cause an overestimated or underestimated mean grain size.

6.4.3. Grab sample results

Abiotic properties of the sandbank sediments

In the following, a parameter denoted topographic position (TP) (see Section 6.3.2) is used. When analyzing the grab-sample data the main idea is to investigate weather the grabs show differences between the major topographic regions. The total organic carbon (TOC) differed significantly between nearly all TPs. Among these, the ‘Flank’ was similar to the ‘Beyond’, and the ‘Trough’ was similar to the ‘Transitional’ TP. The TOC was highest in the ‘Transitional’ (0.59 ± 0.19)%[2] and lowest on the ‘Crest’ $(1.2 \pm 0.3) \times 10^{-2}$%. The total nitrogen (TN) values were significantly different between the ‘Transitional’ and other TPs, and between

---

[2] values are represented as (mean ± standard deviation)

the 'Trough' and other TPs, but not between 'Transitional' and 'Trough'. Values were lowest on the 'Crest' $(4.7 \pm 3.2) \times 10^{-3}$% and highest in the 'Transitional' $(6.1 \pm 1.4) \times 10^{-2}$%. Chlorophyll *a* content showed significant patterns, with highest values in the 'Trough' $(0.5 \pm 0.3 \mu g/g)$ and lowest on the 'Crest' $(0.1 \pm 0.02 \mu g/g)$.

With respect to the sediment properties within the sand waves only chlorophyll *a* content was found to be significantly different between the flanks and troughs. Higher values were found in the troughs than on the flanks.

Biotic results of the grab sample analysis

All variables concerning macrobenthos density and diversity were analyzed, again aiming to relate them to the five TPs. The methods were performed in the open source statistical software *R* [48], are described in detail in [1], and not repeated here.

Total densities were lowest on the 'Crest' (380.40 ± 224.52 individuals/m^2) and highest in the 'Trough' and 'Transitional' (2092.99 ± 2834.49 and 1872.13 ± 1092.39 individuals/m^2, respectively) TPs. Densities on the 'Crest' were significantly lower than all other TPs and densities in the 'Trough' significantly higher than all others except the 'Transitional'. The species richness was lowest with 9.44 ± 3.50 species per sample on the 'Crest' and highest with 28 ± 9.54 species in the 'Transitional', and showed significant differences between all TPs, except between the 'Flank' and 'Beyond' and between the 'Trough' and the 'Transitional'. Pielou's evenness ranged from 0.79 ± 0.08 in the 'Trough' to 0.84 ± 0.09 on the 'Crest' and did not differ significantly among TPs.

When investigating if species patterns were similarly effected by sand wave topology as sand bank topology, it was found that the species richness, but not Pielou's evenness, was significantly different between sand wave crests and troughs. In general, our results indicate that total densities and species richness vary with the large-scale morphology. The same pattern, albeit less pronounced, holds for the smaller scale sand wave morphology.

6.4.4. Subsurface seabed structure

The penetration depth for the SPI pictures was tested using a linear mixed model (LMM), with topographic position as explanatory and station as random variable. The log likelihood ratio was determined between this model and a null model with only the random effect of station included. The average penetration depth was 6.3 ± 2.9 cm, with 39 pictures having a penetration depth of < 5 cm. Penetration depth was much larger on the crest (11.5 ± 2.9 cm) than at the other locations (5.6 ± 2.1 cm) (log likelihood ratio of LMM: -6.8).

In addition to the penetration depth, the images were also classified according to the sediment. From this, the main insight from the SPI data is that the amount of shell fragments was higher in the troughs compared to the crest locations. The crest pictures were all classified as no shell fragments (class 0), while the trough pictures showed the highest percentages of class 1 and 2 (medium and many shell fragments, respectively).

6.4.5. Video transects

For the video transects species types were identified, counted, and linked to TPs. In addition, it was noted if the habitat type changed significantly in the course of a video transect. A total of 1813 individuals of 16 species were observed, over a total observed area of 1358 m^2. The most recorded species was the starfish Asterias rubens (1378 individuals), followed by Ophiuroidea brittle stars (256 individuals) and the hermit crab Pagurus bernhardus (65 individuals). Compared to the crest (0.128 ± 0.057), the troughs (East: 3.079 ± 4.502; West: 0.770 ± 0.298) had higher densities of organisms (log likelihood ratio LMM: -4.9). Moreover, the troughs (East: 3.463 ± 2.876; West: 5.315 ± 3.183) showed 3 to 5 habitat type changes per 100 m transect, while the crest showed none (log likelihood ratio LMM: -4.9). Crest transects only showed sandy sediment with hardly any shell fragments, while all other stations alternated between sandy sediments with shell fragments and sandy sediments with shell fragments and incidental large stones. Sandy sediments with shell fragments, incidental stones and Sabellaria reef fragments (Sabellaria landscape) were observed in the northern station in the eastern trough (station 4) and the middle station in the western trough (station 7). Moreover, the transitional station (station 23) showed some Sabellaria habitat, but also the unique "sand with clay" and "sand with clay and incidental stones" habitats.

6.5. Integration of the different DISCLOSE methods

The video footage, SPI images, and MBES data show similar features, with the more topographically diverse seafloor habitats outside the sandbank crest corresponding with a higher backscatter signal. To link the results from the different sampling methods, a redundancy analysis (RDA) was performed [49]. RDA can be considered a constrained version of Principal Component Analysis (PCA), where it is desired to find linear relationships between a set of dependent variables that are influenced by a set of independent variables. As such, a linear regression is first performed to explain the dependent variables as a function of the independent variables and PCA is then performed on these results to select only those independent variables that best explain the dependent variables [50]. For this research the following were chosen to be the independent variables: M_z, w_2, σ_2, slope, backscatter, bathymetry, BPI_{2000}, BPI_{200}, BPI_{10}, TOC, TN and chlorophyll *a* content. All variables were linearized prior to the RDA analysis. The model explained 46.7% of the total variation in the macrobenthic data. Bathymetry mostly separated the macrobenthos communities in the different topographic positions from each other, as well as sand wave flanks/crests from the sand wave troughs in the 'Beyond' TP. TOC and σ_2 separated the 'transitional' and the trough stations with Sabellaria from the rest of the sampling stations. When the RDA model was based on functional groups, then σ_2 and backscatter were selected as significant contributors to the variation in community structure. These variables separated the 'Trough', 'Transitional', and stations in sand wave troughs in the 'Beyond' region from the rest of the stations. This model explained 31.1% of the total variation in the data.

The observation of stones and shell fragments in the troughs matches between the video footage and SPI photographs. These are further found to coincide with higher backscatter values [40, 51], specifically volume scattering. The resulting mixed sediment beds explain the higher volume scattering observed in the sandbank troughs.

Macrobenthic community compositions appear to be largely determined by topographic position (as determined by hydrodynamics), with higher biodiversity in the sandbank troughs than on the crest, confirming earlier research [12, 52]. Furthermore, in the sand wave regions in the 'beyond' TP it was found that the grab samples from the sand wave troughs were more similar to the samples from the trough of the tidal ridge. The samples from the sand wave crest were more similar to the samples from the crest of the tidal ridge. This pattern was evident despite the samples from the sand waves being poorly distributed relative to the crests, troughs, and flanks of the sand waves. The higher biodiversity in troughs of different scales has been associated with a higher organic matter or mud content [12–14]. However, our communities from the sand wave-dominated areas were hardly separated based on their organic matter content, and we could only find this distinction in sediment properties for the large-scale sandbank. We therefore suggest that, next to sediment properties, physical stress caused by the dynamics of water and sediment is an important factor in determining which species will dominate communities in sand wave environments.

6.5.1. Implications for monitoring

By combining different sampling methods, we obtained a more detailed image of the seafloor than would otherwise be possible. Traditional designs that merely focus on grab or box core samples do not take small-scale heterogeneity of the seafloor into account and interpolate the findings of sampling points to their direct surroundings. Great care should therefore be taken in the spatial interpolation between samples. Although macrobenthos communities largely corresponded with the Brown Bank topology, we showed that additional techniques are useful to obtain information about smaller-scale variability. Acoustic data were crucial to identify sand waves, allowing us to compare patterns in community structure on the sandbank and the sand wave scale. Furthermore, video footage revealed that the Sabellaria found in the box core samples formed (fragmented) reefs, which occurred only in areas with high volume scattering. Not only can we therefore use these techniques to add detail to our interpretation of seafloor heterogeneity, they may also be useful to delineate regions where biogenic structures can be present, and therefore potentially serve as an important tool in conservation management. The box core samples, in contrast with the other survey techniques, allowed inferring the correlation structure between the occurrence of all species of macrobenthos. This is needed in order to properly evaluate the community effects of features like Sabellaria reefs.

6.5.2. Sabellaria reefs and the impact of bottom trawling

In the DISCLOSE project Sabellaria spinulosa reefs were discovered in the area of the Brown Bank during a cruise with OCEANA [3] (Figure 6.5). Sabellaria spinulosa is considered an important species because it is an ecosystem engineer. Related to the presence of this species, the analysis of the video and box core data did

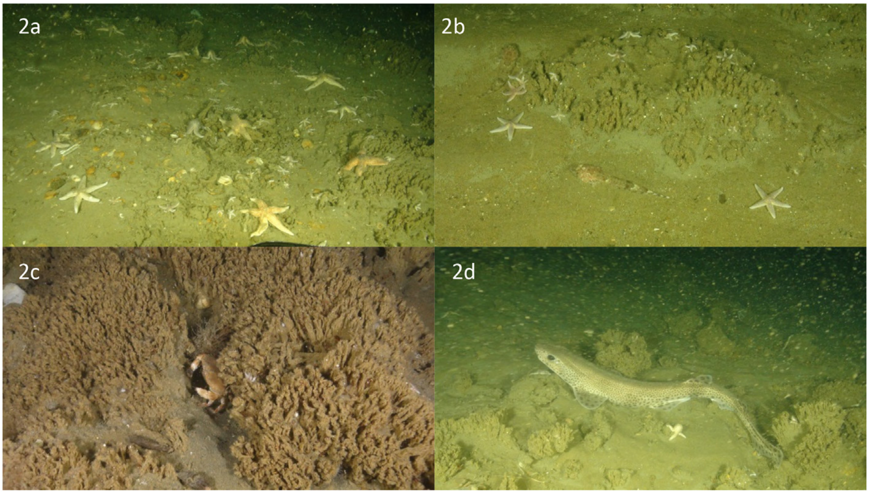

Figure 6.5: Pictures of the S. spinulosa reefs in low abundance (a,b) and reef structure (c,d), with associated species (a: Common starfish (Asterias rubens); b: Common starfish (A. rubens) and dragonets (Callionymus spp.); c: Edible crab (Cancer pagurus); d: Small-spotted catshark (Scyliorhinus canicula)).

not always lead to the same conclusions. At the transitional station, high abundances of individual Sabellaria worms were found in the box cores, whereas the video showed only few reef fragments. Likewise, in the northernmost station in the western trough one box core sample contained Sabellaria worms, but no reef fragments were observed in the video transects. For the northernmost station in the eastern trough and the central station in the western trough, video observations of Sabellaria reef fragments did not automatically coincide with frequent presence of Sabellaria worms in the box core samples. This indicates that this species has a larger distribution area, but forms reefs (Figure 6.5) only in specific locations, and its patchy distribution demands a sampling approach covering multiple scales. Our samples suggest that the presence of both Sabellaria reefs and individuals stimulates the establishment of diverse and – both taxonomically and functionally – distinct macrobenthos communities. Earlier studies have emphasized the ecological importance of reef-forming benthic species, especially through promoting habitat heterogeneity and organic matter entrapment [22, 23, 53]. Interestingly, we show that high abundances of Sabellaria individuals might have the same effect. Furthermore, the specific locations where reef fragments were observed appeared to occur in areas characterized by high acoustic volume scattering, suggesting that this parameter can be used to identify potential Sabellaria reef locations.

The presence of Sabellaria reefs and more diverse and dense macrobenthos communities in the Brown Bank troughs can promote a higher fish diversity, since several species of demersal[3] fish are known to feed near these reefs [54]. Van der

---

[3] Demersal fish are those that live close to the seafloor. The so called demersal zone is in the water column but so close to the seafloor that it is significantly affected by the seafloor and the benthos. The demersal zone is just above the benthic zone. The benthic zone refers to the ecological region on the

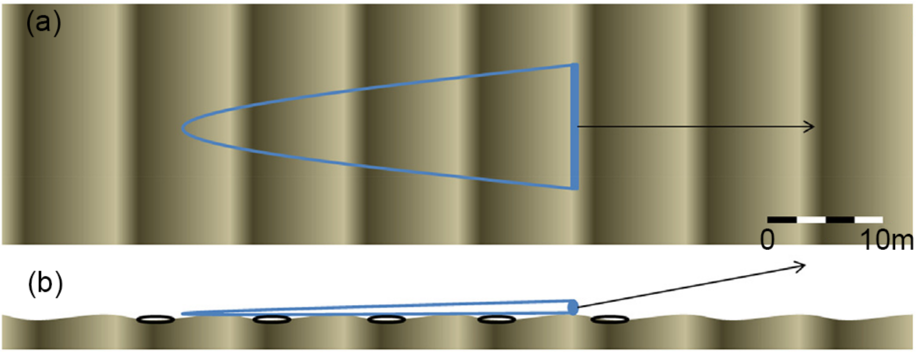

Figure 6.6: A simulation of the seabed topography in relation to fishing activities. The top view (a) shows a beam trawl net (blue). The small-scale megaripples (shown by a light top and dark valley) are perpendicular to the main fishing direction. The side view (b) shows a cross-section of the seabed with the megaripples and the potential refuge areas (black ovals) in the troughs.

Reijden *et al.* [32] showed that beam trawl fisheries strongly prefer the Brown Bank troughs, resulting in intense local fishing. Beam trawling is known to destroy epibenthic structures such as reefs and disrupt endobenthic communities by dragging heavy gear over the seafloor [55, 56]. This intense trawling is therefore a likely reason why only sparse reefs are known around the Brown Bank, whereas higher amounts of reefs still occur in British waters, where they have enjoyed a longer protection [3, 57]. The macrobenthos communities of the Brown Bank troughs are probably adapted to high disturbance, as the region has already been trawled since the thirteenth, and more intensively since the middle of the twentieth century [58, 59]. As the communities are either influenced by anthropogenic disturbance (bottom trawling in the troughs and lower flanks) or by a higher physical stress (high hydrodynamic regime on the crests and higher parts of the sandbank), their current functional composition lacks a clear distinction. Given these considerations, we hypothesize that the Sabellaria reefs survive at the Brown Bank by being located in the troughs of mega ripples (Figure 6.6). These troughs likely form refuge areas where they are spared the full-weight heavy fishing gear.

6.6. Conclusion

The combined use of multiple sampling techniques for seafloor and benthos characterisation allowed us to make a detailed interpretation of our findings. As standard sampling schemes tend to inadvertently 'homogenise' the studied region when spatially extrapolating data, we recommend the complementary use of the MBES, video footage, SPI imagery, together with grab sampling. This allows for a greater detail of the surveys, allowing predictions about the interlaying seafloor characteristics that can potentially serve for conservation management.

---

sediment surface and some sub-surface layers.

6.7. Acknowledgments

The authors would like to thank Karline Soetaert (NIOZ) for organizing the NIOZ cruise and acknowledge Rob Witbaard (NIOZ) for his role as chief scientist during the cruise. The crew of RV Pelagia is also acknowledged for their practical assistance on board. Peter van Breugel is thanked for performing the particle size analysis in the NIOZ lab, and Matthew Parsons and Maria Bacelar Martinez for processing of the macrobenthos samples. Finally, the authors acknowledge the Gieskes-Strijbis Fonds for financial support of the DISCLOSE project, within which this research took place.

References

[1] S. Mestdagh, A. Amiri-Simkooei, K. J. van der Reijden, L. Koop, S. O'Flynn, M. Snellen, C. Van Sluis, L. L. Govers, D. G. Simons, P. M. Herman, H. Olff, and T. Ysebaert, *Linking the morphology and ecology of subtidal soft-bottom marine benthic habitats: A novel multiscale approach,* Estuarine, Coastal and Shelf Science **238**, 106687 (2020).

[2] A. R. Amiri-Simkooei, L. Koop, K. J. van der Reijden, M. Snellen, and D. G. Simons, *Seafloor characterization using multibeam echosounder backscatter data: methodology and results in the North Sea,* Geosciences **9**, 292 (2019).

[3] K. J. Van Der Reijden, L. Koop, S. O'flynn, S. Garcia, O. Bos, C. Van Sluis, D. J. Maaholm, P. M. Herman, D. G. Simons, and H. Olff, *Discovery of sabellaria spinulosa reefs in an intensively fished area of the Dutch continental shelf, North Sea,* Journal of Sea Research **144**, 85 (2019).

[4] P. V. Snelgrove, *Getting to the bottom of marine biodiversity: sedimentary habitats: ocean bottoms are the most widespread habitat on earth and support high biodiversity and key ecosystem services,* BioScience **49**, 129 (1999).

[5] M. Zeiler, K. Schwarter, K. Ricklefs, and A. Bartholomä, *Seabed morphology and sediment dynamics,* Die Küste, 74 ICCE , 31 (2008).

[6] A. Mazières, H. Gillet, D. Idier, T. Mulder, T. Garlan, C. Mallet, V. Marieu, and V. Hanquiez, *Dynamics of inner-shelf, multi-scale bedforms off the south aquitaine coast over three decades (southeast bay of biscay, france),* Continental Shelf Research **92**, 23 (2015).

[7] S. Passchier and M. Kleinhans, *Observations of sand waves, megaripples, and hummocks in the Dutch coastal area and their relation to currents and combined flow conditions,* Journal of Geophysical Research: Earth Surface **110** (2005).

[8] A. Heathershaw and J. Codd, *Depth-controlled changes in grain size and carbonate content on a shelf-edge sand bank,* Marine geology **72**, 211 (1986).

[9] A. Trentesaux, A. Stolk, B. Tessier, and H. Chamley, *Surficial sedimentology of the middelkerke bank (southern North Sea),* Marine Geology **121**, 43 (1994).

[10] J. A. García-Charton, A. Pérez-Ruzafa, P. Sánchez-Jerez, J. Bayle-Sempere, O. Reñones, and D. Moreno, *Multi-scale spatial heterogeneity, habitat structure, and the effect of marine reserves on western mediterranean rocky reef fish assemblages,* Marine Biology **144**, 161 (2004).

[11] G. M. Lovett, C. G. Jones, M. G. Turner, and K. C. Weathers, *Ecosystem function in heterogeneous landscapes,* in *Ecosystem function in heterogeneous landscapes* (Springer, 2005) pp. 1–4.

[12] T. A. van Dijk, J. A. van Dalfsen, V. Van Lancker, R. A. van Overmeeren, S. van Heteren, and P. J. Doornenbal, *Benthic habitat variations over tidal ridges, North Sea, the Netherlands,* in *Seafloor Geomorphology as Benthic Habitat* (Elsevier, 2012) pp. 241–249.

[13] J. H. Damveld, K. J. van der Reijden, C. Cheng, L. Koop, L. R. Haaksma, C. A. J. Walsh, K. Soetaert, B. W. Borsje, L. L. Govers, P. C. Roos, H. Olff, and S. J. M. H. Hulscher, *Video transects reveal that tidal sand waves affect the spatial distribution of benthic organisms and sand ripples,* Geophysical Research Letters **45**, 11,837 (2018), https://agupubs.onlinelibrary.wiley.com/doi/pdf/10.1029/2018GL079858 .

[14] P. A. Ramey, J. P. Grassle, J. F. Grassle, and R. F. Petrecca, *Small-scale, patchy distributions of infauna in hydrodynamically mobile continental shelf sands: Do ripple crests and troughs support different communities?* Continental Shelf Research **29**, 2222 (2009).

[15] C. G. Jones, J. H. Lawton, and M. Shachak, *Organisms as ecosystem engineers,* Oikos **69**, 373 (1994).

[16] E. W. Koch, J. D. Ackerman, J. Verduin, and M. van Keulen, *Fluid dynamics in seagrass ecology—from molecules to ecosystems,* in *Seagrasses: biology, ecologyand conservation* (Springer, 2007) pp. 193–225.

[17] S. Temmerman, T. J. Bouma, G. Govers, Z. B. Wang, M. De Vries, and P. Herman, *Impact of vegetation on flow routing and sedimentation patterns: Three-dimensional modeling for a tidal marsh,* Journal of Geophysical Research: Earth Surface **110** (2005).

[18] E. M. van der Zee, T. van der Heide, S. Donadi, J. S. Eklöf, B. K. Eriksson, H. Olff, H. W. van der Veer, and T. Piersma, *Spatially extended habitat modification by intertidal reef-building bivalves has implications for consumer-resource interactions,* Ecosystems **15**, 664 (2012).

[19] B. Walles, J. S. De Paiva, B. C. van Prooijen, T. Ysebaert, and A. C. Smaal, *The ecosystem engineer crassostrea gigas affects tidal flat morphology beyond the boundary of their reef structures,* Estuaries and Coasts **38**, 941 (2015).

[20] J. Houziaux, F. Kerckhof, K. Degrendele, M. Roche, and A. Norro, *The hinder banks: yet an important region for the belgian marine biodiversity,* Brussels: Belgian Science Policy , 249 (2008).

[21] V. Van Lancker, G. Moerkerke, I. Du Four, E. Verfaillie, M. Rabaut, and S. Degraer, *14 - fine-scale geomorphological mapping of sandbank environments for the prediction of macrobenthic occurrences, belgian part of the North Sea,* in *Seafloor Geomorphology as Benthic Habitat*, edited by P. T. Harris and E. K. Baker (Elsevier, London, 2012) pp. 251 – 260.

[22] S. Dubois, C. Retière, and F. Olivier, *Biodiversity associated with sabellaria alveolata (polychaeta: Sabellariidae) reefs: effects of human disturbances,* Marine Biological Association of the United Kingdom. Journal of the Marine Biological Association of the United Kingdom **82**, 817 (2002).

[23] M. F. Gravina, F. Cardone, A. Bonifazi, M. S. Bertrandino, G. Chimienti, C. Longo, C. N. Marzano, M. Moretti, S. Lisco, V. Moretti, G. Corriero, and A. Giangrande, *Sabellaria spinulosa (polychaeta, annelida) reefs in the Mediterranean Sea: Habitat mapping, dynamics and associated fauna for conservation management,* Estuarine, Coastal and Shelf Science **200**, 248 (2018).

[24] M. Rabaut, K. Guilini, G. Van Hoey, M. Vincx, and S. Degraer, *A bio-engineered soft-bottom environment: The impact of lanice conchilega on the benthic species-specific densities and community structure,* Estuarine, Coastal and Shelf Science **75**, 525 (2007).

[25] R. A. McConnaughey, K. L. Mier, and C. B. Dew, *An examination of chronic trawling effects on soft-bottom benthos of the eastern Bering Sea,* ICES Journal of Marine Science **57**, 1377 (2000), https://academic.oup.com/icesjms/article-pdf/57/5/1377/1882024/57-5-1377.pdf .

[26] S. F. Thrush and P. K. Dayton, *Disturbance to marine benthic habitats by trawling and dredging: Implications for marine biodiversity,* Annual Review of Ecology and Systematics **33**, 449 (2002), https://doi.org/10.1146/annurev.ecolsys.33.010802.150515 .

[27] C. Jenkins, J. Eggleton, J. Albrecht, J. Barry, G. Duncan, N. Golding, and J. O'Connor, *North norfolk sandbank and saturn reef csac,* SCI Management Investigatio n Report (2015).

[28] A. D. Rijnsdorp, S. G. Bolam, C. Garcia, J. G. Hiddink, N. T. Hintzen, P. D. van Denderen, and T. van Kooten, *Estimating sensitivity of seabed habitats to disturbance by bottom trawling based on the longevity of benthic fauna,* Ecological Applications **28**, 1302 (2018).

[29] M. Sciberras, J. G. Hiddink, S. Jennings, C. L. Szostek, K. M. Hughes, B. Kneafsey, L. J. Clarke, N. Ellis, A. D. Rijnsdorp, R. A. McConnaughey, R. Hilborn, J. S. Collie, C. R. Pitcher, R. O. Amoroso, A. M. Parma, P. Suuronen, and M. J. Kaiser, *Response of benthic fauna to experimental bottom fishing: A global meta-analysis,* Fish and Fisheries **19**, 698 (2018), https://onlinelibrary.wiley.com/doi/pdf/10.1111/faf.12283 .

[30] R. O. Amoroso, C. R. Pitcher, A. D. Rijnsdorp, R. A. McConnaughey, A. M. Parma, P. Suuronen, O. R. Eigaard, F. Bastardie, N. T. Hintzen, F. Althaus, S. J. Baird, J. Black, L. Buhl-Mortensen, A. B. Campbell, R. Catarino, J. Collie, J. H. Cowan, D. Durholtz, N. Engstrom, T. P. Fairweather, H. O. Fock, R. Ford, P. A. Gálvez, H. Gerritsen, M. E. Góngora, J. A. González, J. G. Hiddink, K. M. Hughes, S. S. Intelmann, C. Jenkins, P. Jonsson, P. Kainge, M. Kangas, J. N. Kathena, S. Kavadas, R. W. Leslie, S. G. Lewis, M. Lundy, D. Makin, J. Martin, T. Mazor, G. Gonzalez-Mirelis, S. J. Newman, N. Papadopoulou, P. E. Posen, W. Rochester, T. Russo, A. Sala, J. M. Semmens, C. Silva, A. Tsolos, B. Vanelslander, C. B. Wakefield, B. A. Wood, R. Hilborn, M. J. Kaiser, and S. Jennings, *Bottom trawl fishing footprints on the world's continental shelves,* Proceedings of the National Academy of Sciences **115**, E10275 (2018), https://www.pnas.org/content/115/43/E10275.full.pdf .

[31] O. R. Eigaard, F. Bastardie, N. T. Hintzen, L. Buhl-Mortensen, P. Buhl-Mortensen, R. Catarino, G. E. Dinesen, J. Egekvist, H. O. Fock, K. Geitner, H. D. Gerritsen, M. M. González, P. Jonsson, S. Kavadas, P. Laffargue, M. Lundy, G. Gonzalez-Mirelis, J. R. Nielsen, N. Papadopoulou, P. E. Posen, J. Pulcinella, T. Russo, A. Sala, C. Silva, C. J. Smith, B. Vanelslander, and A. D. Rijnsdorp, *The footprint of bottom trawling in European waters: distribution, intensity, and seabed integrity,* ICES Journal of Marine Science **74**, 847 (2016), https://academic.oup.com/icesjms/article-pdf/74/3/847/31244877/fsw194.pdf .

[32] K. J. Van der Reijden, N. T. Hintzen, L. L. Govers, A. D. Rijnsdorp, and H. Olff, *North Sea demersal fisheries prefer specific benthic habitats,* PloS one **13**, e0208338 (2018).

[33] C. R. Bates, G. Scott, M. Tobin, and R. Thompson, *Weighing the costs and benefits of reduced sampling resolution in biomonitoring studies: Perspectives from the temperate rocky intertidal,* Biological Conservation **137**, 617 (2007), forests in the Balance: Linking Tradition and Technology in Lanscape Mosaics.

[34] J. R. Bennett, D. R. Sisson, J. P. Smol, B. F. Cumming, H. P. Possingham, and Y. M. Buckley, *Optimizing taxonomic resolution and sampling effort to design cost-effective ecological models for environmental assessment,* Journal of applied ecology **51**, 1722 (2014).

[35] C. De Moustier and H. Matsumoto, *Seafloor acoustic remote sensing with multibeam echo-sounders and bathymetric sidescan sonar systems,* Marine Geophysical Researches **15**, 27 (1993).

[36] L. Hellequin, J. . Boucher, and X. Lurton, *Processing of high-frequency multibeam echo sounder data for seafloor characterization,* IEEE Journal of Oceanic Engineering **28**, 78 (2003).

[37] C. J. Brown, S. J. Smith, P. Lawton, and J. T. Anderson, *Benthic habitat mapping: A review of progress towards improved understanding of the spa-*

tial ecology of the seafloor using acoustic techniques, Estuarine, Coastal and Shelf Science **92**, 502 (2011).

[38] M. A. Knaapen, *Sandbank occurrence on the Dutch continental shelf in the North Sea,* Geo-marine letters **29**, 17 (2009).

[39] M. Knaapen, *Sandwave migration predictor based on shape information,* Journal of Geophysical Research: Earth Surface **110** (2005).

[40] L. Koop, A. Amiri-Simkooei, K. J van der Reijden, S. O'Flynn, M. Snellen, and D. G Simons, *Seafloor classification in a sand wave environment on the Dutch continental shelf using multibeam echosounder backscatter data,* Geosciences **9**, 142 (2019).

[41] J. Nieuwenhuize, Y. E. Maas, and J. J. Middelburg, *Rapid analysis of organic carbon and nitrogen in particulate materials,* Marine Chemistry **45**, 217 (1994).

[42] A. M. Queirós, S. N. R. Birchenough, J. Bremner, J. A. Godbold, R. E. Parker, A. Romero-Ramirez, H. Reiss, M. Solan, P. J. Somerfield, C. Van Colen, G. Van Hoey, and S. Widdicombe, *A bioturbation classification of European marine infaunal invertebrates,* Ecology and Evolution **3**, 3958 (2013), https://onlinelibrary.wiley.com/doi/pdf/10.1002/ece3.769 .

[43] M. Solan, B. J. Cardinale, A. L. Downing, K. A. Engelhardt, J. L. Ruesink, and D. S. Srivastava, *Extinction and ecosystem function in the marine benthos,* Science **306**, 1177 (2004).

[44] D. C. Rhoads and S. Cande, *Sediment profile camera for in situ study of organism-sediment relations 1,* Limnology and Oceanography **16**, 110 (1971).

[45] A. Amiri-Simkooei, M. Hosseini-Asl, and A. Safari, *Least squares 2d bicubic spline approximation: Theory and applications,* Measurement **127**, 366 (2018).

[46] E. Hamilton, *Prediction of deep sea sediment properties state of the art. deep sea sediments,* in *Physical & Mechanical Properties* (Plenum Press, 1974).

[47] D. Jackson, *Apl-uw high-frequency ocean environmental acoustic models handbook,* Applied Physics Laboratory, University of Washington, Technical Report **9407** (1994).

[48] R Core Team, *R: A Language and Environment for Statistical Computing*, R Foundation for Statistical Computing, Vienna, Austria (2018).

[49] A. Ramette, *Multivariate analyses in microbial ecology,* FEMS Microbiology Ecology **62**, 142 (2007), https://academic.oup.com/femsec/article-pdf/62/2/142/18101219/62-2-142.pdf .

[50] S. Glen, *Principal component analysis, regression and parafac,* Online (2021).

[51] V. K. Bellec, V. R. Van Lancker, K. Degrendele, M. Roche, and S. Le Bot, *Geo-environmental characterization of the kwinte bank,* Journal of coastal Research , 63 (2010).

[52] J. Ellis, T. Maxwell, M. Schratzberger, and S. Rogers, *The benthos and fish of offshore sandbank habitats in the southern North Sea,* Journal of the Marine Biological Association of the United Kingdom **91**, 1319–1335 (2011).

[53] L. Godet, J. Fournier, M. Jaffré, and N. Desroy, *Influence of stability and fragmentation of a worm-reef on benthic macrofauna,* Estuarine, Coastal and Shelf Science **92**, 472 (2011).

[54] B. Pearce, *The ecology of Sabellaria spinulosa reefs*, Ph.D. thesis, University of Plymouth (2017).

[55] S. Bolam, R. Coggan, J. Eggleton, M. Diesing, and D. Stephens, *Sensitivity of macrobenthic secondary production to trawling in the English sector of the greater North Sea: A biological trait approach,* Journal of Sea Research **85**, 162 (2014).

[56] J. B. Jones, *Environmental impact of trawling on the seabed: A review,* New Zealand Journal of Marine and Freshwater Research **26**, 59 (1992), https://doi.org/10.1080/00288330.1992.9516500 .

[57] N. Gibb, H. Tillin, B. Pearce, and H. Tyler-Walters, *Assessing the sensitivity of sabellaria spinulosa to pressures associated with marine activities.* (2014).

[58] S. De Groot, *The impact of bottom trawling on benthic fauna of the North Sea,* Ocean management **9**, 177 (1984).

[59] C. J. Frid, K. Harwood, S. Hall, and J. Hall, *Long-term changes in the benthic communities on North Sea fishing grounds,* ICES Journal of Marine Science **57**, 1303 (2000).

7

Conclusion and outlook

The history of energy use is a sequence of transitions to sources that are cheaper, cleaner, and more flexible.

Vaclav Smil

I would like to die on Mars. Just not on impact.

Elon Musk

7.1. Recapitulation

The main focus of this thesis was to investigate the role of acoustics for habitat mapping with an interdisciplinary approach. The research area was the Dutch sector of the North Sea. One of the specific goals of this research was to expand the areas of the North Sea for which the relationship between backscatter and seafloor characteristics is understood well. Much of the previous research was focused on the Cleaverbank area of the North Sea. Since a big part of the southern North Sea is a sand wave area, specific attention was paid to gaining a better understanding of acoustic mapping for this area.

A particularly important question to investigate for MBES backscatter-based classification of sandy seafloors was the resolution of classification results. This is because these seafloors have repeating bedforms i.e., sand waves, of multiple sizes. Of these, the megaripple, has a wave length of only a few tens of meters. To detect changes at these scales, a high spatial resolution was needed, such that there were multiple classification points on the period of one megaripple. Furthermore, because the phenomena of interest was to detect the sorting of sediments that ranged from sand to coarse sand, a high geo-acoustic resolution was needed to detect these small differences in sediment composition. To answer these questions a dataset from the Brown Bank was used.

In a different dataset, also from the Brown Bank area, it was found that there is a sand ripple smaller than the megaripple present in this area. These sand ripples are too small to be captured by bathymetry measurements. However, a careful analysis of the backscatter showed the effects these sand ripples have on the backscatter signal. The presence of the sand ripples was confirmed by video data.

One of the most common data types that is used for seafloor classification in acoustics is backscatter. However, currently large gaps in backscatter coverage exist in the North Sea. It is not known when full coverage backscatter data of the North Sea in the Dutch sector will become available. However, the Hydrographic Service of the Royal Netherlands Navy collects bathymetric data for the entirety of the Dutch sector of the North Sea on regular intervals. Because of this, it was investigated if a classification method can be developed that is applicable for these areas of the North Sea where backscatter is not available but bathymetric data is available.

Finally, it was investigated how to best link acoustic seafloor data to habitat data such as video and grab-sample data. The end goal of the acoustic mapping is to create maps not just of the bathymetry or sediment type but of the habitats of the seafloor in full coverage and in high detail. It is important for future projects that the DISCLOSE project creates links between these methods. This is a necessary step towards creating full coverage habitat maps with good resolutions.

7.2. Conclusions

In Chapter 3 it was investigated how to characterize the seafloor in a sand wave environment the Bayesian classification method was applied to MBES backscatter data gathered in the Brown Bank area of the North Sea. To obtain reliable classification results, steep and rapidly changing slopes over tens of meters had to be corrected for. Acoustic classification results were then compared with video and grab-sample data.

Based on the results of the sediment grain size analysis from the grab samples, it was found that the seafloor sediments of the Brown Bank area are very homogeneous. At each sampling station three grab samples were taken, and the variance in the mean grain size over the entire survey area was similar to the variance within the triplicate grab samples from the individual sampling stations. However, Folk classification of grab samples, as well as, the acoustic classification results were more discriminative. A further analysis showed that for areas like the Brown Bank, the full grain size distribution should be used when classifying the grab samples and when relating this ground truth data to the acoustic classification results.

For acoustic classification of sediments in relatively homogeneous environments, especially over megaripple structures, high spatial and geoacoustic resolutions are required. There is, however, a trade off in these resolutions. Therefore, depending on the aim of a classification application, either of these resolutions can be prioritized for. It was found that the Bayesian classification method remains statistically sound when optimizing for the spatial resolution, as long as the number of scatter pixels used in the averaging satisfies the central limit theorem requirements. This is a pivotal result that underscores the validity of the acoustic classification results over megaripples.

The results further revealed that there was a significant sorting of sediments over megaripples. Higher acoustic classes, and therefore coarser sediments, were found in the troughs and on the crests. Low acoustic classes were consistently found to be on the steepest part of the stoss side of a megaripple. On the, even steeper, lee side slope of the megaripple a mixture of all acoustic classes was found.

These detailed results related to megaripples have a number of implications. First, for detailed habitat maps, the size of the megaripple and not that of the sand wave should define the resolution scale of the map. Next, researchers gathering ground truth data, such as grab samples and video data, should strive to geo-reference the point measured on the seafloor with an accuracy well below the wavelength of megaripples to avoid ambiguities. Finally, it confirms that the classification of backscatter data from MBES systems is a powerful method to further study and display the spatial distribution of sediments over megaripple bed forms. As such, it can provide valuable information for habitat mapping, engineering projects such as offshore wind farms or pipe laying, or to serve as field validation data for sand wave modelers.

From the second data set that was collected in the area of the Brown Bank, and discussed in detail in Chapter 4, it was found that small-scale repeating seafloor structures (sand ripples), have a profound impact on angular response curves (ARCs) of MBES backscatter data. Visible in the ARCs, were unexpected off nadir peaks. These patterns were influenced by the survey azimuth, but not consistent when the survey azimuth was held constant. It was found that the pattern switched on the same time intervals as the switch of the tide flow direction. These survey-azimuth dependent ARC patterns were consistent with prior findings, but in this thesis it was further shown that even from the same area of seafloor and a constant survey azimuth, backscatter results differed in time. Video ground truth confirmed that the switch in ARC pattern matched an orientation switch in sand ripples on the seafloor. These results have implications for several different classification algorithms. Many of these classification algorithms make use of the relationship of increased backscatter intensity corresponding to larger mean grain sizes to estimate the mean grain size of parameter of the seafloor sediment composition. There are other factors that can increase backscatter strength, and the results of this research indicate that the sand wave topology of the seafloor can also result in an increase in backscatter strength. Therefore, care must be taken that it is not seafloor topology, rather than seafloor sediment composition, that is being characterized when performing backscatter-based seafloor characterization in sand wave environments.

We further suggest that the pattern in the ARCs is useful as a diagnostic tool. Firstly, the off nadir peaks in the ARCs indicate the slope angles of the sand ripples. The slope angles indicated by the ARCs in this research, matched well with typical lee and stoss side slope angles of sand ripples from the literature. From the two angles, the avalanching observed for the lee side measurements in the video data, allowed the use of the known *angle of repose* for sand in water to be compared with the angles indicated from the ARC patterns. The indicated slopes of the stoss side of the sand ripples were harder to validate.

Importantly, a clear link between ARC pattern and sand ripple orientation on the seafloor was shown. This was confirmed by the use of both video ground truth data and modeled tidal flow data. It was possible to predict the orientation of sand ripples on the seafloor based on patterns in the acoustic data. By this method it was possible to make these predictions over spatial scales of kilometers.

Another methodology, such as using video data, would not be able to make such predictions over such large areas cost effectively. Furthermore, the use of MBES bathymetry would have failed to yield this result, due to the insufficient resolution of the bathymetry data. These results showcase the advantage of combining different sampling methods such as acoustics and video cameras. The results further showed that the top centimeter of the seafloor undergoes a complete transformation every six hours in this part of the North Sea. The capability to take such measurements from acoustic data shows that the methods employed in this thesis are an invaluable tool for habitat mapping.

To overcome the large gaps in coverage in backscatter data for the Dutch sector of the North Sea, two seafloor classification methods were developed in Chapter 5 that use an object-based image analysis approach. The methods use bathymetry, bathymetric derivatives, and grab samples as input, and do not rely on the use of backscatter. The transferability of the best method was tested by applying it to two data sets. The first data set was from Norwegian waters, specifically the Røstbanken area off the coast of Lofoten. The second data set was from the Borkumer stones area close to the island of Schiermonnikoog in Dutch waters. The classification results were compared to the results from an existing backscatter-based classification Method (referred to as Method 1 in the chapter) in the case of the Røstbanken data, and to grab sample ground truth data for both data sets.

The first of the developed methods (referred to as Method 2) used a purely texture-based object-based image analysis approach. The second method (Method 3) was similar, but used additional image object features. Both methods are fast enough to be used over large coastal areas with data resolutions of 5 × 5 m. To apply the method(s) to new areas, adjustments to the scale parameter of the segmentation algorithm were necessary. Additionally, when creating the first two levels of image objects, image layer choice was important in order for the shapes of the image objects to conform to small-scale features of the seafloor. With these adjustments, the algorithm was transferable to new research areas.

When comparing Methods 1, 2 and 3 to grab sample ground truth data, a respective classification accuracy of 98.7%, 73%, and 87% was found. These accuracies were measured by splitting the grab samples into a training and testing subset. The algorithms where trained using the training subset. After the classification was performed, then the classification accuracy was tested using the testing subset of grab samples. For the mentioned accuracies, a tolerance of ± 1 class was used. When compared to the results from Method 1, then Method 2 had an accuracy of 52% and Method 3 an accuracy of 86%, again with a ± 1 class tolerance. Because the input requirements and computation cost does not differ significantly between Methods 2 and 3, the use of Method 3 is hence recommended.

Having a bathymetry and bathymetric derivative based classification method was important given that bathymetry data is more available than backscatter data for many coastal seas. This importance was even greater when considering full global coverage of bathymetric data being available through projects such as the GEBCO seabed 2030 project [1]. As such, the results presented in this chapter should be of wide interest to the seafloor classification community.

Furthermore, in the DISCLOSE project strong links between the use of acoustic results, video results, and grab sample results were made in Chapter 6. It was clear that the combining of these methods improved the overall habitat mapping capability. It was also found that links between benthic habitats and acoustic results were often not linked directly to bathymetry or backscatter. Often these links were strongest between bathymetric derivatives such as the bathymetric position index or backscatter parameters such as volume scattering. This strengthens the case not just for multidisciplinary data gathering, but also that within acoustic data gathering as many different data types should be gathered as possible.

The North Sea played an integral part in Dutch history, and will continue to do so in the coming years. This is due to activities such as shipping and fishing that take place there. The North Sea is also one of the busiest seas in the world. All of this industrial and fishing activity must have an effect on seafloor habitats of the North Sea. But even if this was not the case, it would still be of scientific benefit to establish a good habitat baseline for the North Sea that could be referenced in the years, decades, and centuries to come. The work accomplished in the DISCLOSE project is a vital step in the direction to make a full-coverage baseline habitat map a possibility. As such, this work has high scientific, and social value to our society that is so dependent on the North Sea.

7.3. Outlook

As is often the case, an answer to question 1 raises questions 2 and 3. The research results from this thesis also provide numerous directions for future research. From the research results related to sediment sorting on megaripples it was found that for different areas the lee side steepest slopes of the megaripples showed the entire range of acoustic classes. Future research should uncover what the cause for this mixed result is. It is recommended that multiple frequencies be used for such research. Good notes should be taken on the tidal flow velocities and directions to investigate if the changes are related to the flow of the tide. This could help to investigate if the changes are related to avalanching on these slopes. Another possible cause would be the directions of sand ripples towards the bottom of the lee side slope. It is known that flow separation can happen over megaripples, with a backwards flowing eddy in the trough of the megaripple. It is possible that the directions of sand ripples change in the troughs of the megaripple. If video camera ground truth data is collected, then very careful geo-referencing should be performed to know precisely what part of the megaripple is observed in the footage.

Another question to investigate, is if the stoss and lee side slopes of tide driven sand ripples can be accurately measured by use of a multibeam echosounder. This would easiest to do in the controlled environment of a tank, such that sand ripple slope angles could be more easily measured.

The object-based image analysis based seafloor classification was applied to two research areas. An obvious next step would be to apply it to the entire Dutch sector of the North Sea. For this it would need to be investigated what effect the resolution of bathymetry data has on the classification results. Another research question is if the use of different bathymetry derivative layers could be used to make predictions not just about the superficial sediment, but of the subsurface sediments. It would also be worthwhile to investigate if a generic rule set could be developed that did not rely on grab sample training data.

In a more general sense, a deeper integration of the different methods used in the DISCLOSE project should be pursued. In this thesis video camera data was compared to acoustic data in order to validate acoustic classification. In the future, it would be of value to automate classification of video data by use of trained machine learning methods to classify the seafloor visible in the video data. These classified video frames should further be accurately geo-referenced, and could then be used as a training set for acoustic data in order to automatically extrapolate the video based classification to large areas.

A goal for the distant future would be to use autonomous video drones and autonomous MBES drones to go to sea to gather data from a target research area. The video data could then be used to train the classifiers for the acoustic data to create full coverage habitat maps of the seafloor. To create such a system would require significant investment for research and development, but once operational, would greatly decrease the personnel and ship time overhead that is currently needed for habitat mapping.

References

[1] L. Mayer, M. Jakobsson, G. Allen, B. Dorschel, R. Falconer, V. Ferrini, G. Lamarche, H. Snaith, and P. Weatherall, *The nippon foundation—GEBCO seabed 2030 project: The quest to see the world's oceans completely mapped by 2030,* Geosciences **8**, 63 (2018).

Curriculum Vitæ

Leo KOOP

08-06-1985	Born in Spanish Lookout, Belize.

Education

1992–2000	Grade School Gnadenfeld, Spanish Lookout, Belize (1992–1998, 2000) Valley view, Spanish Lookout, Belize (1999)
2006–2010	Undergraduate in Mathematics, minor in Information Technology University of Belize, Belmopan, Belize
2010 – 2012	Graduate studies in Bible truth & Church service, Full Time Training in Anaheim, Anaheim, California, USA
2013 – 2014	Master of Science in Scientific Computing Technische Universität Berlin, Berlin, Germany
2014 – 2015	Master of Science in Applied Mathematics Delft University of Technology, Delft, The Netherlands
2016 – 2021	Doctor of Philosophy (Ph.D) in Underwater Acoustics, Delft University of Technology, Delft, The Netherlands
Thesis:	Using multibeam echosounders for multiscale and interdisciplinary habitat mapping on the Dutch Continental Shelf
Promotors:	Prof. dr. D. G. Simons and Prof. dr. ir. M. Snellen

Awards

2010	Degree with highest GPA in Science and Technology, University of Belize
2017	Ron McDowell student scholarship to speak at GeoHab 2017

Acknowledgements

I am sure everyone has their unique experiences for each stage in their life. I must admit that my years as a PhD researcher have been very eventful, perhaps the most eventful years of my life. A few years ago I experienced the losing of my mother when she suffered an unexpected stroke. Two years later, my father also passed away. And this, during the corona crisis, when traveling to the funeral was not possible. On the positive side, I also got married during my PhD years to the most wonderful wife. We have since welcomed our first child into the family. Little David is the joy of the family.

There are many people that I would like to thank. I will start with some of the academic staff from the Delft University of Technology. Dick Simons, you were instrumental in getting this project off the ground. Without your work, this PhD would have never been possible for me. I also appreciate your fast and critical thinking and your concise feedback related to the project and publications. Mirjam Snellen, without your faithful feedback during my entire PhD project it would have not been nearly as smooth of an experience. Also, your willingness to lay down the law when things needed to get done, was helpful in the end. Alireza, your coming up to the DISCLOSE project was a big help especially in getting over the hump of the first journal publication. And I cannot forget Lisette Vollmer, without you arranging so many day-to-day practical details, where would we, the PhD candidates, be?

My project was part of a much larger project that involved two other research institutes, as well as the North Sea foundation. The project was funded by the Gieskes Strijbis Fonds. Without them, the project would not have been possible. I would like to thank Hedda van Straten and Frederiek Cohen for their oversight of the project and vital input at various stages. I would further like to thank the director, Roderic Evens Knaup and the rest of the Board of the Gieskes Strijbis Fonds. Then, from the Royal Netherlands Institute for Sea Research; Peter Herman, your ideas for research opportunities were inspiring and your attention to detail and academic rigor was helpful. Tom Ysebaert, your arrangement of the ship time opportunities and giving us access to the particle size analysis lab, was instrumental in finishing my PhD. Sarah O'flynn, I would like to thank you for all the work you did to arrange the ship time, as well as the measurement methodologies you designed that resulted in some of our later papers. Sebastiaan Mestdagh, although you joined the project later, it was great working with you. Peter van Breugel, thank you for teaching me the ins and outs of particle size analysis. Henk de Haas, thank you for all of the practical information and advice on operating acoustic data gathering equipment at sea. Finally, the crew of the Pelagia during all the different times that we were sea, thank you. Now from the University of Groningen; Han Olff, all your critical questions in all of our meetings kept us on our toes, thank you. Laura, your easy-going manner and attention to detail for practical matters was an example for us to follow. Karin van der Reijden, we certainly have had very many experiences together, ranging from all of the meetings, to the arranging for and carrying out of all the sea going experiments, and all of the writing of the papers. It has been a pleasure performing research in the same project with you together.

To my colleagues at the research group. Timo, all of our hours of conversations about the functioning of multibeam echosounders, what things to consider, what things not to consider, in survey design and data processing was helpful. Tannaz, your work ethic has been an inspiration and your humbleness to approaching and attacking any problem despite how large it is, has been encouraging. Afrizal, thank you for being on that ship with me together and working those insane hours, in order to get the research data that we needed. Roberto, your easy-going and upbeat attitude belie the serious academic that you are. Anwar, thank you for being my first office mate and introducing me to all the ins and outs of PhD life. Ana, of all the offices I have been in, the one we were in was the best. Collin, the bouldering trips were awesome. Raoul and Elisabeth, thank you for working all of those crazy hours with me at sea. It was a pleasure working with the both of you together.

Then, a thank you related to the design of the cover. Tamara van Dijk, thank you for all of your hard work to make the cover design a reality. The cover illustrates the research methodology adopted in the DISCLOSE project. The water surface of the sea is easy for all to see. This is why it stretches from edge to edge of the cover. Within DISCLOSE we first used the MBES to determine the accurate depth of the seafloor. By the MBES data we could also interpret many seafloor characteristics. The MBES covered the largest area, hence the seafloor extends from the point of the discovery all the way to the left edge of the cover. By using video and photos of the seafloor a more detailed knowledge of the seafloor was gained, albeit at smaller scales. Finally, by the use of grab samples, still more detail was generated, also about the subsurface, but at still smaller scales. Hence the reason this is illustrated on the cover just once.

Finally, I would like to thank a number of my family and friends. My father who always encouraged us to learn, and his discussions on seemingly any physics topic. Without those conversations, I do not think I would have ever made it to the Delft University Of Technology, let alone pursue a doctorate degree. My mother, there are too many things that I have her to thank for. Oh, how I wish she could have seen me at my graduation. Jacob, where would I be without you, your input, and your encouragement. Without it I would probably not have ever graduated with a Bachelor degree. Too my family-in-law; Collin, your kindness and your care for us in every situation is appreciated. Wilma, thank you for always having a ”can do” attitude. Finally, to the most important person in my life, my Carolien. Thank you for bearing with me through all the ups and downs, finally we have arrived at the end of this chapter. And to the littlest guy in the family, David, you are the best dude to chillax with at the end of a brain-draining day.

List of Publications

11. K. J. Van Der Reijden, L. L. Govers, **L. Koop**, J. H. Damveld, P. M. J. Herman, S. Mestdagh, G. Piet, A. D. Rijnsdorp, G. E. Dinesen, M. Snellen and H. Olff, *Beyond connecting the dots: A multi-scale, multi-resolution approach to marine habitat mapping.* Ecological indicators, 128, 107849, (2021).

10. **L. Koop**, M. Snellen and D. G. Simons, *An Object-Based Image Analysis Approach Using Bathymetry and Bathymetric Derivatives to Classify the Seafloor.* Geosciences, 11(2), 45 (2021).

9. **L. Koop**, K. J. Van Der Reijden, S. Mestdagh,T. Ysebaert, L. L. Govers, H. Olff, P. M. J. Herman, M. Snellen and D. G. Simons, *Measuring Centimeter-Scale Sand Ripples Using Multibeam Echosounder Backscatter Data from the Brown Bank Area of the Dutch Continental Shelf.* Geosciences, 10(20), 495, (2020).

8. S. Mestdagh, A. Amiri-Simkooei, K. J. van der Reijden, **L. Koop**, S. O'Flynn, M. Snellen, C. Van Sluis, L. L. Govers, D. G. Simons, P. M. Herman and H. Olff, *Linking the morphology and ecology of subtidal soft-bottom marine benthic habitats: A novel multiscale approach.* Estuarine, Coastal and Shelf Science, 106687, (2020).

7. **L. Koop**, A. Amiri-Simkooei, K. J. van der Reijden, S. O'Flynn, M. Snellen, and D. G. Simons, *Seafloor classification in a sand wave environment on the Dutch Continental Shelf using multibeam echosounder backscatter data.* Geosciences, 9(3), 142, (2019).

6. A. R. Amiri-Simkooei, **L. Koop**, K. J. van der Reijden, M. Snellen, and D. G. Simons, *Seafloor characterization using multibeam echosounder backscatter data: methodology and results in the North Sea.* Geosciences, 9(7), 292, (2019).

5. A. R. Amiri-Simkooei, **L. Koop**, M. Snellen, and D. G. Simons. *Seafloor sediment characterization using multibeam echosounders without grab sampling: Opportunities and challenges.* Conference Proceedings of the 5th Underwater Acoustics Conference and exhibition 2019: UACE2019, Hersonissos, Crete, Greece, 30 June through 05 July 2019.

4. K. J. Van Der Reijden, **L. Koop**, S. O'flynn, S. Garcia, O. Bos, C. Van Sluis, D. J. Maaholm, P. M. Herman, D. G. Simons, H. Olff and T. Ysebaert, *Discovery of Sabellaria spinulosa reefs in an intensively fished area of the Dutch Continental Shelf, North Sea.* Journal of Sea Research, 144, 85-94, (2019).

3. J. H. Damveld, K. J. Van Der Reijden, C. Cheng, **L. Koop**, L. B. Haaksma, C. A. J. Walsh, K. Soetaert, B. W. Borsje, L. L. Govers, P. C. Roos and H. Olff, *Video transects reveal that tidal sand waves affect the spatial distribution of benthic organisms and sand ripples.* Geophysical Research Letters, 45(21), 11-837, (2018).

2. M. Snellen, T. C. Gaida, **L. Koop**, E. Alevizos, and D. G. Simons, *Performance of multibeam echosounder backscatter-based classification for monitoring sediment distributions using multitemporal large-scale ocean data sets.* IEEE Journal of Oceanic Engineering, 44(1), 142-155, (2018).

1. T. Haji Mohammadloo, T. Tengku Ali, M. Snellen, **L. Koop**, T. C. Gaida, and D. G. Simons, *Assessing the repeatability of sediment classfication method and the limitations of using depth residuals*. 4th Underwater Acoustics Conference and Exhibition, (2017).